Imperial College
London

The study of crack growth in polyethylene using traction-separation laws

Kwang Ming Simon TING

A thesis submitted for the degree of Doctor of Philosophy of the University of London and the Diploma of Imperial College London

December 2003

Department of Mechanical Engineering
Strength of Materials
Imperial College London
London SW7 2BX

Abstract

Understanding the mechanisms of crazing, which are the precursor to fracture in polyethylene under slow crack growth conditions, is one of the key factors in the development of tough materials for structural applications such as in pipes for the transportation of water and gas.

Due to the localised nature of the damage (craze) evolution in polyethylene, it was possible to postulate a traction-separation relationship to describe the fracture process. Using a circumferentially notched tensile specimen, the relationship has been examined over a wide range of constraint and rate conditions. The aim is to show that the traction-separation behaviour of polyethylene is constraint and rate dependent and that this dependency can lead to contrasting damage-failure behaviour between different grades. On a macroscopic scale, this is manifested by distinctive crack growth behaviour with varying degrees of resistance against crack propagation. As a result, the nature and the type of the damage formed affected the overall energy dissipation. The implication on the fracture toughness and hence the long-term fracture properties is significant. Through the optical and microscopy work, a unified approach was developed which combines mechanical characteristics with microstructural observations. Based on this approach, both gross and subtle differences in the fracture behaviour between different grades were readily detected and differentiated. Furthermore, the structure-property relationship associated with each grade was established. Such an analysis should provide the crucial information about the material performance for plastic pipe manufacturers in the development and the characterisation of new generations of pipe materials

Preliminarily numerical simulations of the circumferentially notched tensile tests were performed using the Finite Volume method. The aim is to determine the appropriateness of the measured cohesive laws in the numerical simulations. Results of this study will serve as the platform for the development of a fully predictive fracture model.

Acknowledgements

I would like to first express my deepest gratitude to Prof. J Gordon Williams and Dr. Alojz Ivankovic for their guidance and supervision throughout the duration of the project. I am grateful for their encouragement and advice. I am thankful for the generous financial support provided by BP-Solvay (formerly BP Chemical Ltd.) for the project and also for providing the materials. I also like to thank Dr. Ed Q Clutton of Impact Lab. (formerly with BP Chemical Ltd.) and Dr. Virgile Rouyer of BP-Solvay for their comments and support.

I would like to show my appreciation to all members of Strength of Materials section especially Dr. Vlado Tropsa and Dr. Alex Karac for their assistance and coaching in the use of FOAM. The logistics and technical support given by Mr. Nick Tailor (retired) and Mr. Chris Jerrard have helped reduced the effort during the project in many ways. I also like to thank Dr. Aaron Goh, Mr. Keith Cheong, Mr. Chaiwut Gamonpilas, Mr. Kar Tan, Mr. Luiz Kawashita, Ms. Vassia Paloumbi and Ms. Wernsze Teo for their friendship. I also appreciate the interest showed by Dr. Brain Cotterell and Prof. Alfred Huan of IMRE in the project. I am also indebted to A*Star of Singapore for the generosity provided during the fellowship program.

Finally, I am very grateful to my wife and daughter for the love and in helping me to keep things in perspective.

For my wife and daughter

Contents

List of figures

Chapter 1

Chapter 2

Chapter 3

Chapter 4

Chapter 5

Chapter 6

Chapter 7

Chapter 8

List of tables

Nomenclature

List of Latinsymbols

a	Notch depth/ crack length
A_o	Initial/original cross-sectional/ligament area
A_i	Instantaneous cross-sectional area
c	Length of plastic zone
E	Young's modulus/ modulus of elasticity
E_0	Modulus at unit time
E^p	Plastics/hardening modulus
l_c	Current length
l_f	Final gauge length
l_o	Initial gauge length
l_{xhead}	Crosshead extension
m	Power law index
M	Crack tip constraint factor
M_w	Weight average molecular weight
M_n	Number average molecular weight
n	Power law index
P	Load
P_D	Polydispersity
T_n	Normal traction
u_n	Normal displacement

Greek symbols

Γ	Cohesive energy /area under the traction-separation curve
ρ	Density
ε_{eng}	Engineering strain
ε_{true}	True strain
ε_y	Yield strain

$\dot{\varepsilon}$	Strain rate
δ	Displacement/separation
δ_{break}	Separation at decohesion/break separation distance
δ_{COD}	Critical separation value
δ_{normal}	Normal displacement
δ_{peak}	Peak separation distance
$\delta_{tolerance}$	Tolerance value for numerical simulation
σ	Applied stress
σ_{eng}	Engineering stress
σ_{normal}	Normal stress component
σ_{peak}	Cohesive/peak/maximum stress/strength of the traction-separation curve
σ_{soft}	Softening stress
σ_{true}	True stress
σ_Y	Yield stress
σ_{Y0}	Yield stress at unit time
λ	Extension/draw ratio

Abbreviations

BMPE	Blow moulding polyethylene
CNT	Circumferentially notched tensile test
CZ	Cohesive zone
CZM	Cohesive zone model
DENT	Double edge notch test
FNCT	Full notch creep test
FOAM	Field Operation And Manipulation
FV	Finite volume
FVM	Finite volume method
GL	Gauge length
HDPE	High density polyethylene
LEFM	Linear Elastic Fracture Mechanics

MWD	Molecular weight distribution
PE80	2nd generation pipe grade with excellent slow crack growth resistance.
PE100	3rd generation pipe grade with excellent slow crack growth resistance.
PE	Polyethylene
PENT	Pennsylvania edge notched test
RCP	Rapid crack propagation
RPM	Revolution per minute
SCB	Side chain branch
SCG	Slow crack growth
SEM	Scanning electron microscopy
TS	Traction-separation

Chapter 1
General Introduction

When British Gas first introduced polyethylene pipes into their pipeline systems in 1969, it generated a considerable amount of interest in employing polyethylene as the alternative source of materials for the manufacture of pressurised pipes in the transportation of gas and water. Polyethylene pipes offered numerous advantages over traditional pipe materials such as cast and ductile iron. Being chemical resistant, ductile and tough, polyethylene offered good resistance against corrosion, environmental degradation and soil movements. Their flexibility and lightweight allows long lengths of pipe to be supplied in, and laid from, coil thus facilitating new laying techniques that avoid frequent introduction of joints and fittings. It can be seen from the Figure 1.1(a) that pipe supplied in coil allows the laying of long pipe lengths to be carried out easily (Figure 1.1(b)), which can lead to a substantial saving in installation costs. Moreover, the ease of fabrication and lower material cost also enhanced their popularity with manufacturers.

(a) (b)

Figure 1.1 (a) Long lengths of pipe supplied in coil (*from* http://www.wavin.co.uk) (b) Laying of plastic pipelines (*from* http://www.pe100plus.net)

Furthermore, the long and proven track record of polyethylene pipes being employed for water and gas distribution has also contributed towards its widespread use in low pressure piping applications. A recent study by Beech *et. al.* [2001a] reported that the demand for polyethylene pipes would continue to grow into 2005. As can be seen from the Figure 1.2, the predicted volume in 2005 almost double that in 1985. This data

reaffirmed that polyethylene would continue to hold an important role in the development of reliable and durable pipelines.

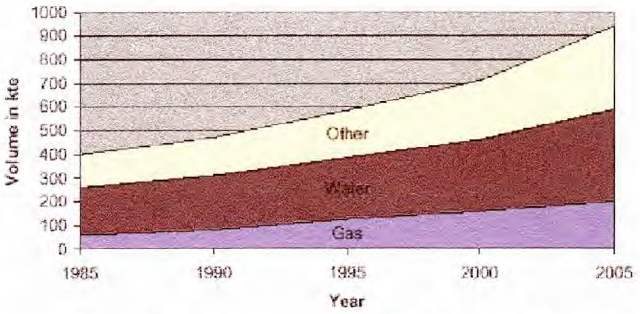

Figure 1.2 Actual and predicted growth of the polyethylene pipe market in Western Europe (*from* Beech *et al.* [2001a]).

Although polyethylene pipes have good service and safety records their time and temperature dependent characteristics are known to account for a number of field failures. At low temperatures and high strain rates, rapid crack propagation (RCP) can potentially take place thereby destroying a substantial length of the pipeline. A second mode of failure is associated with a long term slow crack growth (SCG) process. In SCG, a pre-existing defect (e.g. deep sharp cracks) provided the site for the initiation of cracks. The cracks then grow under the low static load in the pipe wall over a long period of time proceeded by a craze. The breakdown of the craze is known to cause the pipe to fail in a brittle manner under SCG conditions. Under real service conditions, the internal pressure provides the driving forces for the SCG phenomenon. Additionally, the complex loading system that occur in buried pipes, as illustrated in Figure 1.3, would have significant effects on the deformation behaviour.

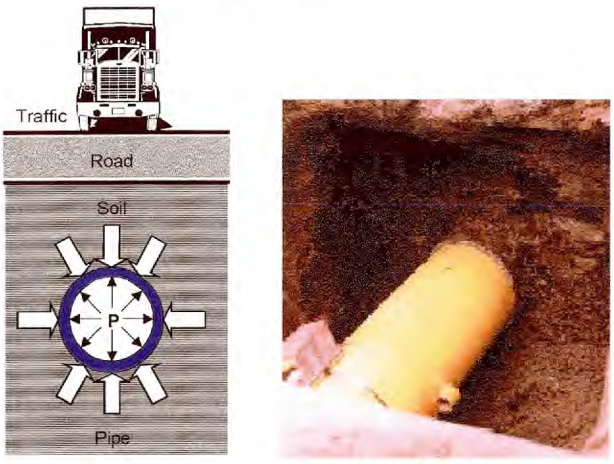

(a) (b)

Figure 1.3 (a) General loading condition of buried pipes. (b) Buried pipelines.

The present work focuses on the SCG which is often regarded as the more critical fracture characteristic between the two modes of failures (RCP and SCG) since it would require slow crack growth to provide an initiation site for RCP. In characterising the SCG resistance, numerous studies have exploited the applicability of laboratory sized deep notch specimens to provide an integrity assessment of large structure with defects, such as the full notch creep test (FNCT) (Nishio *et. al.* [1985]), the double edge notch test (DENT) (Choi and Broutman [1985]), the Pennsylvania edge notch test (PENT) (Lu and Brown [1992]) and the circumferentially notch tensile test (CNT) (Duan and Williams [1998]). Such an approach is often taken with a view to accelerate the failures in laboratory conditions and also to reduce the costs associated with large-scale tests. Moreover, the localised nature of the damage (craze) evolution ahead of the crack front permitted the use of laboratory sized specimens to facilitate the SCG assessment. A good correlation was found between the laboratory results and the SCG resistance of pipe (Tränkner *et. al.* [1996] and Lu *et. al.* [1997]). These studies were mainly performed in plane strain conditions arising from the deep notch geometry. In this aspect, the SCG resistance thus evaluated may be regarded as the inherent resistance to slow crack growth in the brittle fracture mode since it represents a lower bound of the material toughness. Therefore, these tests may be viewed as too severe in relation to possible service situations (e.g. surface notches caused by rock/soil impingement) where the level of constraint is possibly lower and hence the deformation capacity would be different (Beech *et. al.* [2001b]). Furthermore, the structural condition is likely to cover a wide range of constraint (or stress triaxiality). Depending on the material ability to yield locally, a low constraint could invoke ductile mechanisms and cause a considerable increase in the fracture resistance. In some extreme cases, it leads only to plastic flow. However, the influence of the ductile mechanisms on the SCG process has yet to be examined extensively. Comparatively few studies have addressed the effect of constraint (crack tip constraint) on SCG behaviour.

1.2 Project aims

The primary aim of this thesis is to examine the role of the crack tip constraint on the fracture behaviour of a range of polyethylenes. By utilising a circumferentially notched

tensile specimen devised by Duan and Williams [1998], it was possible to vary the geometric constraint via the notch depth and the specimen thickness. By subjecting the specimens to uniaxial tension at various constraint and rate conditions, a wide range of experimental data were collected. Due to the localised nature of the damage zone, it allowed the postulation of a traction-separation relation to describe the fracture process. Through the microscopy work, a unified approach was developed which combines mechanical characteristics with microstructural observations. On this basis, the damage and failure mechanisms associated with each grade were identified as well as the structure-property relationship. The investigation also presented one of the few studies that deal with the direct determination of the cohesive law. A relatively smaller proportion of project time was spent in the numerical analysis which was based on the Finite Volume (FV) scheme. The CNT model was developed, validated and simulated for a limited range of the measured cohesive laws. Results of this study will serve as the platform for the development of a fully predictive fracture model

1.3 Thesis outline

The thesis is organised as follows. In Chapter 2, a literature survey on subjects related to the present work is given. Chapter 3 introduces the material used in this project and details the specimen preparation and the experimental technique. This is followed in Chapter 4 by examining the stress-strain behaviour of the material at various rates. The traction-separation behaviour is given in Chapter 5 and illustrates the role of the crack tip constraint on the damage-failure mechanisms and the relation between mechanical properties and microstructure are presented in Chapter 6. Chapter 7 describes the results of the numerical study. Concluding remarks and recommendations for future work are given in Chapter 8.

Chapter 2

Literature review

2.1 Introduction

The purpose of this chapter is to provide a literature survey on subjects related to the present work. A review of the molecular structure in polyethylene forms the starting point in understanding the mechanical behaviour. This is followed by examining the phenomenon of crazing in polyethylene, which is regarded as the key to understand the reasons behind the material resistance to deformation and hence the material toughness. Finally, the chapter concludes with a focus on some of the recent findings on cohesive zone modelling.

2.2 Physical structure of polyethylene

Polyethylene is one of the most widely studied polymers that belong to the family of thermoplastics. Polyethylene is produced by joining together ethylene monomers to form a long covalently bonded chain which consists of a backbone of carbon atoms. Under a combination of heat, pressure and catalysts, the double bond between the carbon atoms of the ethylene molecule is broken to a single bond. This allows the linking process to begin where many more ethylene monomers are added to the growing chain. The chemical process is known as addition polymerisation, which is a popular method for producing polyethylene.

2.2.1 Branching of polyethylene

The main chain formed can be branched, whereby a complete chain section replaces the H atom attached to the main linear chain to form a branched polyethylene, as

illustrated in Figure 2.1. However, branching reduces the packing efficiency of the chains making it more difficult to crystallise which in turn decreases the density. The material strength falls as an indirect result of branching. Furthermore, branching is known to obstruct the movement between molecular chains during disentanglement. This obstruction could be highly detrimental in impact loading as it decreases the chain mobility. On the other hand, branching has a beneficial effect during SCG as it keeps the chain from unravelling.

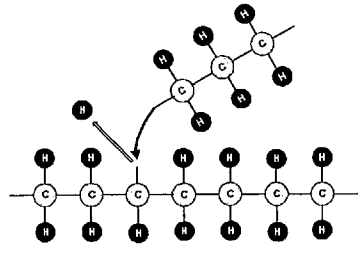

Figure 2.1 Schematic illustration of the branching process.

2.2.2 Molecular weight

The growth and termination of the chains during polymerisation is a statistical process, resulting in a nonuniform distribution of chain length and weight that often resembles a bell-shaped curve giving the molecular weight distribution (MWD) curve. The molecular description of the material is usually completed with the definition of the number average molecular weight, M_n and weight average molecular weight M_w.

$$M_n = \frac{\sum n_i M_i}{\sum n_i} \tag{2.1}$$

$$M_w = \frac{\sum n_i M_i^2}{\sum n_i M_i} \tag{2.2}$$

Where n_i represents the number of molecules with molecular weight, M_i. The value of M_n is sensitive to the presence of short and light chains while M_w value depends on the high M_i species (long and heavy molecules). The ratio of M_w over M_n defines the polydispersity, P_D or the range of molecular sizes in the material. Greater control during polymerisation is required to narrow the MWD, whereby the proportion of short chains to long chains would be evenly distributed. On the whole, the entanglement density

increases with an increase in the molecular weight due to a greater probability that long molecular chains would form entanglement points. In addition, these entanglement points behave rather like permanent chemical crosslinks, thereby increasing the strength of the material. The likelihood of forming inter-crystalline tie molecule also increases with molecular weight, which in turn is a contributory part of the overall entanglement density. The combined effects of long molecular chains and inter-crystalline ties would generally increase the resistance against the disentanglement processes. Normally, the mechanical properties (strength and stiffness) improve with increasing molecular weight however, it is also coupled with an increase in the melt viscosity. Processing practicalities and costs therefore restricted the molecular weight increase. From the literature the molecular weight and branching are often cited as the two most important structural variables in manipulating the SCG resistance (O'Connell *et. al.* [2003]).

2.2.3 The crystalline and amorphous structure

The conventional model of bulk polyethylene consists of amorphous regions sandwiched between crystalline regions which are held together by tie molecules that extend from one crystalline layer to another as illustrated in Figure 2.2. The crystalline region contains molecule chains folded in a repeated manner to form ordered crystalline lamellae as opposed to the disordered structure characterised by the random chains arrangement in the amorphous region. The amorphous structure can be thought of as frozen melt in which the molten state structure is retained at room temperature. At room temperature, the material obtained the strength through the crystalline lamella while the ductility is via the amorphous domain. The tie molecules are believed to constrain the extent of ductile deformation. Under tensile loading modes, the interlamellar separation is thought to cause voiding in the amorphous region (Lin and Argon [1994]).

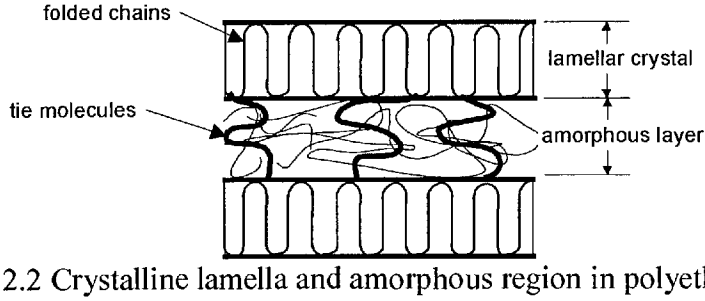

Figure 2.2 Crystalline lamella and amorphous region in polyethylene.

2.3 Crazing in polyethylene

Craze can be described as a plastically deformed region that lies along the crack plane developed from microvoids into highly fibrillated structure, separated by voids ahead of the crack tip. A side view of a typical craze is shown in Figure 2.3. Crazing was first identified more than 30 years ago in glassy polymers. The discovery of the craze was soon recognised to be different from either shear bands or cracks because of the existence of the voids which are interspersed between arrays of fibrils. The mechanical integrity of material is retained even with the formation of the craze, suggesting that a craze still has a load carrying capacity. The detection of crazing in semi-crystalline polymers took a while longer to uncover due mainly to the more complex nature of the microstructure features which also required a high constraint condition to encourage the formation of a craze. Nevertheless, the occurrence of crazing in semi-crystalline polymers, particularly in polyethylene, is indisputable (Chan and Williams [1983] and Bhattacharya and Brown (1985)).

Figure 2.3 A typical craze structure.

2.3.1 The role of crazing in SCG

Many authors, most notably Brown and co-workers have performed extensive studies investigating the SCG process. It is generally accepted that the formation and breakdown of the craze that precedes the advancing crack front controls the onset of crack growth in polyethylene, particularly in SCG. The conventional crazing process during SCG is illustrated in Figure 2.4. It is clear that crazing plays a crucial role in governing the fracture process. Therefore, an understanding of craze kinetics would help in explaining the reasons behind why one polymer has a high fracture toughness but another a low one (Lu *et. al.* [1988]). Consequently, the focal point in the

assessment of the long term performance of polyethylene pipe concentrates on obtaining an accurate characterisation of the craze behaviour (Lu and Brown [1997], Beech *et. al.* [2001b] and Hamouda *et. al.* [2001]).

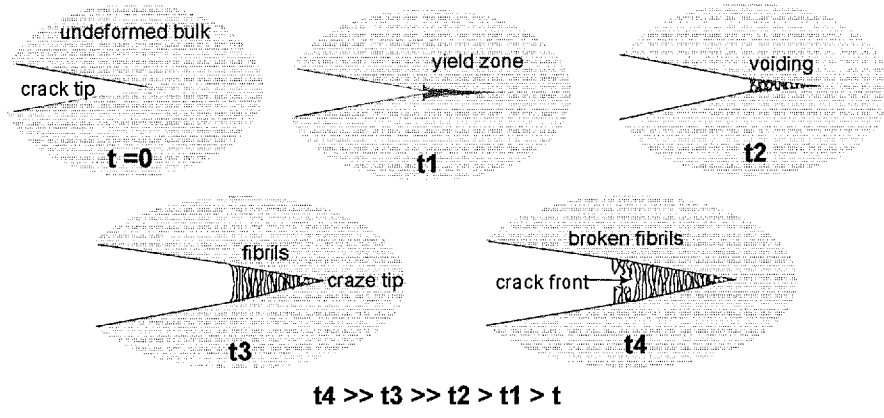

Figure 2.4 The crazing process during SCG.

2.3.2 Mechanics of craze deformation

Once a craze is initiated, the manner in which it spreads into the undeformed polymer is thought to be via the meniscus instability mechanisms as suggested by Argon and Salama [1977] and illustrated in Figure 2.5. The finger-like growth occurs due to the density differences between the phases and can be thought of as the propagation of a low density voided structure of the craze into the denser, undeformed matrix (Donald [1997]).

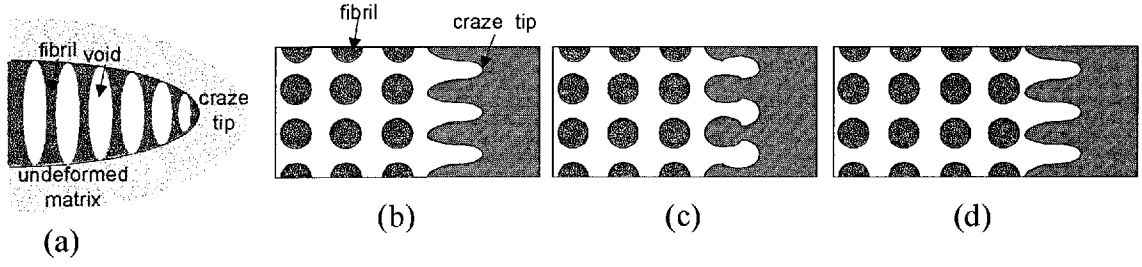

Figure 2.5 Generation of void-fibril structure by the meniscus instability mechanisms. (a) Side-view of the void-fibril structure. (b) to (d) Sequence of the propagation of a craze tip viewed from above, leaving behind isolated fibrils. (*after* Donald [1997]).

As the craze grows in length, it also widens in the direction of the tensile load by drawing new material from the dense polymer into the new fibrils, a process known as surface drawing (Hui and Kramer [1995]). In this manner, the craze may not weaken as

it widens, thus maintaining the average extension ratio constant for a given surface area. The fibrils eventually fail at the craze-bulk interface by chain scission or disentanglement as shown in Figure 2.6. In chain scission or pullout, the chain is broken/pulled free at the entanglement point while the entangled chain is unravelled during the disentanglement process.

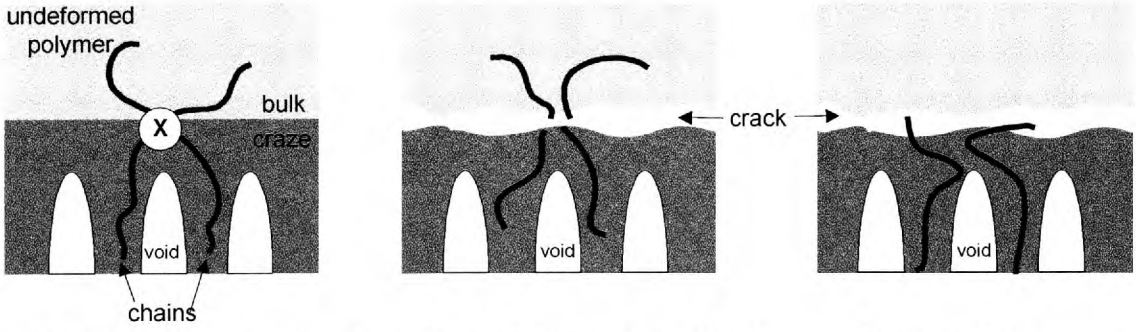

Figure 2.6 A schematic illustration of the surface drawing mechanism during craze growth. (a) Chains entangled at point "X". Entanglement loss by (a) chain scission or (b) chain disentanglement. (*after* Donald [1997]).

It is also possible that the growth of the fibrils take place via the creep mechanisms as shown in Figure 2.7 (Cawood *et. al.* [1993] and O'Connell *et. al.* [1995]). Consequently, the craze weakens progressively as the surfaces separate with failure occurring at the fibrils midrib. In polyethylene, the craze widening process is likely to involve both of the surface draw and fibril creep mechanisms.

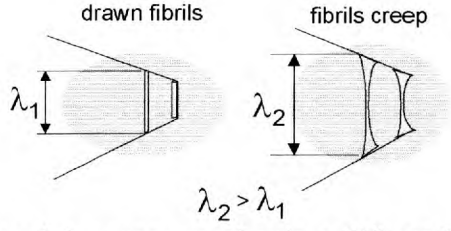

Figure 2.7 Fibrils growth by creep mechanism. Where λ is the drawn ratio.

2.3.3 Factors affecting SCG resistance

After the formation of the craze, the ability of the fibrils to continue supporting the load is likely to control the failure time. This could form a significant portion of the total failure time of the structure and hence influences the SCG performance. The SCG

resistance in polyethylene is generally recognised to depend on the ability to minimise fibrillar creep and to resist the molecular disentanglement processes. Several studies pointed out that the SCG resistance of a medium density polyethylene (MDPE) is superior to that of the high density polyethylene (HDPE) due to its better ability to resist chain disentanglement. A study by Lu *et. al.* [1988] found that the SCG performance in MDPE was indeed improved because of an increase in resistance against the disentanglement processes. The superior performance was attributed to the presence of side branch chains in MDPE. The findings are consistent with results reported in the literature on the effect of branching on the SCG performance (Bubeck and Baker [1982] and Egan and Delatycki [1995]). The fact that the disentanglement becomes more difficult with a branched chain as opposed to a smooth chain is due to the chain sliding. It seems obvious that pulling a branched chain through the crystalline regions of the fibrils would be more difficult than pulling through the relatively smooth chain as illustrated in Figure 2.8. As a result, the SCG performance is enhanced by branching, which delays the onset of crack growth by hindering the disentanglement processes.

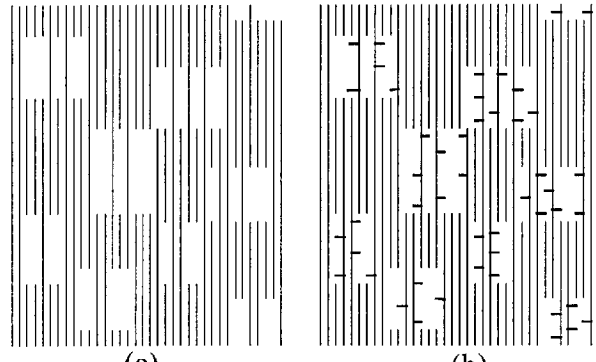

Figure 2.8 Schematic structures of highly oriented polyethylene: (a) for branch-free chain and (b) for branched chain. Light areas are amorphous region. (*from* Lu *et. al* [1988])

Resistance to SCG in polyethylene is also known to increase with increasing molecular weight (Nunes *et. al.* [1982] and Lagaron *et. al.* [2000]). This is because the higher molecular weight molecule has a greater probability of forming entangled networks. Moreover, the concentration of tie-molecules spanning the amorphous region is likely to increase. Additionally, a longer chain would pass through a larger number of lamellar crystals (Brown and Ward [1983]). Therefore, it would become more difficult to pull molecules through the crystalline lamella and to disentangle the chains in the

amorphous region. Pandya [2000] proposed that the optimum SCG resistance would be achieved through the combination of a high molecular weight and a judicious degree of chain branching.

2.4 Cohesive zone methodology

Linear Elastic Fracture Mechanics (LEFM) has proved a useful tool for characterising the fracture of a cracked body under load provided the nonlinear zone ahead of the crack tip is negligible. However, a number of studies performed previously by several authors (Narisawa and Takemori [1989] and Duan [1996]) reported the difficulties in applying LEFM in ductile polymers. The work of Chan and Williams [1983] provided one of the first known cases. They proposed that the rate of SCG could be described by:

$$K \propto \text{å}^n \tag{2.3}$$

Where K is the stress intensity factor, å is the crack speed and n is the slope of the K- å curve. However, the relationship was only rigorously true for high density polyethylene. As can be seen from the Figure 2.9, the slope (or n) approached infinity at high K and å values for the tough polyethylene tested in Comprox 2% at +75°C, which invalidated equation (2.3).

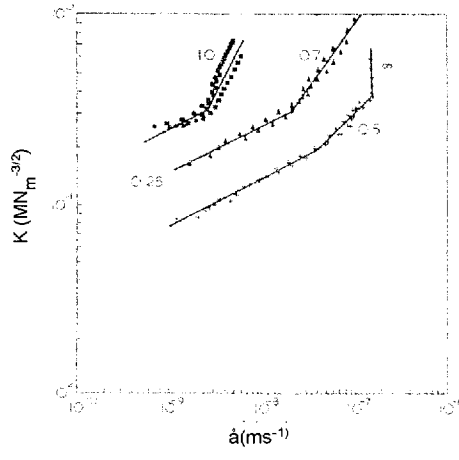

Figure 2.9 K- å curves for tough polyethylene in two different environments at various temperatures: (■) in distilled water at +80°C; (▲) in Comprox 2% at +60°C; (+) in Comprox 2% at +75°C. Numbers alongside curves indicates slopes of respective lines. (*from* Chan and Williams [1983]).

In later work, it was found that the energy released in tough polyethylene during ductile crack growth leads to the creation of a large crack tip plastic zone (Duan [1996]). Consequently, the K and J -fields underestimated the severity of the crack and provided an incorrect characterisation of the fracture properties. The validity of such an approach becomes questionable. Furthermore, the description of the near crack tip stress and strain conditions based on a single parameter treatment appears inadequate under conditions of widespread yielding.

Therefore, a useful starting point to assess the applicability of LEFM is to consider the size of the fracture process zone. If the size of the zone at the crack tip is small in comparison to the size of the crack and the size of the specimen or to the size of the crack tip stress field (i.e. K-field), then the strength can be predicted using LEFM. On the other hand, if the size of the nonlinear zone - due to plasticity or crazing - is not negligible in comparison with other dimensions of the cracked geometry then the cohesive forces that exist in the fracture process zone must be taken into account and LEFM cannot be used. Moreover, even for brittle materials, where the process zone can be lumped into a single point, the presence of an initial crack is still required for LEFM to be applicable. This would mean that bodies with blunt notches, but no cracks, cannot be analysed using LEFM.

In recent years, the cohesive zone model (CZM) has been put forward to address the limitation associated with LEFM. The origin of cohesive zone concept can be traced to Dugdale [1960] however, his work was perceived at that time as the crack tip plastic zone analysis. Another notable early contribution to this technique came from Hillerborg *et. al* [1976] who has pioneered the use of cohesive model in concrete by introducing the concept of fracture energy into the methodology. The authors were able to represent simply and reliably a number of traction-displacement relationships for concrete and hence emphasised further the elegance, simplicity and appropriateness of the cohesive crack model.

The principle behind the cohesive zone (CZ) concept or traction-separation (TS) law is to define a relationship between the cohesive force and the separating surfaces within the fracture zone. In other words, the cohesive zone idealised the fracture process in solids as occurring within thin layers confined to a line segment or a narrow strip where material degradation and separation occur as illustrated in Figure 2.10. The key

assumption of the model is the accumulation of damage (e.g. crazing) and other inelastic effects in the fracture process. It is common to assume that the cohesive stress depends only on the local opening and that a critical opening exists beyond which the cohesive stress vanishes. A material point on this interface is therefore initially undamaged but as the traction across the interface reaches some critical level it starts losing cohesion and gradually softens until a traction-free surface is created. The loss of cohesion, and thus crack initiation/extension within the solid may be regarded as the deterioration of otherwise intact tension and shear stresses across the adjacent (interface) faces.

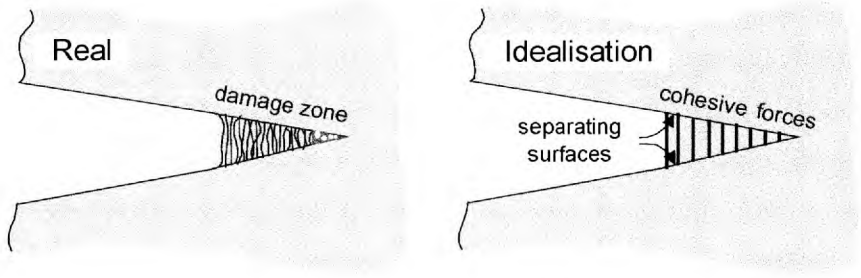

Figure 2.10 Representation of the fracture process zone by the cohesive zone concept.

The cohesive zone concept viewed the crack growth resistance of a structure as the sum of energy dissipated in the plastic zone and the work spent in the actual separation process. There is however, no "universal" cohesive/traction-separation law given a priori: the cohesive zone is a phenomenological model which does not claim to model the real physical mechanisms of the fracture process. Because of this, the choice of the cohesive law is basically free as there is no explicit correlation between the law and the results of the analysis. The cohesive zone model is therefore a general model which, in theory, is applicable to any materials that exhibit crack tip plastic zones that resemble a line segment or band-like cohesive zones. Consequently, the approach has becomes particularly attractive for modelling the failure process zone that are long in one dimension but small in the perpendicular direction.

The concept is gaining widespread reviews recently because the formulation of the model is relatively straightforward. Furthermore, the fundamental phenomena of the fracture behaviour of the structure could be described without the need to model the individual mechanisms. However, a review of the cohesive zone applications, to be

discussed in §2.4.3, reveals that the methodology constituted an area of research where the experimental investigations lag behind the computational work.

2.4.1 Parameters affecting the cohesive zone

The material parameters required for characterising the cohesive zone are peak separation stress, σ_{max} and the energy of separation, Γ. The critical separation δ_{break} between two separating surfaces when the traction stress has dropped to zero, is not an independent parameter because $\Gamma \propto \sigma_{max}\delta_{break}$, where the constant of proportionality depends of the shape of the traction-separation curve. This relationship therefore represents the physical processes of material deterioration in the fracture process zone. Figure 2.11 depicts the relationship between the cohesive parameters.

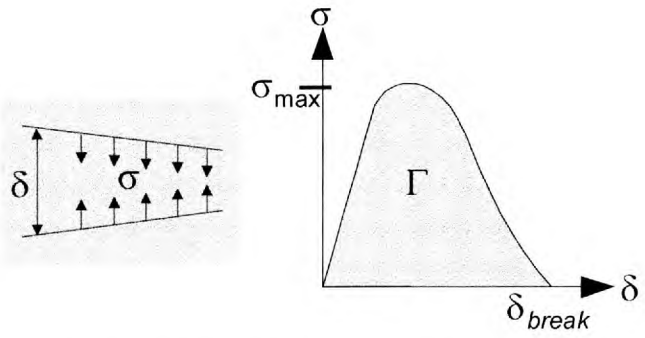

Figure 2.11 The cohesive zone model and the traction-separation curve.

As can be seen in the Figure 2.11, σ_{max} denotes the maximum traction that can be sustained within the cohesive zone. The area under the curve Γ, defines the work required for the creation of new crack surface or a unit area of a fully developed crack. In this manner, the fracture is described by a failure criterion locally at the crack tip and the interaction of this criterion with the description of the surrounding material determines the macroscopic toughness of the structure under the investigation.

The traction-separation curve is also known to be affected by some macroscopic parameters such as crack tip constraints resulting from geometry and the loading rate. This was demonstrated by Siegmund and Brocks [1999] in a numerical study that the parameters of cohesive zone in ductile materials were influenced by the triaxiality of the stress state while Ting *et. al.* [2003a, b] provided extensive experimental data to support

the findings. Both studies showed that the σ_{max} increases with increasing constraint whereas δ_{break} is large at low triaxialities and decreases with increasing constraint. Pandya and Williams [2000b] measured the traction-separation properties for a range of polyethylenes at various rates and concluded that the cohesive parameters were dependent on the loading conditions. The evidence suggests that the cohesive process is not independent, neither from the global constraint nor throughout the crack growth history. It thus showed the attractiveness of the cohesive zone approach to fracture problems in that the linkage between the cohesive zone properties and crack growth resistance can be established.

2.4.2 The Dugdale model

The work performed by Dugdale [1960] to analyse a narrow slit in an infinite plate presented one of the earliest efforts in cohesive zone modelling. According to the Dugdale theory, yielding at the crack tip would extend the length by a distance, c as shown in Figure 2.12. As can be seen c defines the plastic zone length and the normal stress along the zone is assumed to be constant and equal to σ_c. By allowing the crack to yield with the formation of the plastic zone ahead, the stress singularity at the tip was removed. Hence, an expression for predicting c can be derived by relating the parameters of the plastic zone to the applied load as follows:

$$c = \frac{\pi^2 \sigma^2 a}{8\sigma_c^2} \tag{2.4}$$

Where σ is the applied stress, σ_c is the compressive stress and a is the crack length. It is rather obvious that the line shaped plastic zone or narrow strip ahead of the crack tip proposed by Dugdale resembled that of the craze zone in a polymeric material more closely than that of the circular shape (under plane stress condition) or the kidney shape (under plane strain condition) predicted by the elastic stress field solutions given in Figure 2.13.

Consequently, many authors adopted the Dugdale model to describe the crack tip craze zone in polymeric materials. For example, Marshall *et. al.* [1973] suggested the use of Dugdale theory to predict the craze stress in polystyrene. Brown and Lu

[1995] derived a theoretical equation based on the Dugdale model to predict the SCG rate in polyethylene. Riemslag [1997] reported a good correlation between the measured craze dimensions (length) and those predicted by equation (2.3). Others gave a useful discussion on its application to model the crack tip craze zone (Donald [1997], Kinloch and Young [1983] and Ward [1983]). However, the Dugdale model does not take into account the stress concentration at the crack tip (Hui and Kramer [1995]).

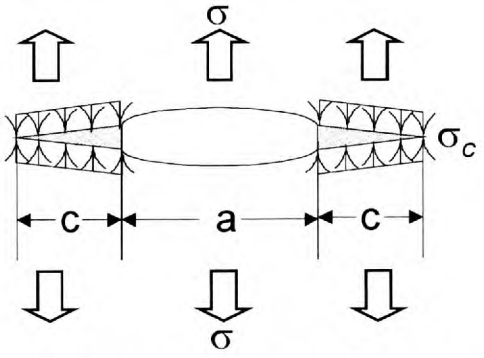

Figure 2.12 Dugdale plastic zone strip model.

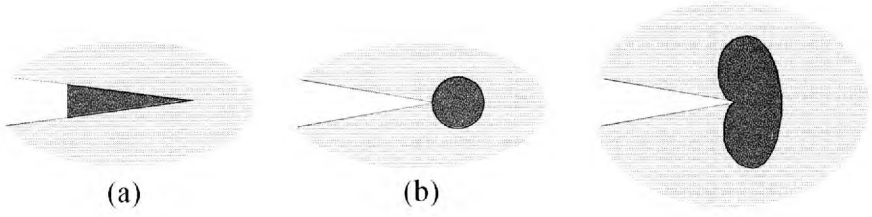

Figure 2.13 Shape of crack tip plastic zone (a) line zone, (b) circular zone and (c) kidney shaped zone.

Interestingly, in the current context of cohesive zone modelling the ideas put forward by Dugdale led to the simplest type of cohesive zone model as illustrated in Figure 2.14. According to the model, the material remains elastic until a critical stress σ_{max} is reached which corresponds to the failure strength of the material. At the peak load, the damage is initiated ahead of the crack front and continues to grow in size while σ_{max} remains constant with increasing displacement (time). When the displacement reaches a critical value δ_{break}, σ_{max} is assumed to vanish instantaneously along the crack plane, leading to the creation of a traction-free crack face. The Dugdale CZM thus cannot describe adequately the fracture behaviour of material which exhibits a strain-softening response.

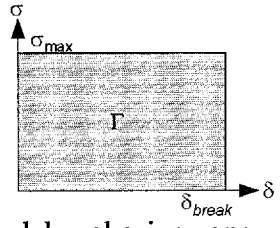

Figure 2.14 Dugdale cohesive zone model

2.4.3 Application of the cohesive zone model

The appeal of the cohesive zone model is reflected by the vast amount of literature available on the subject covering a wide range of topics and materials. Hillerborg [1991] provided a useful review on the cohesive modelling technique and offered suggestions for the implementation in concrete, fibre reinforced concrete, rock, fibre reinforced plastics, wood and metal. A recent publication of Elices *et. al.* [2002] described the application in a range of engineering materials and addressed the advantages, limitations and challenges facing the methodology. In other work, Williams and Hadavinia [2002] examined the analytical solutions of various popular cohesive laws for cantilever beam specimens. The crazing (initiation, widening and breakdown) in amorphous polymer was modelled by Tijssens *et. al.* [2000]. The validity of the model was demonstrated through the simulation of crazing around a circular hole and compared it to the results obtained experimentally. To account for the mixed-mode fracture in T-peel and single lap-shear adhesive joints, Yang and Thouless [2001] developed a mode-dependent CZM and obtained a good correlation between the experimental observation and numerical prediction of the fracture. To capture the rate-dependency of failure in adhesive bonds of the double cantilever beam, Xu *et. al.* [2003a,b] introduced a rate-dependent CZM based on the standard linear solid material model. Using cohesive parameters inferred from global measurement and a micromechanical model, the simulation of crack growth behaviour of thin sheet specimens of high strength aluminium alloys was evaluated by Li and Siegmund [2001]. Tvergaard and Hutchinson [1992] proposed a generic traction-separation relation of the form in Figure 2.15 to model the fracture process (void growth) in ductile metals.

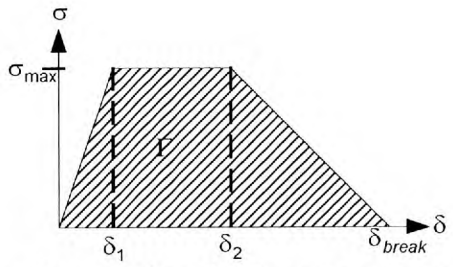

Figure 2.15 Traction-separation relation for fracture process. The separation law is fully specified by cohesive energy Γ, peak stress σ_{max} and the shape parameters δ_1/δ_{break} and δ_2/δ_{break} (*from* Tvergaard and Hutchinson [1992])

However, few studies have been done on the direct determination of the cohesive law. Instead, most of the work obtained the cohesive parameters through some type of identification procedure (Que and Tin-Loi [2002]) or an inverse analysis (Hong and Kim [2003]) (see also the reviews in the proceeding paragraph). The main difficulty resides in the fact that there are various inaccuracies about the way the cohesive parameters are obtained experimentally. For most test configurations, it is difficult to avoid crack growth or to obtain a uniform stress in the specimen. Duan and Williams [1998] overcame these problems, while characterising the fracture properties of tough polyethylene, by introducing a circumferential notch on a rectangular bar and in doing so confined the crazing in the ligament. It was showed that the damage evolution across the width of the specimen was uniform. For this reason, it was possible to postulate some form of traction-separation relationship (Pandya and Williams [2000a,b]). Subsequently, the scheme was extended to measure the cohesive laws as a function of rate and constraint in a range of polyethylenes. The technique is shown schematically in Figure 2.16. The load cell was used for measuring force whereas δ was obtained through a mechanical extensometer. Recently, Ting *et. al.* [2003a,b] enhanced the method by introducing a video (non-contact) extensometer to measure the material separation.

Figure 2.16 Direct determination of the cohesive law using a mechanical extensometer.

The scheme has proved attractive in that it provided the actual and physical link between the cohesive law and the local fracture process (or the specific experimental measurements). A reasonable correlation was obtained between the measured and predicted crack growth in polyethylene when the measured cohesive curves were incorporated as the local fracture criterion in a numerical scheme (Pandya *et. al.* [2000,2001] and Ivankovic *et. al.* [2003]).

Chapter 3

Materials, preparation and experimental procedures

3.1 Materials under review

Four different grades of polyethylene provided by BP Chemical Ltd were studied. The selection comprised of one homopolymer and three copolymers. HDPE is a high-density homopolymer whereas BMPE is a grade used for blow moulding applications. The other two grades, namely PE80 and PE100 are pipe materials. Amongst the materials, the pipe materials are known to be the toughest. However, the pipe materials do not represent the fully formulated products. Instead, these materials are representative of the type of ex-reactor product used as a basis for pipe applications. Their properties are listed in Table 3.1.

PE types	ρ (kg m^{-3})	SCB (/1000C)	M_w (g mol^{-1})	M_n (g mol^{-1})	P_D	% M $<10^4$	% M $>10^6$
PE80	940	4.5	185,000	14,000	13.2	11.6	4.7
PE100	947	2.5	310,000	11,000	28.2	15.9	10.6
BMPE	947	1.5	290,000	22,000	13.2	9.3	6.2
HDPE	954	0	355,000	20,400	17.4	7.8	7.3

Table 3.1. The properties of PE studied. Where ρ is the density, SCB is the side chain branch density, M_w is the weight average molecular weight, M_n is the number average molecular weight, P_D is the polydispersity, % M $<10^4$ is the percentage of low molecular weight material and % M $>10^6$ is the percentage of high molecular weight material. Data supplied by BP Chemical Ltd.

According to Table 3.1 the copolymers have side chain branches added to the main chain and Figure 3.1 shows a schematic presentation of the branch construction.

The presence of these branch points hinders crystallisation, which leads to a lower ρ value in the copolymers as compared to the branch-free HDPE.

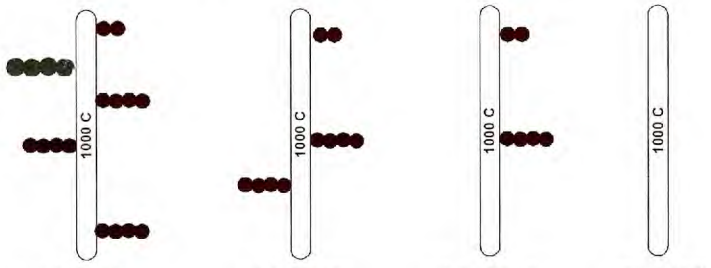

Figure 3.1 Branch structure of (a) PE80, (b) PE100, (c) BMPE and (d) HDPE. The SCB content is indicated in brackets. □ – main chain (ethylene monomer) • – side chain branch (hexane monomer).

In addition, the molecular characteristics are different between the materials and their molecular weight distributions (MWD) are shown in Figure 3.2. It can be seen that PE100 has the broadest MWD and this is reflected in the polydispersity, P_D value given in Table 3.1. Also, PE100 has the largest fraction of low and high molecular weight material with the curve skewed towards higher M. In contrast, PE80 showed a narrower MWD whereas BMPE and HDPE have very similar MWD.

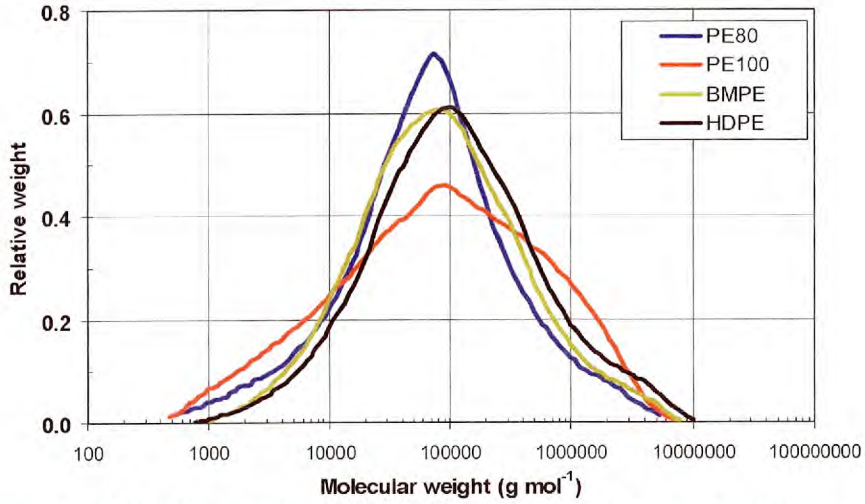

Figure 3.2 Molecular weight distributions (MWD) of the polyethylene grades. Data supplied by BP Chemical Ltd.

Data obtained in the previous work (Pandya [2000]) demonstrated conclusively that the SCG resistance of PE100 is the highest followed by PE80, BMPE and HDPE. The present work does not dispute the validity of this evidence. Here, the choice of

material forms a basis for comparing the damage behaviour between the grades to highlight the influence of the molecular features and specimen geometry on the micromechanisms.

3.2 Specimen preparation

A common source of error during testing can usually be traced to poorly prepared specimens, in addition to the experimental set-up and procedures. Therefore, the preparation of the specimen has to be carefully undertaken as an integral part of error-free experimental work. The present investigation required the dumbbell tensile specimen and the circumferentially notch tensile (CNT) specimens.

3.2.1 Dumbbell specimen

The dumbbell specimens were supplied as compression-moulded with a thickness of 1.5mm and a 70mm gauge length. The dimensions are given in Figure 3.3.

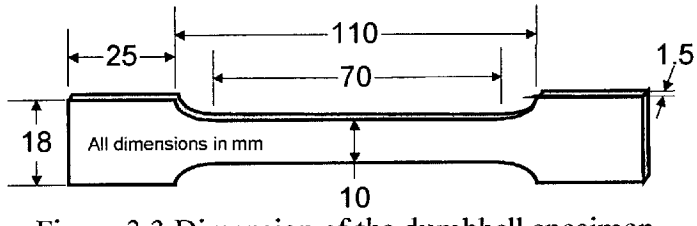

Figure 3.3 Dimension of the dumbbell specimen.

3.2.2 Circumferentially notched tensile (CNT) specimen

The second test specimen used in the experiment is the circumferentially notched tensile specimen developed by Duan and Williams [1998]. The specimens were cut from compression moulded sheet in the forms of rectangular bars with the following dimensions (a) 10 x 10 x 110mm, (b) 16 x 16 x110mm and (c) 20 x 20 x110 mm. The specimen geometry was changed by introducing three different notch depths for each bar. The notch depth was determined by calculating the ligament to bulk area (LBA)

ratio at 10%, 30% and 50%. Table 3.2 summaries the various dimensional values of the CNT specimen and Figure 3.4 shows a schematic of the specimen.

Bar size (mm)	*a*1 (10% LBA ratio)	*a*2 (30% LBA ratio)	*a*3 (50% LBA ratio)
10 x 10x 110	3.2 mm	1.9 mm	1.0 mm
16 x 16x 110	5.2 mm	3.1 mm	1.6 mm
20 x 20x 110	6.4 mm	3.8 mm	2.0 mm

Table 3.2. Notch depth values. Where *a* is the notch depth and LBA is the ligament to bulk area ratio.

A lathe was used to produce the symmetrical notch using a single point cutting tool of tip radius ≤ 20μm as shown in Figure 3.5. During notching, the spindle speed was set to 70 RPM with a feed rate of 2mm/min. Notching stops when the correct feed (notch) depth was reached indicated on the feed dial indicator. The quality of the notch depth produced by this method was controlled to within ± 10% of the nominal value with a 20° notch angle as shown in Figure 3.6.

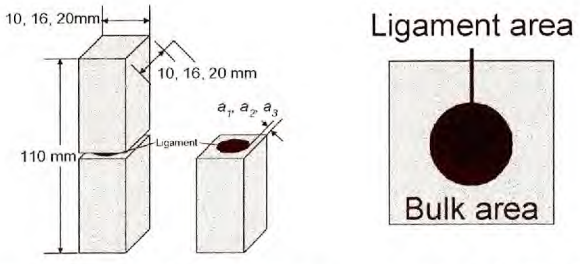

Figure 3.4 The CNT specimen. Where *a* is the notch depth.

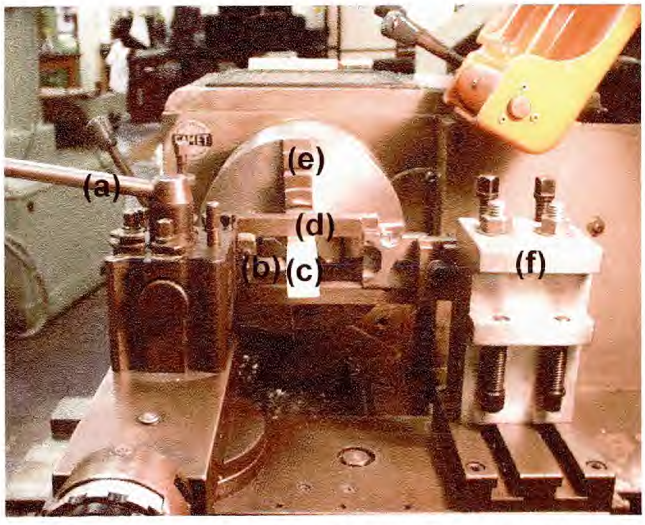

Figure 3.5 Lathe set-up for notching. (a) Tool post, (b) cutting tool, (c) specimen, (d) notching jig, (e) self-center 4 jaws chuck and (f) notch jig post.

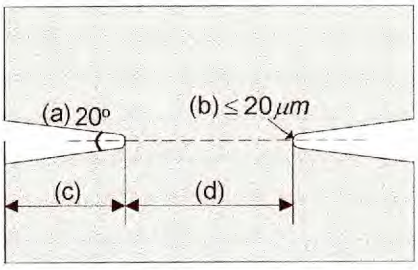

Figure 3.6 Notch tip geometry. (a) Notch angle, (b) notch tip radius, (c) notch depth and (d) ligament diameter.

The notch tip produced has to be sharp to inhibit any plane stress effects on the subsequent damage behaviour. Lu *et. al* [1991] provided constructive analyses on the various notching techniques and its effects on the notch-affected layer on the slow crack growth behaviour. The present study achieved the notch tip sharpness by using a single-point cutting tool. The sharpness of the tool tip is in turn preserved by sharpening the tip after every approximately 300 mm of cut distance. For this purpose, a tool sharpen jig is used to sharpen the cutting tool on a grinder, as shown in Figure 3.7.

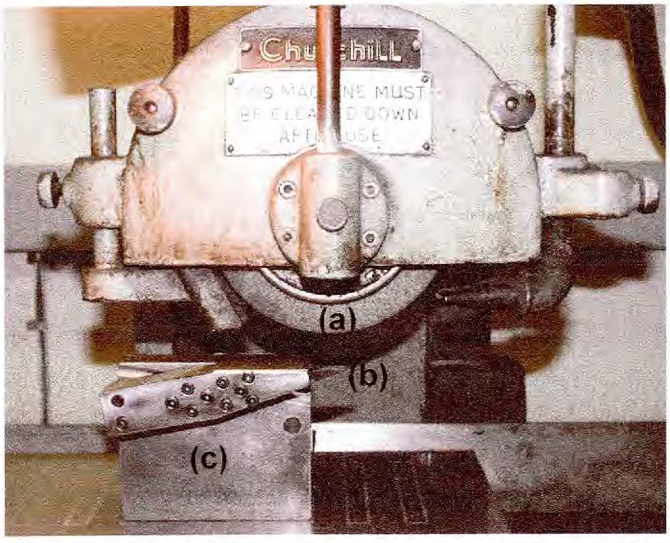

Figure 3.7 Jig set-up on a grinding machine to sharpen the cutting tool. (a) grinding wheel, (b) cutting tool and (c) tool sharpen jig.

3.3 Experimental procedures

All experiments were carried out on a screw-driven Instron machine with a moving crosshead, in a controlled environment at 22°C ± 2°C. A standard 10kN load cell was

used to measure the load under constant crosshead speed. The specimen was mounted onto the machine using the Instron standard screw-driven jaw grips.

3.3.1 Tensile test

In the uniaxial tensile test, the dumbbell specimen was employed to obtain the engineering stress-strain data. The extension of the specimen was measured by the crosshead with the initial gauge length defined at 70mm. A schematic presentation of the test set-up is shown in Figure 3.7. The load-displacement data extracted from the test was used to calculate the engineering stress and strain in accordance with:

$$\sigma_{eng} = \frac{P}{A_0} \tag{3.1}$$

$$\varepsilon_{eng} = \frac{l_f - l_0}{l_0} = \frac{l_{xhead}}{l_0} \tag{3.2}$$

Where σ_{eng} is the engineering stress, P is the load, A_o is the initial cross-sectional area, ε_{eng} is the engineering strain, l_f is the final gauge length, l_o is the initial gauge length and l_{xhead} is the crosshead extension.

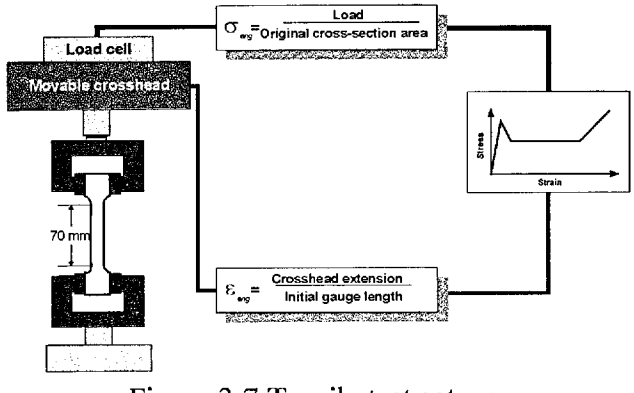

Figure 3.7 Tensile test set-up

3.3.2 CNT test

In the CNT test, the experiments were performed on circumferentially notched tensile specimens under displacement-controlled conditions. Some improvements to the original test configuration put forward by Pandya [2000] were made. One of the

changes involved the specimen gripping method. Initial observation found that the pin-hole mounting method (which was developed for gripping 16mm thick specimen with a 10% LBA ratio) was unsuitable in the current work. This is because materials deformed around the mounting holes when specimens with 30% and 50% LBA ratio were tested. Furthermore, if the hole was slanted or misaligned, as illustrated in Figure 3.8 during preparation then it is possible to introduce shear force in the test. Several alternative gripping methods were evaluated (Ting [2001]) and it was found that the Instron standard screw-driven bulk gripper overcame the problems associated with the pin-hole mounting method. To increase the gripping strength, the shallow serrated pattern of the gripper jaws was changed to parallel rows of deep V-shaped grooves of 1mm pitch. Another significant improvement made in the CNT test set-up was switching from the mechanical extensometer to a video system. One of the drawbacks with the mechanical system is the potential slippage of the extensometer during recording. In contrast, the video system is a non-contacting device. In addition, the video system is capable of large strain measurement of 50 mm extension. Previously, strain measurement was restricted to the limits of the extensometer arms travel to ± 5mm. More importantly, a gauge length of 5 mm can be defined whereas the smallest gauge length that can be used with the mechanical extensometer is 12.5mm. The selection of the gauge length is important as it can affects the accuracy of the measurement. A discussion of its effect will be given in the following section. The final configuration of the CNT test and the video extensometer system are illustrated in Figure 3.9.

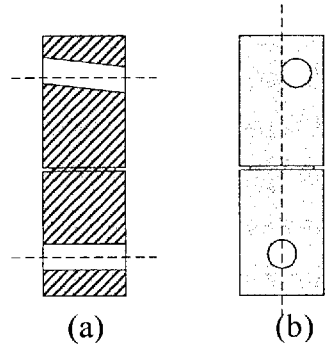

Figure 3.8 Illustration of (a) slanted hole and (b) misaligned hole.

Prior to the start of a test, the specimen was marked with a pair of dark parallel lines 5mm apart (i.e. the initial gauge length) positioned at an equal distance from the plane of the notch opening. The boundary that enclosed the likely total extension of the

specimen was then defined in the video software, as illustrated in Figure 3.10. The video extensometer records the extension of the specimen by measuring these lines at regular intervals through the lens, which converts the incident light intensity into a proportional voltage signal before being digitised into binary numbers. The load-extension data produced from the test represented the *in-situ* measurement of the traction-separation relationship and the traction-separation data were calculated using the following equations:

$$T_n = \frac{P}{A_0} \tag{3.3}$$

$$u_n = l_f - l_o \tag{3.4}$$

Where T_n is the normal traction, P is the load, A_o is the original ligament area, u_n is the normal displacement, l_f is the final gauge length and l_o is the initial gauge length.

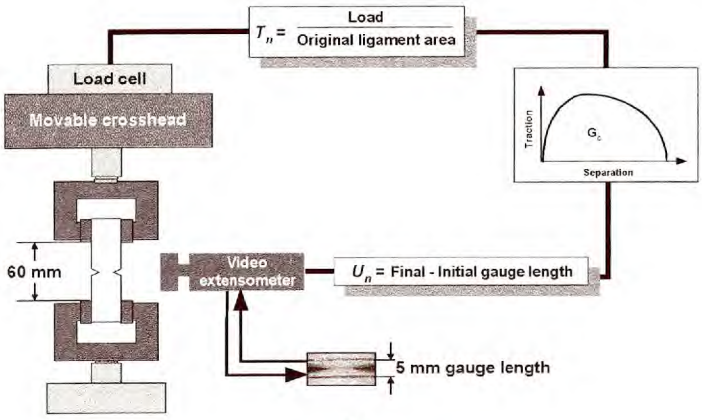

(i)

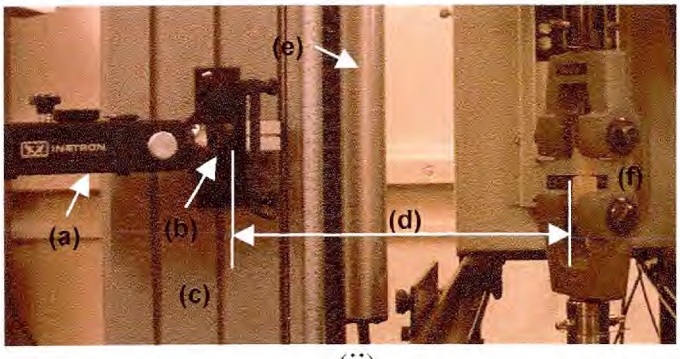

(ii)

Figure 3.9 (i) CNT test set-up and (ii) configuration of the video extensometer system. (a) Video extensometer, (b) 25mm lens with a 50mm field of view, (c) load frame column, (d) lens to specimen distance-297mm, (e) light aperture and (f) specimen.

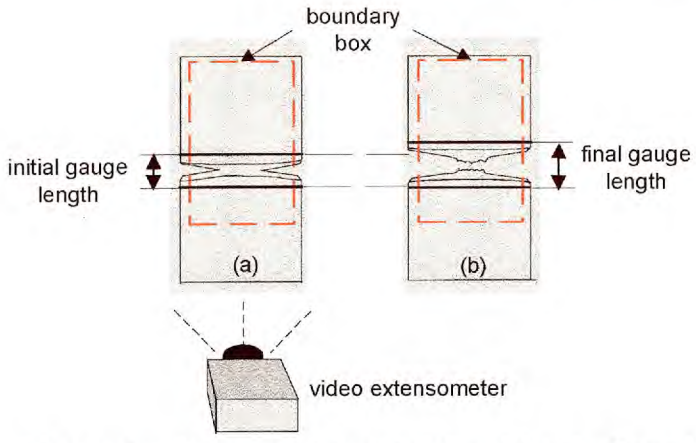

Figure 3.10 The video system's area of interest defined by the boundary box at the (a) start of test and (b) end of test.

3.3.2.1 Effect of gauge length

In earlier work Pandya [2000] showed that the disparity in the readings obtained by the mechanical extensometer and the crosshead method was attributed to the gauge length defined during the CNT test. In the case of the crosshead method, the gauge length defined was 60mm whereas it was 12.5mm with the mechanical extensometer. It was found that the displacement at the peak load obtained via the crosshead method was significantly higher than those measured using the mechanical extensometer. This was because the crosshead has included in its reading the load train slack, the test fixtures compliance and the strain contribution of the bulk material. The deduction is valid as revealed by the stress-displacement readings compared between the video extensometer, mechanical extensometer and crosshead method with gauge lengths defined at 5mm, 12.5mm and 60mm respectively, as shown in Figure 3.11. The corresponding experiment configurations are illustrated in Figure 3.12. Being an independent device unconnected to the test machine, the video and mechanical extensometer readings are not affected by the load train and fixtures compliance, unlike the crosshead which is an integral part of the test machine.

It can be seen from the Figure 3.11 that the displacement distance at peak increases with increasing gauge length. On the other hand, there is little difference in the total displacement values between the curves. In each case, the maximum stress is identical

and is unaffected by the choice of the gauge length. In contrast, the gauge length influences the pre-peak displacement significantly. It would appear that the selection of the gauge length is critical when the measurement is localised to the notch where the fracture process is confined in the ligament, as in the case with the CNT test. Given that the whole specimen accommodates large strain prior to the damage formation in the ligament it becomes imperative that the gauge length defined is as close to the height of the deformation (fracture) zone so that the strain accumulated outside the zone is not taken into the measurement. As it is not possible to estimate the height of the zone, the current selection of the gauge length is dictated by the capability of existing hardware equipment. For reasons explained in the preceding sections, the video extensometer has been selected because the smallest gauge length can be defined.

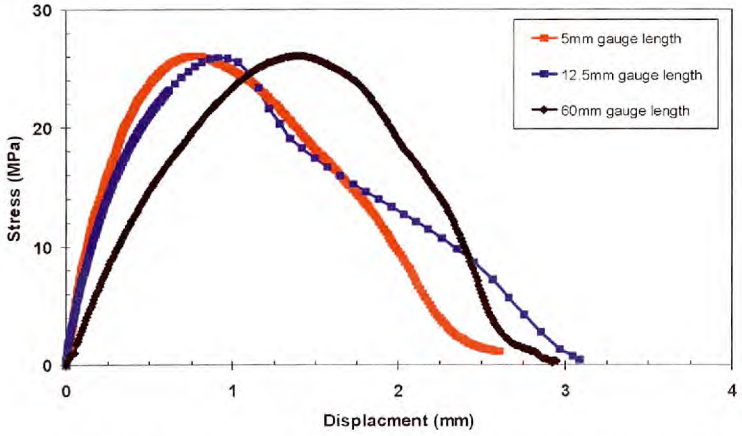

Figure 3.11 Effect of gauge length on the stress-displacement curve.

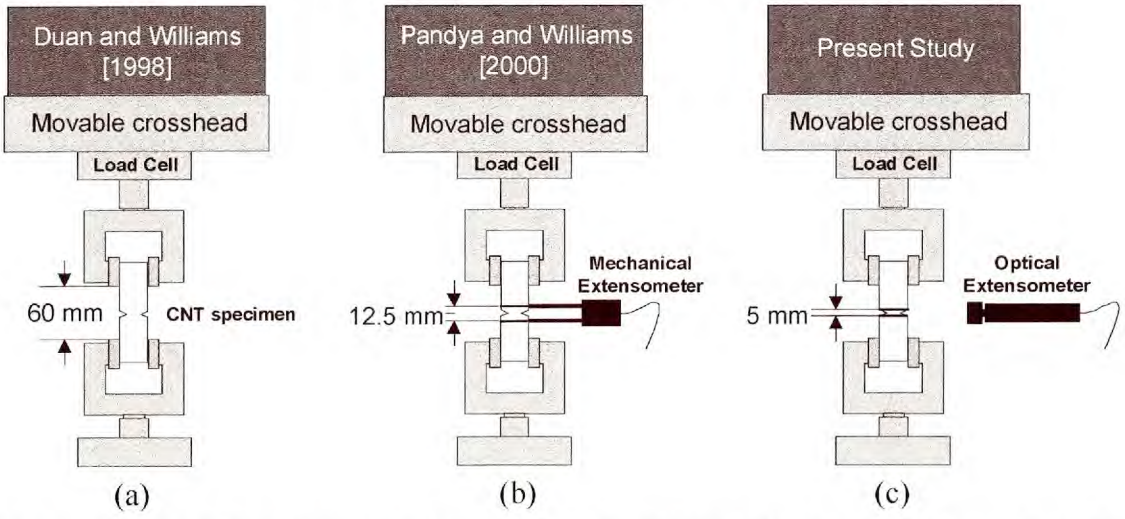

Figure 3.12 Experiment configurations using (a) cross-head method, (b) mechanical extensometer and (c) video extensometer.

3.3.3 Stop-section technique

The CNT test provided an ideal vehicle for investigating the damage (craze) structure. To be able to view the damage as it initiates and grows within the ligament requires skills and a sound technique to halt the test and section the specimen at a pre-determined load or extension. Several methods based on a similar idea have been proposed (Riemslag [1997] and Pandya [2000]). It was suggested that the specimen was sectioned in the unloaded state and then reopened with a jig to its original displacement at stop. A major drawback of such an approach was the immediate recovery of the fibrils in the damage zone upon unloading. Intuitively, it was also felt that the elastic spring back of the bulk material upon unloading could further compress the fracture (damage) zone. Furthermore, it is likely that the reopened sectioned only approximated the original opening. A recently developed stop-section method by Clutton [2002] addressed the problems associated with the former method and is adopted by the present study. The technique is illustrated in Figure 3.13.

When the test was terminated, the partially opened specimen remained on the test machine under load. Next, a G-clamp was used to protect and stabilise the notch area (damage zone) against any vibration while holes was drilled for positioning the jig. Then the G-clamp was removed to allow the jig to clamp open the specimen while it is still gripped under load. Subsequently, the specimen was removed from the machine to cut off the excess length. Finally, the specimen was sliced into halves using a razor blaze, thus exposing the damage zone in the fully opened state for inspection under the scanning electron microscope (SEM). Prior to the SEM, the specimen was coated in gold and the beam voltage was set to between 10 and 20 kV. Throughout the process, the resulting axial slices remained held open by the jig thereby providing an accurate qualitative assessment of the damage behaviour.

3.4 Conclusions

This chapter provided a review of the material properties and summarises the various procedures in relation to the specimen preparation and the experimental techniques. A video system capable of measuring strains in localised regions has been introduced into the CNT test procedure. The aim is to enhance the measurement techniques during the

deformation of the polymer. A novel stop-section method to analyse the evolution of the damage behaviour has been proposed by Clutton [2002] and adopted in the present investigation.

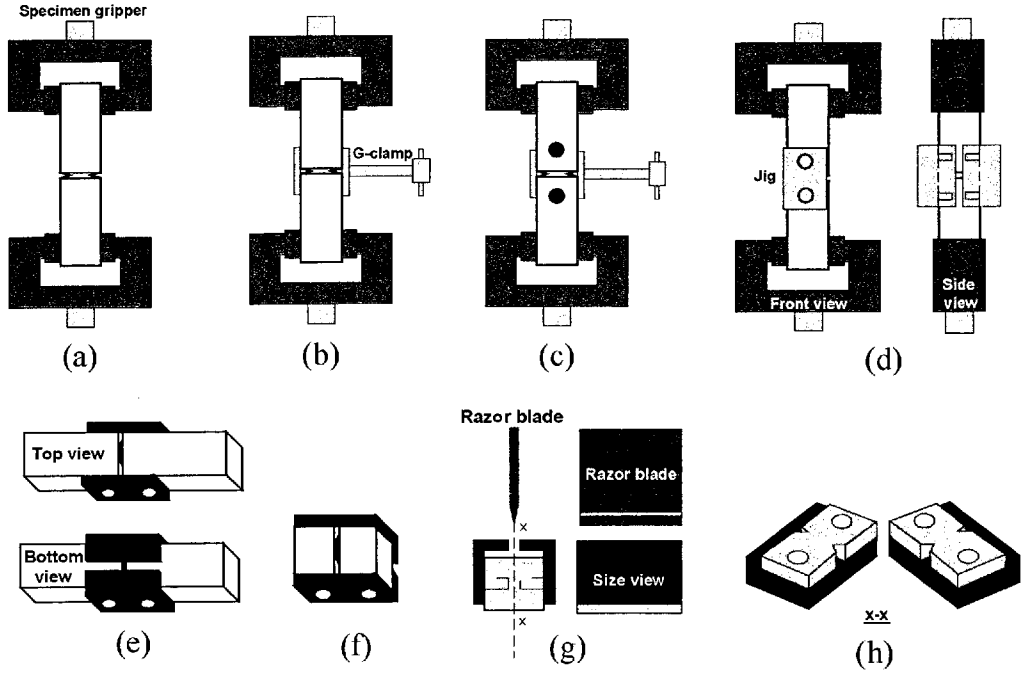

Figure 3.13 The stop-section technique. (a) Stop the test, (b) clamp specimen, (c) drill locating holes, (d) remove clamp and place jig, (e) specimen removed from machine, (f) cut-off excess length, (g) slice specimen using a razor blade and (h) specimen ready for SEM examination.

Chapter 4

The stress-strain behaviour of polyethylene

4.1 Introduction

The aim of this chapter is to characterise the material mechanical behaviour under tension and more specifically, to determine the mechanical properties under plane stress conditions. This can be accomplished by performing the tensile test which is one of the most widely employed mechanical tests for assessing mechanical properties. The appeal stems from the fact that much useful engineering information on the mechanical behaviour of the material can be obtained. A complete tensile test result would generate data on elastic properties, yield strength, ductility (toughness) and the degree of plastic deformation. However, the viscoelastic nature of polymers, which introduces time-dependent behaviour, adds another component in the test. As a result, the mechanical properties are strain rate dependent and in characterising the deformation behaviour of polymers the effects of temperature and strain rate must be included in the assessment.

4.2 Deformation under uniaxial stretching

Consider a semi-crystalline polymer sample stretched under tension at a uniform rate of extension the stress-strain curve will often assume the shape as shown in Figure 4.1. The applied stress increases steadily but begins to deviate from linearity as it approaches the yield point. With ongoing strain, the yielded material deforms further causing the nominal stress to fall drastically while a neck is formed (Figure 4.1(b)). As the neck stabilised the stress settles at a constant value and this marks the onset of large plastic deformations as the neck begins to propagate across the length of the sample, as seen in Figure 4.1(c). The plastic deformation is hindered with increasing

strain (this phenomena is known as strain hardening) and the stress-strain curve begins to rise once again until a critical limiting strain is reached where the sample breaks.

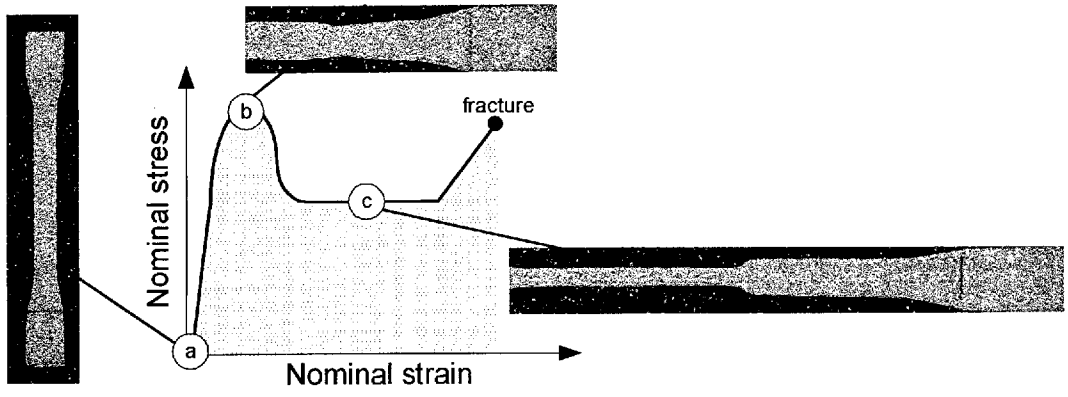

Figure 4.1 Nominal stress-strain curve. (a) Undeformed, (b) neck and (c) draw.

4.2.1 True stress-strain curves

The conventional stress-strain data (Figure 4.1), which used the original cross-section area and gauge length to compute the stress and strain respectively, is adequate provided that the strain is small and remains homogeneous. However, at large strains conventional stress-strain curve can give a misleading interpretation of the post-yield deformation. There are several reasons for this shortcoming as pointed out by Haward [1994]. Firstly, the gauge length becomes ambiguous as deformation spreads into the shoulder of the dumbbell sample. Secondly, the true strain rate is not rigorously applied during the test. More importantly the slope, at large strains, of the nominal stress-strain curve fails to measure accurately the strain hardening process because of the inhomogeneous deformation caused either by necking, crazing or shear yielding which was not taken into account in the definition of the nominal stress and strain. Therefore, a more precise definition is required for the stress and strain that consider the interrelation between gauge length and diameter changes associated with plastic deformation, as defined in the following equations.

$$\sigma_{true} = \frac{P}{A_i} \tag{4.1}$$

$$\varepsilon_{true} = \ln\frac{l_c}{l_o} = \ln\lambda \tag{4.2}$$

Where σ_{true} is the true stress, P is the load, A_i is the instantaneous cross-sectional area, ε_{true} is the true strain, l_i is the initial length, l_c is the current length and λ is the extension ratio.

The measurement of a true stress *vs.* true strain is not straightforward as compared with the conventional stress-strain curve and presents a certain amount of challenge. Much of the experimental difficulty lies in obtaining an accurate measurement of the localised extension ratio, λ. The situation becomes tricky when damage mechanisms such as necking and crazing are present. In recent years, numerous studies have looked at improving the procedure and in some cases coupled with more efficient measuring equipment. For example, Nitta and Ishiburo [2002] utilised a double edge notched geometry to eliminate the plastic instability associated with neck formation in order to achieve a uniform deformation during tensile stretching. In another study, G'Sell *et. al.* [1992] contained the tensile measurement in a confined area of the sample where deformation is effectively homogeneous while Boyce *et. al.* [1994] carried out the test in uniaxial compression to avoid the problem of necking. More recently, G'Sell *et. al.* [2002] developed a novel technique which relied on a video system to compute the volumetric strain in real time while the axial true strain rate is kept constant. The technique was applied to a glassy polymer which exhibited "diffuse" necking during the test, as shown in Figure 4.2. The drop in true stress after yielding as seen in Figure 4.2(a) corresponded to the intrinsic strain softening of the material and was not a result of any geometric artifact.

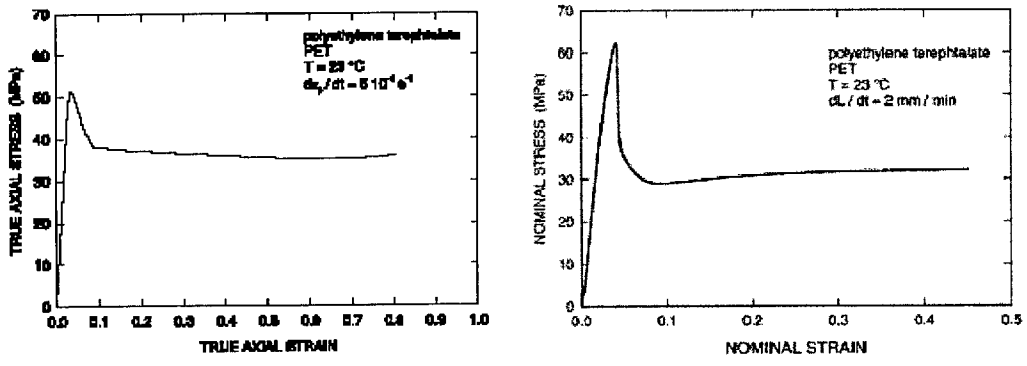

(a) (b)

Figure 4.2 (a) True stress-strain curve and (b) Nominal stress-strain curve of polyethylene terephtalate (PET). (*from* G'Sell *et. al.* [2002])

4.2.2 The mechanics of deformation under tension

The formation of the neck is regarded as plastic instability because it leads to inhomogeneous deformation and dimensional variation. In a conventional stress-strain test the necking instability is characterised by the distinct yield drop. In a true stress-strain curve, on the other hand, the plastic instability is captured as a slight fall in the true stress in a region where the stress rises less steeply with strain. Once necking begins, the longitudinal strain becomes non-uniform. In addition to necking strains, a triaxial stress state exists in the vicinity of the neck (G'Sell *et. al.* [1992]). Because of the Poisson effect stresses are induced in the radial and transverse directions. The state of triaxial tension stress distribution within the necked region acts to plastically constrain the material from further deformation in the neck. As a result, the axial stress has to be increased to accommodate the deformation. At the molecular level, necking is due to chain-like molecules being drawn out of their original amorphous or crystalline structure into an approximately linear and parallel arrangement. With continuing extension, the unfolded chains within the neck increasingly align themselves in the direction of the applied load to form long fibrils and eventually became stiffer than the surrounding material. The drastic reorganisation of a linear polyethylene structure deformed under tension is shown in Figure 4.3 (Amornsakchai *et. al.* [2002]). It can be seen that the initial spherulite shape (Figure 4.3(a)) has broken down into a fibrillar structure (Figure 4.3(b)) under tensile stretching. Consequently, the process of necking and cold-drawing leads to a non-uniform distribution of stress and strain along the length of the test specimen.

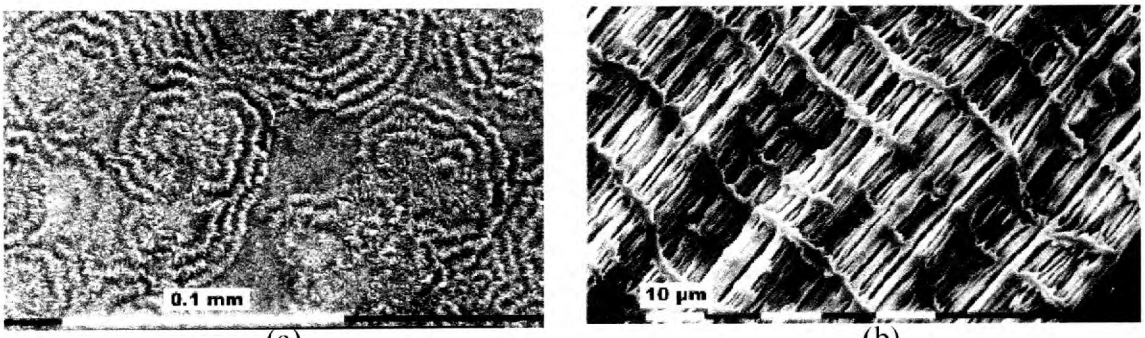

(a) (b)

Figure 4.3 SEM of a linear PE (a) Starting morphology showing banded spherulites and (b) morphology at 40x draw ratio showing a fibrillar structure (*from* Amornsakchai *et. al.* [2002]).

The results of G'Sell *et. al.* [2002] demonstrated that the source of necking instability in polymers could be traced to the nature of the damage mechanisms present. The study showed that the damage found in the necked material consisted of shear yielding and crazing (Figure 4.4 (a)-(c)). On the other hand, crazing was singled out as the only mechanism found in the "non-necking" sample (Figure 4.4 (d)). Others like, Melick *et. al.*[2003] and Unwin *et. al.* [2002] centred their studies around the molecular feature effects (strain hardening characteristics) to explain the stability of the neck formed.

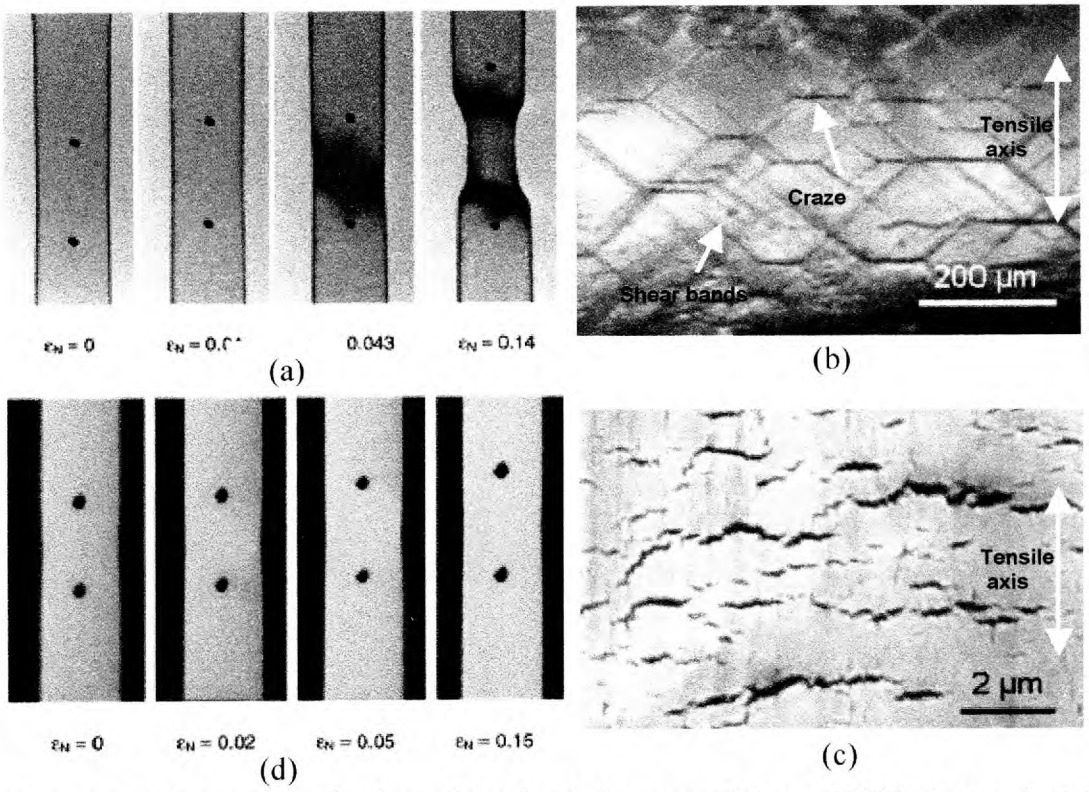

Figure 4.4 Damage mechanisms in polyethylene terephthalate(PET) shown in (a)-(c) under uniaxial tension. (a) Photograph showing microstructural process where diffuse necking is evident. (b) Transmission optical micrograph of shear bands and crazes in the shoulder of the neck in (a). (c) Scanning electron micrograph of crazes in the centre of the neck in (a). (d) Photograph showing microstructural process in high impact polystyrene (HIPS) which shows the absent of necking.(*from* G'Sell *et. al.* [2002]).

4.3 Results of tensile tests

The geometry of the dumbbell sample and the experimental set-up was explained in section 3.2.1 and 3.3.1 respectively. The samples were stretched with an Instron 4466 with fixed crosshead speeds set at between 50 mm/min (strain rate - 1.2 $x10^{-2}$ s^{-1}) and

0.005 mm/min (1.2 x10^{-6} s^{-1}). The nominal stress and nominal strain were used. The tensile stretching experiments were run to determine the influence of the strain (elongation) rate on the tensile behaviour. The present investigation is not concerned with the deformation at large strain plasticity or the strain hardening characteristics and hence conventional stress-strain experiments are adequate for determining the mechanical properties. Once yielding has been initiated, a ductile polymer is capable of huge elongation. For example, in one of the tests the sample was stretched to an elongation of 900% at a crosshead speed of 50 mm/min without failure, as shown in Figure 4.5. For practical reasons, the measurements were terminated between 40% and 100% strain depending on the crosshead speed.

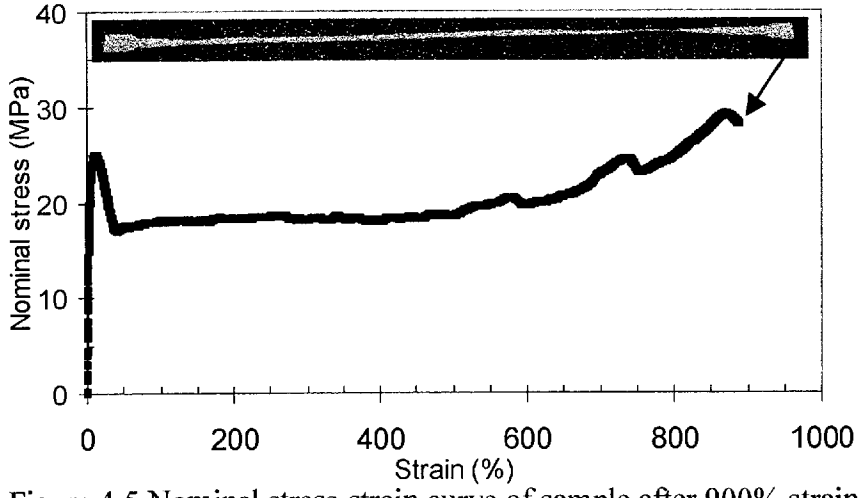

Figure 4.5 Nominal stress-strain curve of sample after 900% strain.

4.3.1 The strain rate dependence of the stress-strain curves

The results of the conventional tensile test on PE80, PE100, BMPE and HPDE at a constant elongation rate of 50mm/min are shown in Figure 4.6. At this rate, the stress-strain curves showed first a non-linear viscoelastic range up to the yield point followed by a marked yield drop while a neck is developed. The abrupt drop in yield terminated after an accumulated strain of about 0.25 for HDPE, 0.3 for PE100 and 0.35 for PE80 and BMPE. The stress eventually stabilised at the plateau and the neck cold-draws at a relatively constant load before the test was terminated at 100% strain. It can be seen from the figure that the yield point is the highest in HDPE while PE80 has the lowest point. On the other hand, the yield point of PE100 and BMPE peaked at about the same value. The high yield point observed in HDPE can be attributed to its density, which is

the highest amongst the materials (see Table 3.1). Since density is related to crystallinity which describes the state of the chains packing, hence, for a densely packed material the crystallinity would be high. On the whole, the strength and stiffness improved with increased crystallinity. However, the presence of random side branching in PE80, PE100 and BMPE inhibited crystallisation, thereby lowering its densities and affected its yield stress at this rate.

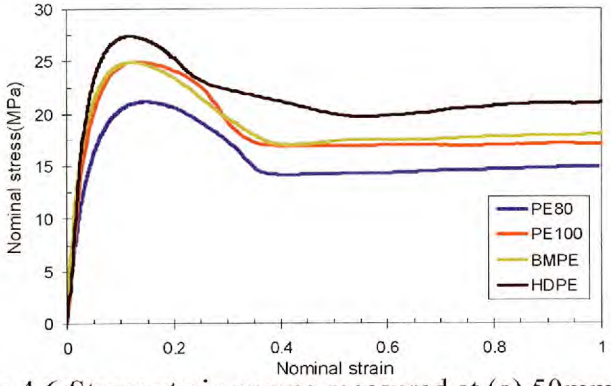

Figure 4.6 Stress-strain curves measured at (a) 50mm/min.

Another contributing factor for the high yield in HDPE is the high molecular weight. The main feature is the longer chains which are more likely to be entangled and to act as inter-crystalline links connecting several crystalline regions, thus increasing the tie molecule concentration. A high tie molecule concentration has the beneficial effect of increasing the yield stress due to the ability of the long chain to distribute the stress more effectively than a shorter chain (Channel and Clutton [1992]). Beside the density and molecular weight dependence of the yield point, side branching is also known to influence the yield behaviour. At high elongation speeds, the time given for chain slippage could be inadequate and can become progressively more demanding if the chain is branched. As a consequence, it is possible that the rate of disentanglement in a branched polyethylene is slower than the applied strain rate thereby encouraging the material to initiate yielding at a lower stress. As is the case for all branched polyethylenes the yield points are lower than HDPE with the lowest yield point found in PE80 because its side chain branch content is the highest. This point is further illustrated by Pandya *et. al.* [2003a] who suggested that chain branching is detrimental to the performance of polyethylene at high rates of extension. Figure 4.7 shows a series of stress-strain curves for all samples measured over a wide range of crosshead speeds.

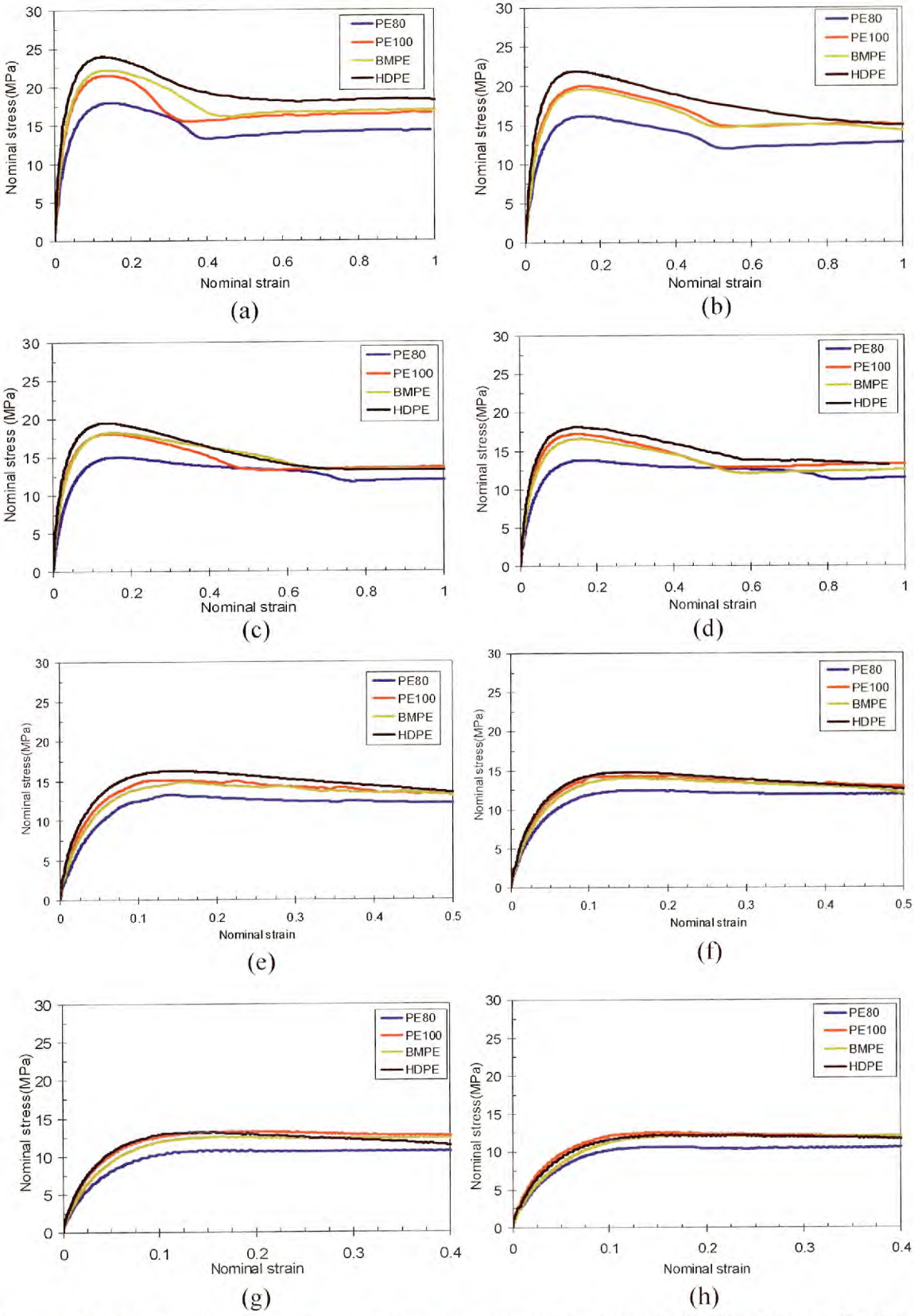

Figure 4.7 Nominal stress-strain curves measured at (a) 10 mm/min, (b) 5 mm/min, (c) 1 mm/min, (d) 0.5 mm/min, (e) 0.1 mm/min, (f) 0.05 mm/min, (g) 0.01 mm/min and (h) 0.005 mm/min.

It can be seen from the Figures 4.7(a) to 4.7(d) that the behaviour of the curves observed at these rates were similar to those stretched at 50 mm/min, in which the initial homogenous deformation gives way to an abrupt drop in yield at the elastic limit caused by diffuse necking. Once more, the yield point of HDPE remains the highest among the grades considered. However, as the strain rate is reduced all materials showed a decrease in the yield point. Furthermore, the drop in stress after the peak became more gradual as the neck evolved at a greater range of strain before stabilising.

The results for tensile tests conducted at 0.1 mm/min and 0.05 mm/min are given in Figures 4.7(e) and 4.7(f) respectively. According to the figures and within the range of strain considered, necking was absent in PE80 and PE100 while a shallow neck formed in BMPE. By comparison, a sharp neck was initiated in HDPE. The most significant features seen here is the smaller difference in the yield point between the materials. Moreover, the local maximum becomes increasingly less well defined. Figures 4.7(g) and 4.7(h) compare the stress-strain behaviour between the materials at tests run at 0.01 mm/min and 0.005 mm/min respectively. In both test conditions, the stress-strain curves showed much less instability than for test runs at higher rates. The most remarkable feature at these rates is that there is almost no necking in the samples while stretched and the deformations proceeded in an almost homogeneous manner, at least in the strain range considered. As a result, the local maximum on the stress-strain curves disappeared and the shape of the curve starts to approach the form shown in Figure 4.8.

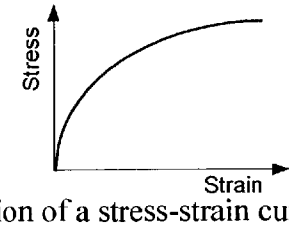

Figure 4.8 Schematic presentation of a stress-strain curve without a local maximum.

The results of Figures 4.6 and 4.7 suggested the following events. First of all, the stretching behaviour at high elongation rates (Figures 4.6, 4.7(a) to 4.7(d)) is different to those seen at lower elongation rates (Figures 4.7(e) to 4.7(h)). Tests drawn at high elongation rate illustrated the importance of density (crystallinity) to account for the superior yield strength and the shape of the curve observed. This can be seen by the

greater yield and draw strength found in the stress-strain behaviour of HDPE, which has the highest density. The behaviour is in stark contrast to PE80 where its corresponding strengths are inferior due to a lower density. In the case of PE100 and BMPE with intermediate densities, their stress-strain behaviour falls between the two extremes. In addition, plastic instability associated with diffuse necking is pronounced in all four materials. However, as the elongation rate decreases the stress-strain behaviour changed. The most significant change associated with the absence of necking or with the formation of only a shallow neck in the samples. This is manifested as a broader yield process with increasingly less defined load maximum. It can also be seen that the differences in the yield stresses of the samples with quite different levels of crystallinity (density values) is small. It appears that the effect of crystallinity became less noticeable as the elongation rate decreases. Therefore, it is reasonable to assume that while at high test rates crystallinity (density) is the most important property, at lower elongation rates the molecular entanglement, which is influenced by the molecular weight and branching, is vital in achieving a more even distribution of stress. Given that at low rates of extension, more time is provided for chains to disentangle and to align with the direction of applied stress. As a consequence, all four materials exhibited coherent drawing characteristics while stretched thereby leading to more stable stress-strain behaviour.

Figure 4.9 summaries the effect of elongation rate on the stress-strain behaviour of each material. It can be seen that the polyethylene samples exhibited stress-strain response which is sensitive to the applied rate around the yield region. The yield point of all samples decreased as elongation rate is lowered. At lower test rates, stress-strain behaviour is more stable but the local peak is less defined. According to Brooks *et. al.* [1992] the rate-dependent behaviour of the pre-yield stress-strain curve of polyethylene can be explained by two distinct processes. It was found that the polyethylene exhibited two yield points in true stress *vs.* nominal strain tests carried out at a range of temperature under constant elongations. It should be noted that the decrease in the elongation rate has an influence similar to the increase in temperature (Nitta and Ishiburo [2002]). The first yield point occurred at a low test temperature (high elongation rate) which is characterise by a marked yield drop at the elastic limit. Brooks associated the first yield point with the intrinsic softening process within the materials

and it is not due to the geometric artifact since the decrease in cross-section at the neck is already taken into account in the definition of true stress. The second yield point, on the other hand, is due to the geometric effects and became apparent at high temperature (low elongation rate) where the true stress-nominal strain curve exhibited a less defined load maximum.

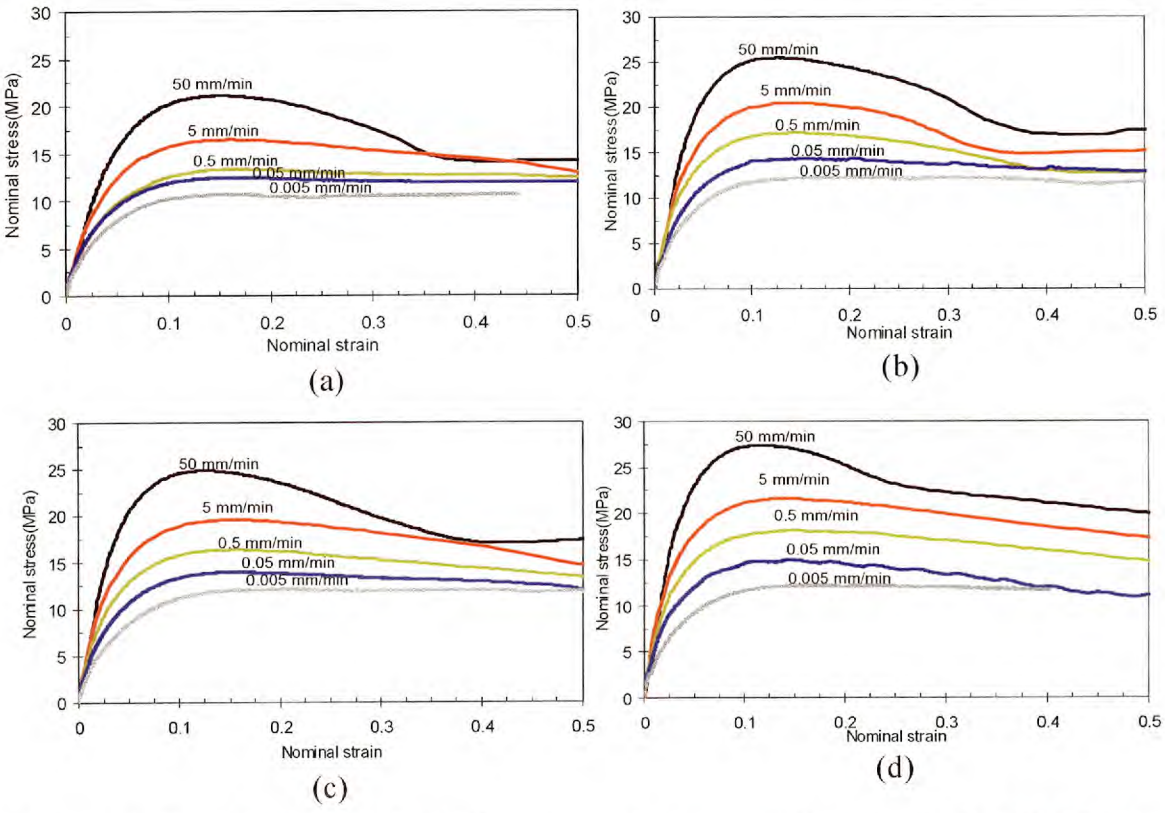

Figure 4.9 The influence of elongation rate on the stress-strain curves of (a) PE80, (b) PE100, (c) BMPE and (d) HDPE.

4.3.2 Effect of strain rate on the mechanical properties

It is generally accepted that the conventional yield stress is defined as the maximum point in the stress-strain curve. However, the stress-strain curves examined at low test rates (Figures 4.7(g) and 4.7(h)) did not show a clear local maximum. As a result, the values of the yield strain, ε_y and Young's modulus, E appear ambiguous. For that reason, another definition of yield stress is required. One approach is to determine the point where the two tangents to the initial modulus and the almost linear region at the peak, intersected as illustrated in Figure 4.10. Besides this method, an offset yield

point has also been proposed (Ward and Hadley [1993]). The former appears more accurate as it utilised the whole pre-yield curve to determine the yield point. For the sake of consistency in the results, all stress-strain curves measured used the method of intersecting lines to establish σ_y, ε_y and E.

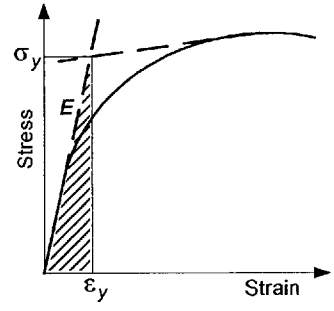

Figure 4.10 The yield stress is defined at the point where the two tangents intersect.

Figure 4.11 displays the nominal yield stress as a function of strain rate for all the samples measured. For all materials, the yield stress increases with the logarithm of strain rate and showed an almost linear rise in the stress value. In the yield measurements taken at high rate of extension ($>1.2x10^{-4}$ s^{-1}), the samples are arranged according to the value of the density as seen in Figure 4.11, with HDPE dominating the upper stress band values followed by PE100, BMPE and PE80. It is clear from the results that the higher the density of the material, the greater the value of the yield stress. The result is in agreement with Vallés and Failla [2003]. As the draw rate is reduced ($<1.2x10^{-4}$ s^{-1}), the yield value of different samples converges. The finding suggested that the effect of crystallinity becomes less influential on the yield value. It is thought that the molecular entanglement plays an important role at these rates of testing. However, substantial experimental work is required to substantiate their influence more quantitatively, which is outside the scope of the present investigation.

The effect of strain rate on E of PE80, PE100, BMPE and HDPE are shown in Figure 4.12. For all materials the data show well defined trends of increasing modulus with increasing strain rate. The most prominent feature is the steep decline in modulus data of HDPE at low strain rate. The branched polyethylene, on the other hand, showed a much more gradual decrease in modulus data over the strain rates considered. At high draw rate, it appears that the ability of HDPE to achieve large modulus values is through a combination of high density and a branch-free structure, both of which are

beneficial against tensile deformation. As the rate of extension is reduced, the benefits of high crystallinity on the strength of HDPE is negligible, as pointed out in an earlier discussion, whereas the smooth molecular chain may become detrimental to the disentanglement process. On the other hand, the degree of molecular entanglement in the branched polyethylene, achieved through the relative combination of molecular weight and side chain branching, could provide the stability in the modulus values as the strain rate is decreased.

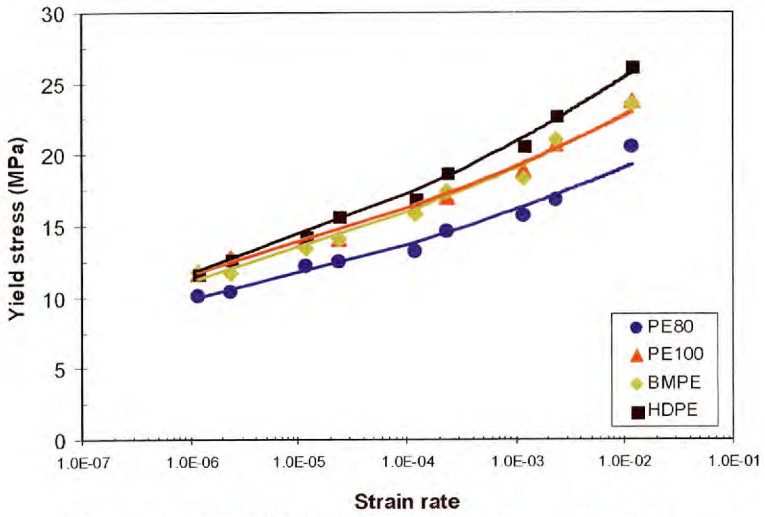

Figure 4.11 Yield stress as a function of strain rate.

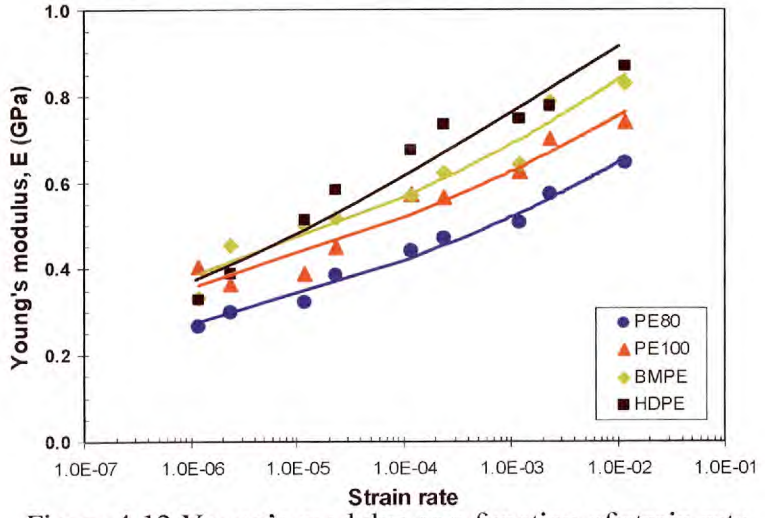

Figure 4.12 Young's modulus as a function of strain rate.

The strain rate $\dot{\varepsilon}$ dependence of σ_y and E can be expressed by a power law relation of the form shown in equations 4.3 and 4.4.

$$\sigma_y = \sigma_{y0} \dot{\varepsilon}^m \tag{4.3}$$

$$E = E_0 \dot{\varepsilon}^n \tag{4.4}$$

Where σ_{y0} and E_0 are the yield stress and modulus values at unit time respectively while the indices m and n are the power law index. The power law parameters listed in Table 4.1 are obtained from power law curves fitted to the data in Figures 4.11 and 4.12. The values of m and n are measured from the slopes of the respective curves and are an indication of the strain rate sensitivity of the respective properties.

PE types	σ_{y0} (MPa)	m	E_0 (GPa)	n
PE80	26.5	0.072	1.0	0.094
PE100	31.8	0.073	1.1	0.081
BMPE	35.6	0.078	1.2	0.085
HDPE	37.5	0.085	1.5	0.100

Table 4.1 Power law parameters.

As can be see from the Table 4.1, the values of m and n are the highest for HDPE, indicating that the rate at which σ_y and E fall are the greatest amongst the grades. This has been confirmed by the results in Figures 4.11 and 4.12. In conclusion, the strain rate dependence of σ_y and E of each grade can now be quantified in terms of the parameters defined in equations 4.3 and 4.4.

4.4 Conclusions

The results obtained from this study demonstrate that the tensile behaviour of polyethylene depends on the density (crystallinity), the degree of molecular entanglement and strain rate. It has been shown that the effect of strain rate affected the yield behaviour and the development of necking. The stress-strain behaviour changed markedly as the strain rate was decreased, changing from the initial necking and cold drawing behaviour to an almost homogeneous deformation with no necking. The strength and stiffness of the polyethylene improved with density (crystallinity) while

stretched at a high draw rate but the effect of crystallinity became less noticeable as the rate of extension is reduced. It is thought that the degree of molecular entanglement, which is a property of the molecular weight and branch content, plays a critical role in stabilising the stress-strain behaviour at these low rates of testing.

However, the role of post-yield behaviour (strain-hardening characteristics) has not been examined extensively here as it is outside the scope of the present work. Nevertheless, this area of research has proved invaluable in ascertaining if the macroscopic deformation behaviour at large strain is brittle or ductile (Haward [1994]) and Melick *et. al.*[2003]).

Chapter 5

The traction-separation behaviour of polyethylene

5.1 Introduction

It is well documented (Bhattacharya and Brown [1985], Lu *et. al.* [1991] and Brown and Lu [1995]) that the precursor to fracture in polyethylene is the failure of the craze structure ahead of the crack tip during slow crack growth. The formation of the craze and the mechanism that leads to craze breakdown have been described frequently. The craze nucleation is characterised by the formation of a highly localised zone ahead of the crack tip which consists of multiple voids. Their growth and subsequent coalescence leads to the formation of a fibrous structure. Depending on the stability of the craze structure, the craze may widen by drawing material from the craze-bulk interface into the craze fibrils and eventually rupture at the midribs, or fail at the craze-bulk interface with little or no signs of material fibrillation (Lagaron *et. al.* [2000]).

The deformation mechanism - craze nucleation and growth to eventual failure - in polyethylene has been extensively examined (Chan and Williams [1983], Donald [1997] and Beech *et. al.* [2001]). It is clear from these studies that crazing plays a crucial role in governing the fracture process. Therefore, a good comprehension of the craze structure is required to understand the fracture modes observed in polyethylene. This led to the development of a circumferentially notched tensile specimen by Duan and Williams [1998]. The specimen is a deep notched square section specimen of dimension 16 x 16 x 120 mm with a circular ligament. The depth of the notch is determined by calculating the ligament to bulk area (LBA) ratio at 10%. The deep symmetrical notch developed a highly constrained region in the ligament. As a result of the geometrical discontinuity, the plane strain conditions prevailed in the ligament thus suppressing the plane stress yielding and encouraged the cavitation process (associated with crazing) across the confined ligament while stretched under tension. The results for

a range of polyethylene were given in stress-time plots to describe the fracture behaviour.

Pandya and Williams [2000a,b] extended the work of Duan and Williams [1998], in which they postulated a traction-separation relation to explain the behaviour of the crack tip damage (craze) zone. They demonstrated that the physical mechanisms in the zone were quantifiable by rate-dependent traction-separation curves and a series of cohesive laws describing the behaviour was established. More importantly, the study provided a clearer presentation of the failure mechanisms that leads to crack growth. However, the study suffered from the restriction that the tests were mostly carried out on fixed notch depth specimens and thus fixed constraint. In reality, the time-dependent behaviour of the craze is likely to be affected by the notch geometry. Therefore, the subsequent crack advance would be influenced by the degree (size) of the localised plastic deformation at the crack tip (Kinloch and Williams [1980]).

Recently, Ivankovic *et. al.* [2003] attempted to provide a predictive assessment of the crack growth behaviour and discovered that crack initiation and propagation were indeed subject to and dependent on the constraint effects, in addition to rate. Thus, it would appear that the ductile crack growth mechanism in tough polyethylene was not well understood. Indeed, an accurate assessment of the craze behaviour at various rates and constraint levels is required to elucidate the damage and deformation mechanisms in polyethylene. Although some work has been performed to investigate the effect of loading rate on the deformation and failure mechanisms (Pandya *et. al.* [2003b]), the role of the crack-tip constraint on the fracture behaviour has yet to be examined extensively.

The present experiments were designed to measure *in-situ* the development of the damage mechanisms (craze) under different constraint conditions over a wide range of loading speeds. Here, the localised fracture process is represented in terms of a traction-separation relation on the plane of fracture. The aim is to show that the formation and subsequent failure of the damage zone was dependent on the constraint level, in addition to the applied rate. Through the microscopy work, a unified approach was developed which combines mechanical characteristics with microstructural observations to ascertain these mechanisms.

5.2 Results and discussion – Direct measurements of the cohesive law

The geometry of the circumferentially notched tensile specimen and the experimental methods were explained in section 3.2.2 and 3.3.2 respectively. The specimens were subjected to uniaxial tension at fixed crosshead speeds of between 0.005 and 50 mm/min. Two different procedures were used to vary the level of constraint in the ligament. In the first, the specimen thickness is kept fixed while the notch depth, i.e. the ligament to bulk area (LBA) ratio, is varied as illustrated in Figure 5.1(a). In the second procedure, the LBA ratio was fixed and the specimen thickness varied (Figure 5.1 (b)). The various dimensions are listed in Table 3.2.

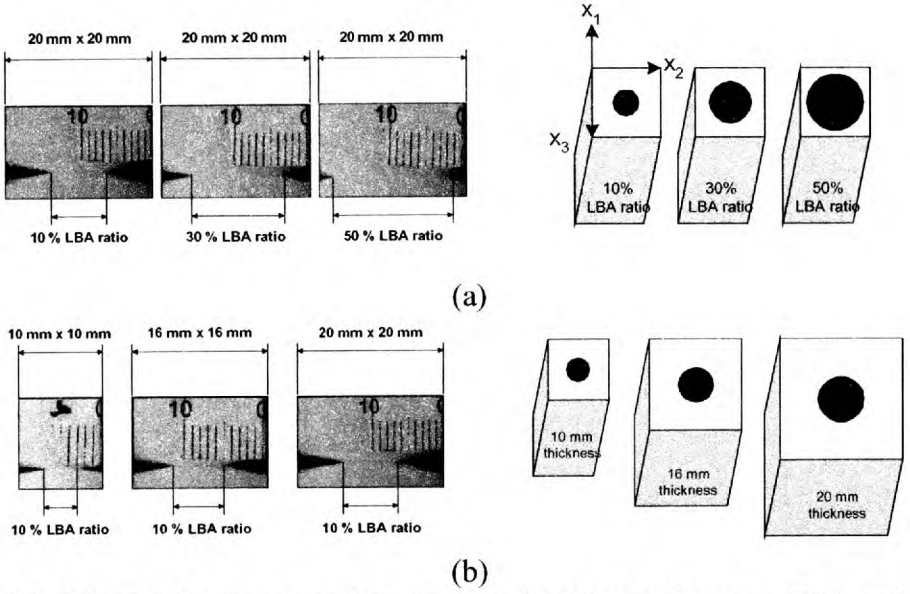

Figure 5.1 The crack tip constraint changed by (a) varying the LBA ratio and (b) changing the specimen thickness.

5.3 The effect of notch depth

5.3.1 The effect of notch depth in PE80

Figure 5.2(a) shows the effect of notch depth on the traction-separation behaviour of PE80 at a fixed crosshead speed of 0.005 mm/min. The associated damage evolutions observed from the CNT samples are shown in Figure 5.2(b) whereas Figure 5.2(c) shows micrographs of the crack tip damage zone examined at the pre-peak, peak and post-peak stages of loading. The method used for sectioning the specimen was

described in § 3.3.3. According to Figure 5.2(a), the initial stiffness and the peak stress of the cohesive curve reduce whereas the separation distance shows a marked increase at increasing LBA ratio. This is a feature common to all the grades.

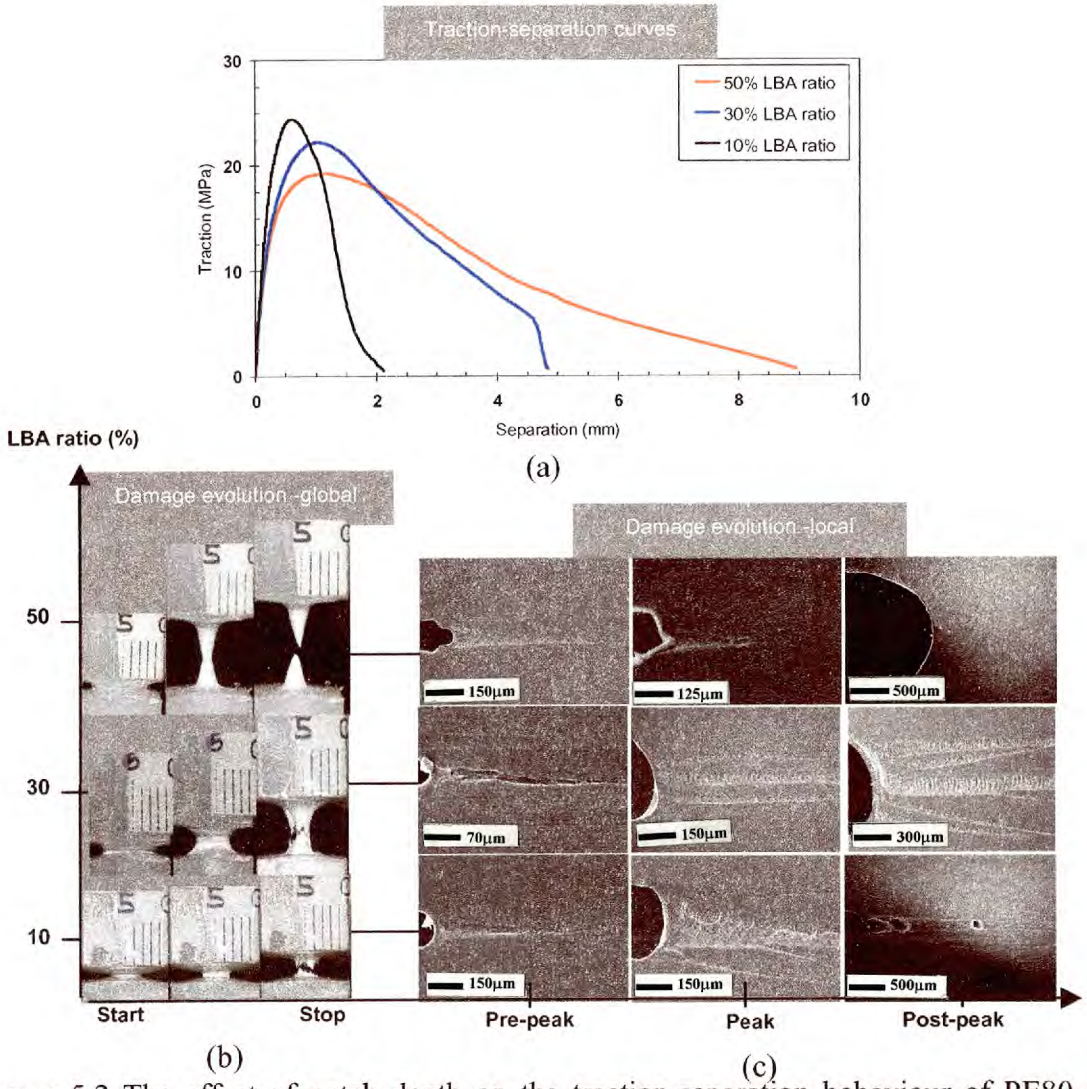

Figure 5.2 The effect of notch depth on the traction-separation behaviour of PE80 at 0.005mm/min. The specimen thickness is 10mm. (a) The measured traction-separation curves. (b) Photographs showing the sequence of fracture during testing. (c) SEM micrographs of sectioned specimen examined at different stages of loading.

As can be seen from Figure 5.2(b), the differences in separation distance and hence separation energy (area under the curve) can be attributed to the different damage mechanisms as the LBA ratio (constraint) varies. It can be seen that at 10% LBA ratio, the limited deformation of the craze fibrils resulted in a small post peak extension. Likewise at 30% LBA ratio, the failure mechanism was similar except that more material has been drawn into the craze. In contrast, at 50% LBA ratio, there was

continuous drawing of material into the damage region until failure occurred. Examination of the cross-sectioned specimen under the SEM at various stages of loading, as shown in Figure 5.2(c), gives a clear depiction of the craze evolution. For all the LBA ratios, damage was initiated in the craze prior to reaching the peak load. By the time the peak load was attained, the 10% LBA ratio specimen showed the onset of multiple crazing. Likewise, a multiple craze structure was observed in the 30% LBA ratio specimen. However, the size of the secondary crazes found in the 30% LBA ratio is comparably larger than those seen in 10% LBA ratio specimen. As a result, the degree of tip blunting is significantly higher than that of the 10% LBA ratio specimen. On the other hand, a single craze structure was formed at the notch tip of the 50% LBA ratio specimen but the notch tip was comparably more blunted due to a significant bulk drawing. At this stage of loading (peak), the craze zones at each notch have not extended across the ligament. At a later stage of loading (post-peak), multiple crazing continues to be the principal damage mechanism for both of the 10% and 30% LBA ratio specimens. According to the micrograph of the 10% LBA ratio specimen, the primary craze has extended across the ligament accompanied by the void growth while most of the secondary crazes formed remained unconnected. By comparison, the majority of the crazes in the 30% LBA ratio specimen have grown across the ligament. It becomes apparent that the small post-peak extension seen in Figure 5.2(a) for the 10% LBA ratio curve is due to the failure of the primary craze only. As the LBA ratio increased to 30%, the damage was characterised by the simultaneous growth of the multiple crazes. Consequently, the 30% LBA ratio specimens were capable of drawing more material into the numerous craze zones leading to a greater post-peak extensibility on the macroscopic scale (Figure 5.2(a)). Towards the end, the descending slope of the traction curve becomes steeper owing to the failure of the craze. On the contrary, the damage mechanism of the 50% LBA ratio specimen transformed from crazing to shearing. As a consequence, the specimen appears to behave like a tensile specimen deformed under plane stress conditions as it undergoes shear without the formation of appreciable voids. Again, the transformation in the mechanism is indicated by the change in the slope of the post-peak response of the 50% LBA ratio curve as shown in Figure 5.2(a).

Figure 5.3 compares the traction-separation properties at 0.5mm/min. As before, the peak stress falls with increasing LBA ratio whereas the separation distance and the energy value increase with increasing LBA ratio. However, the increase in the separation distance is lower than those measured at 0.005mm/min due to the difference in the fracture behaviour.

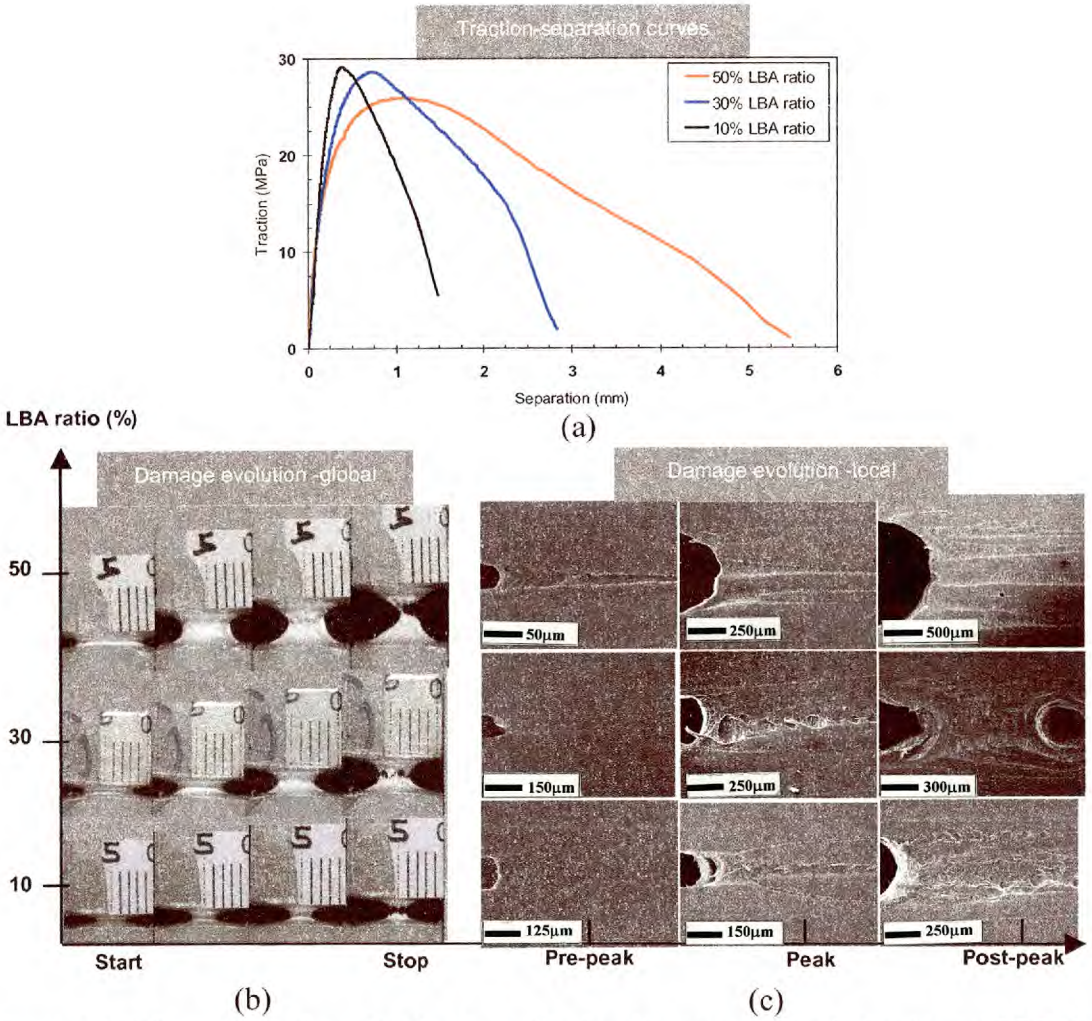

Figure 5.3 The effect of notch depth on the traction-separation behaviour of PE80 at 0.5mm/min. The specimen thickness is 10mm. (a) The measured traction-separation curves. (b) Photographs showing the sequence of fracture during testing. (c) SEM micrographs of sectioned specimen examined at different stages of loading.

Once again, the constraint for the 10% LBA ratio curve is the highest while it is the lowest in the 50% LBA ratio curve. On the whole, the notch tip material flows more readily to blunt the tip as the crack tip constraint is relieved (i.e. increasing the LBA ratio). As shown in Figure 5.3(b), the 50% LBA ratio draws in more material into the damaged ligament and consequently the tip is more blunted. It is this mechanism (crack

blunting arising as a result of plastic flow) which delays the crack initiation and may be inferred from the cohesive curve from the lack of a change in slope after the peak stress. At the peak stress, the micrographs in Figure 5.3(c) reveals that at 50% LBA ratio, the dominant craze is absent from the damage structure. Instead, the structure consisted of crazes of approximately equal thickness. Such a structure appears to blunt the tip more effectively as illustrated in Figure 5.4. As can be seen from the figure, the secondary crazes appear to grow independently from the primary craze at the tip. As a result, the secondary crazes itself contributed to the blunting process. By comparison, the amount of blunting that depends solely on the primary crazes is much lower. Clearly, the high degree of crack tip blunting in the 50% LBA ratio sample has increased the total energy of separation through a large separation distance even though the peak stress was lower than that of the 10% or 30% LBA ratio samples (Figure 5.3(a)). It should be noted that the length of the damage zone has not yet reach the full ligament length.

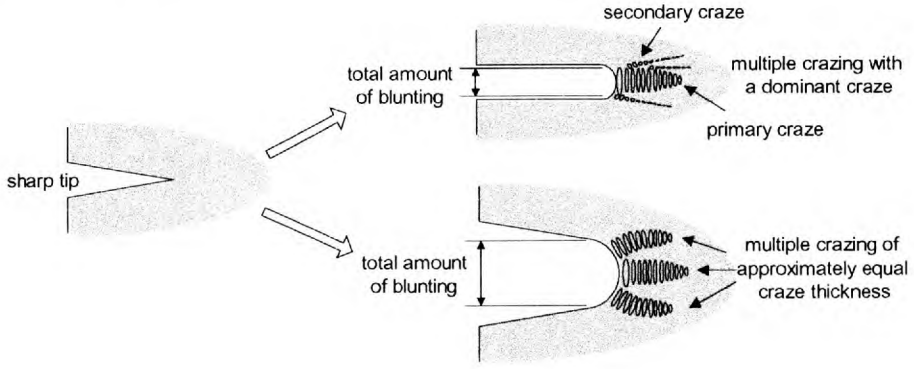

Figure 5.4 A schematic illustration of the degree of notch tip blunting.

Figure 5.5 shows the constraint dependence on the traction behaviour of each LBA ratio sample at 50 mm/min, along with the associated damage evolution. The peak stress in Figure 5.5(a) falls with increasing LBA ratio as expected. The most significant feature seen here is the smaller difference in break separation values between the samples. Apparently at this speed, the blunting process seems to be suppressed as seen in Figure 5.5(b). As the samples were pulled apart, the fractured surface revealed a level/flat texture. At this condition, the damage has spread across the ligament by the time the stress reaches the peak as seen in Figure 5.5(c).

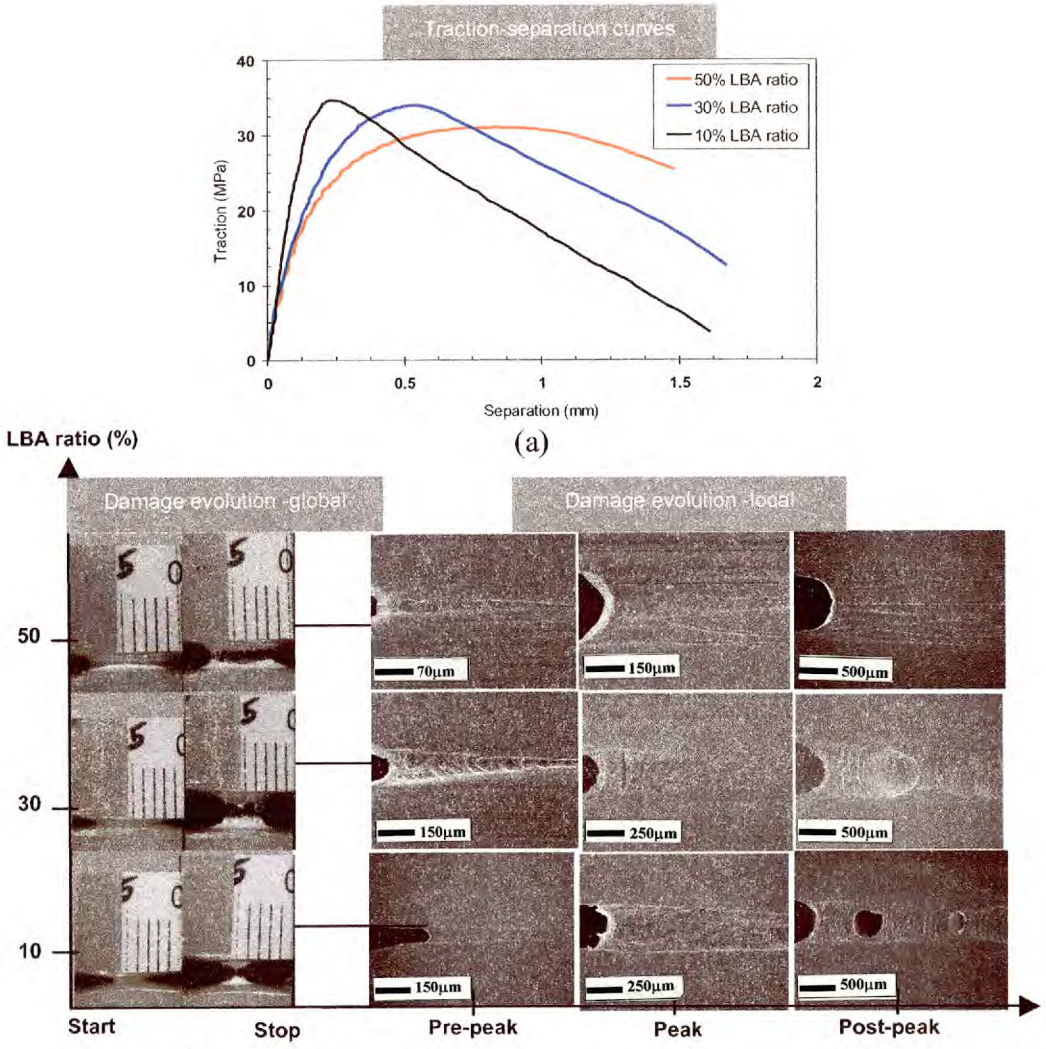

Figure 5.5 The effect of notch depth on the traction-separation behaviour of PE80 at 50mm/min. The specimen thickness is 10mm. (a) The measured traction-separation curves. (b) Photographs showing the sequence of fracture during testing. (c) SEM micrographs of sectioned specimen examined at different stages of loading.

According to the micrographs, a homogenous craze structure is formed in the 10% and 30% LBA ratio whereas the damaged ligament of the 50% LBA ratio showed a multiple craze structure. This is in contrast to the observation at low and intermediate test speeds in which both of the 10% and 30% LBA ratio showed the formation of the multiple craze structure. As the damage zone thickens (post-peak stage), the fibrillar structure in the 10% and 30% LBA ratio samples became highly drawn in the direction of the applied tensile stress. Subsequently, the fracture energy consumed was associated with void coalescence during the growth. As a result, the fracture surface consists of large voids as seen in Figure 5.6. By comparison, the brittle response of the 50% LBA

ratio (Figure 5.5(a)) resulted in a fracture surface that contains islands or patches of craze remnant attached to one half of the surfaces which mate with detachment zones on the mating surface as shown in Figure 5.7(a). It is likely that the crack grows alternatively from one craze-matrix boundary interface and then the other, resulting in a "layered structure" surface as described previously by Hazra [2000] and illustrated in Figure 5.7(b). Under the conditions of increasing extension rates, the features of the single craze structure appears more desirable as opposed to a multiple craze structure which could leads to a more brittle behaviour.

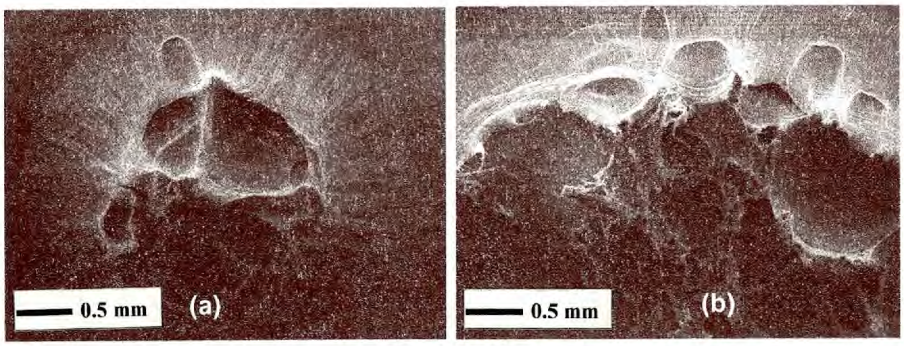

Figure 5.6 Fracture surfaces of the (a) 10% and (b) 30% LBA ratio specimens viewed under SEM.

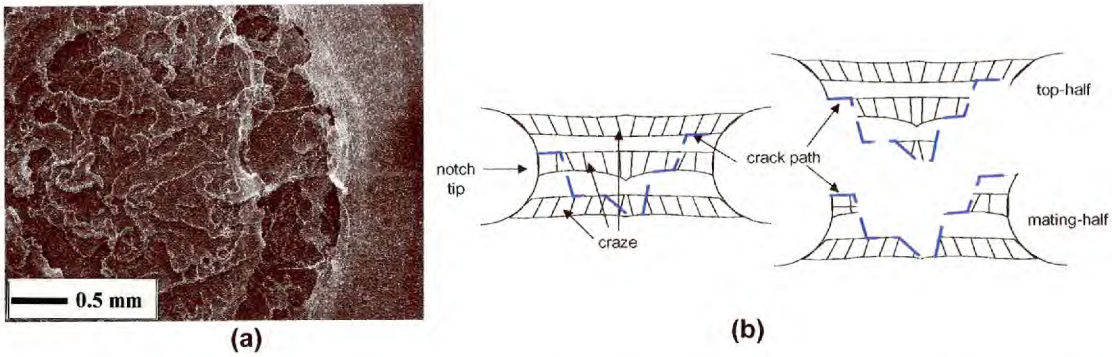

Figure 5.7 (a) Fracture surface of the 50% LBA ratio specimen viewed under SEM. (b) A schematic illustration of the layered structure appearance.

5.3.2 The effect of notch depth in PE100

Figure 5.8(a) shows the effect of notch depth on the traction-separation properties of PE100 measured at a constant crosshead speed of 0.005mm/min. Figure 5.8(b) shows the sequence of fracture while Figure 5.8(c) compares the damage zone of each notch at

various stages of loading. As can be seen in the Figure 5.8(a), the behaviour of each curve is unique. This is seen by the variation in stiffness (initial slope) with notch depth which increases with decreasing LBA ratio. Also, the 10% LBA ratio curve has the highest peak stress which falls with increasing LBA ratio. However, the energy value of the 50% LBA ratio curve is the highest despite its lowest peak stress. The reason for higher energy values was a significant increase in the break separation. It can be seen in the Figure 5.8(b) that the greater degree of crack tip ductility in the 50% LBA ratio leads to a ductile deformation.

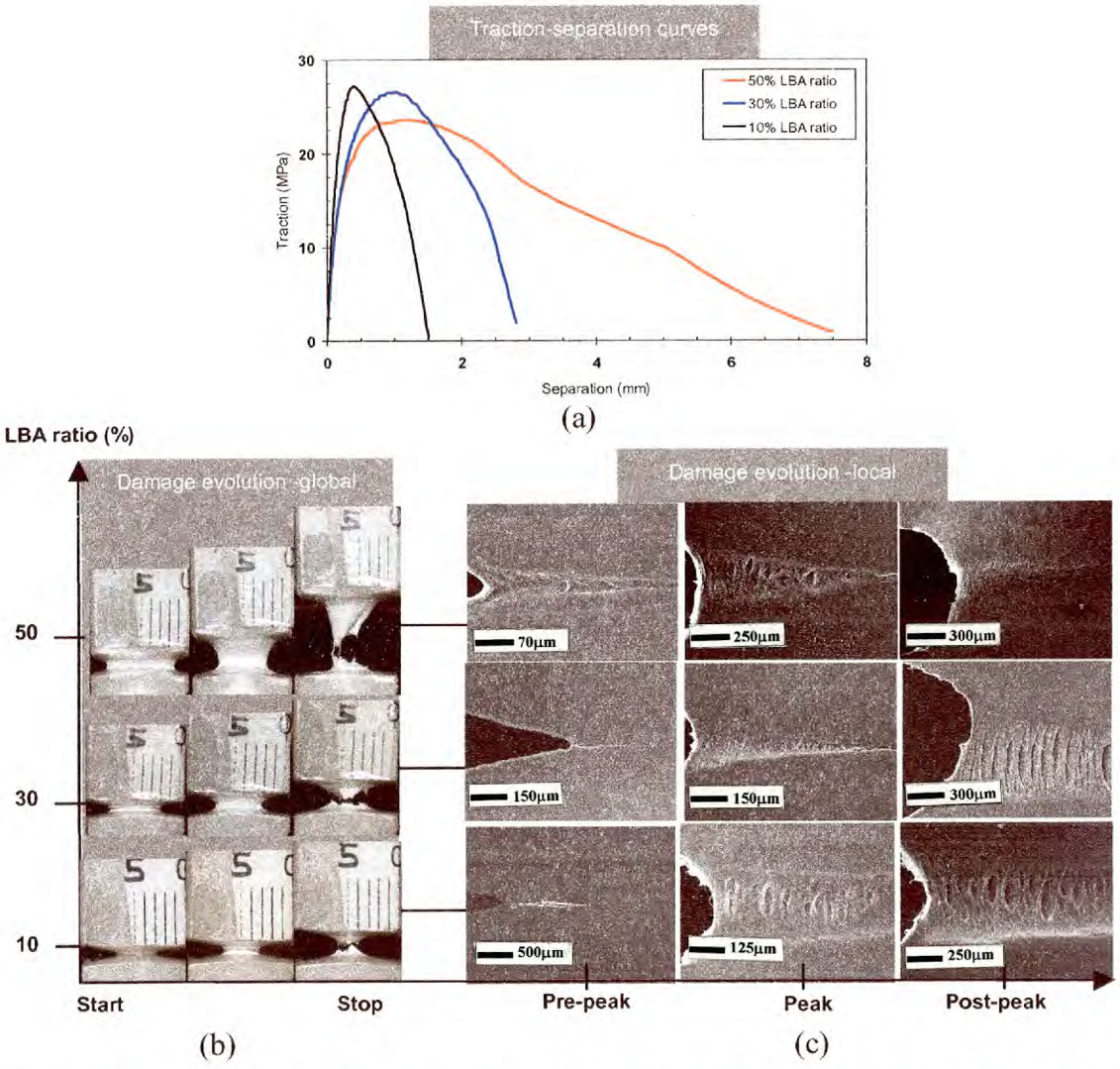

Figure 5.8 The effect of notch depth on the traction-separation behaviour of PE100 at 0.005mm/min. The specimen thickness is 10mm. (a) The measured traction-separation curves. (b) Photographs showing the sequence of fracture during testing. (c) SEM micrographs of sectioned specimen examined at different stages of loading.

Figure 5.9 shows that the initial craze in the 10% and 30% LBA ratio samples (Figure 5.8(c)) has grown radially inwards to meet in the centre of the ligament during the post-peak stages of loading. The similarity in appearance between the damaged ligament of the 10% and 30% LBA ratio is truly striking. This is also manifested in the form of a similarly shaped traction curve between the specimens (Figure 5.8(a)).

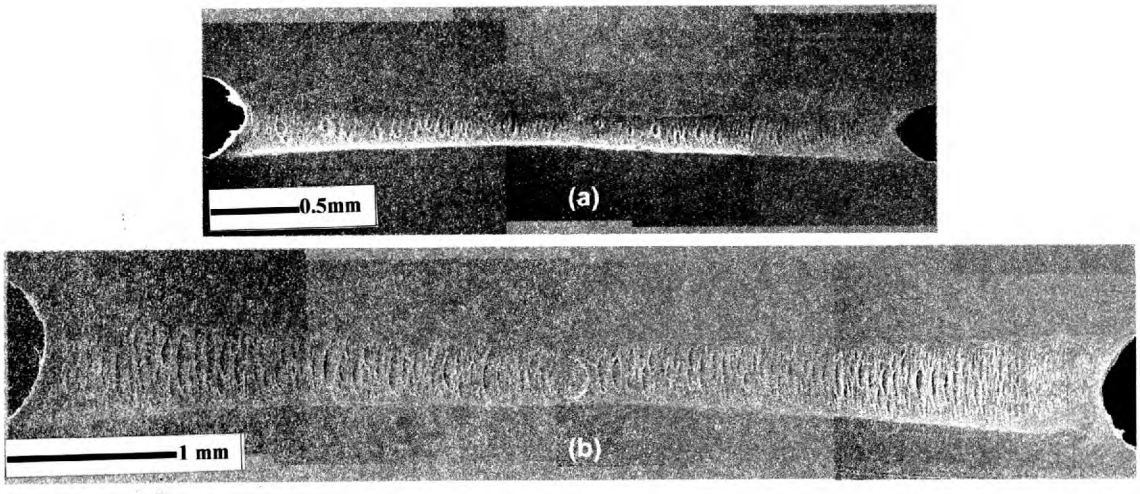

Figure 5.9 The damaged ligament of the (a) 10% and (b) 30% LBA ratio specimens during the post-peak stages of loading.

Micrographs of the 50% LBA ratio specimen, on the other hand, shows that the initial craze formed appears to be embedded in the shear bands. The fractured surface in Figure 5.10(a) seems to suggest that the modes of fracture near the surface is due to shear yielding while craze yielding prevails on the interior. This is in contrast to the homogenous ductile necking associated with the PE80 tested at the same test condition (Figure 5.10(b)).

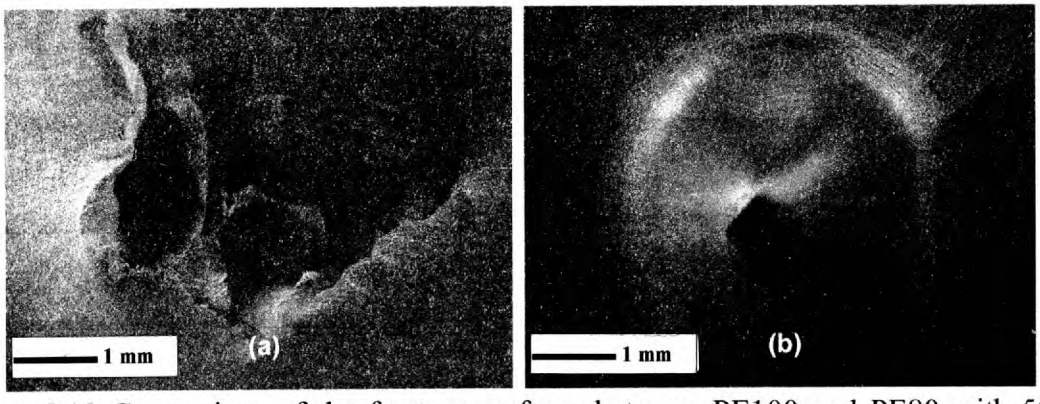

Figure 5.10 Comparison of the fracture surfaces between PE100 and PE80 with 50% LBA ratio at 0.005mm/min.

Figure 5.11 shows the results of the traction-separation measurement performed at 0.5mm/min. At this speed, there was a marked drop in the separation distance of the 50% LBA ratio sample. According to the Figure 5.11(b), the cause of the reduction in the break separation is an increase in the plastic flow constraint which is comparably higher than at the speed of 0.005mm/min. Nevertheless, the separation distance of the 50% LBA ratio is still larger than that of the 10% or 30% LBA ratio curves in Figure 5.11(a), indicating that the plastic flow constraint is lower in the former.

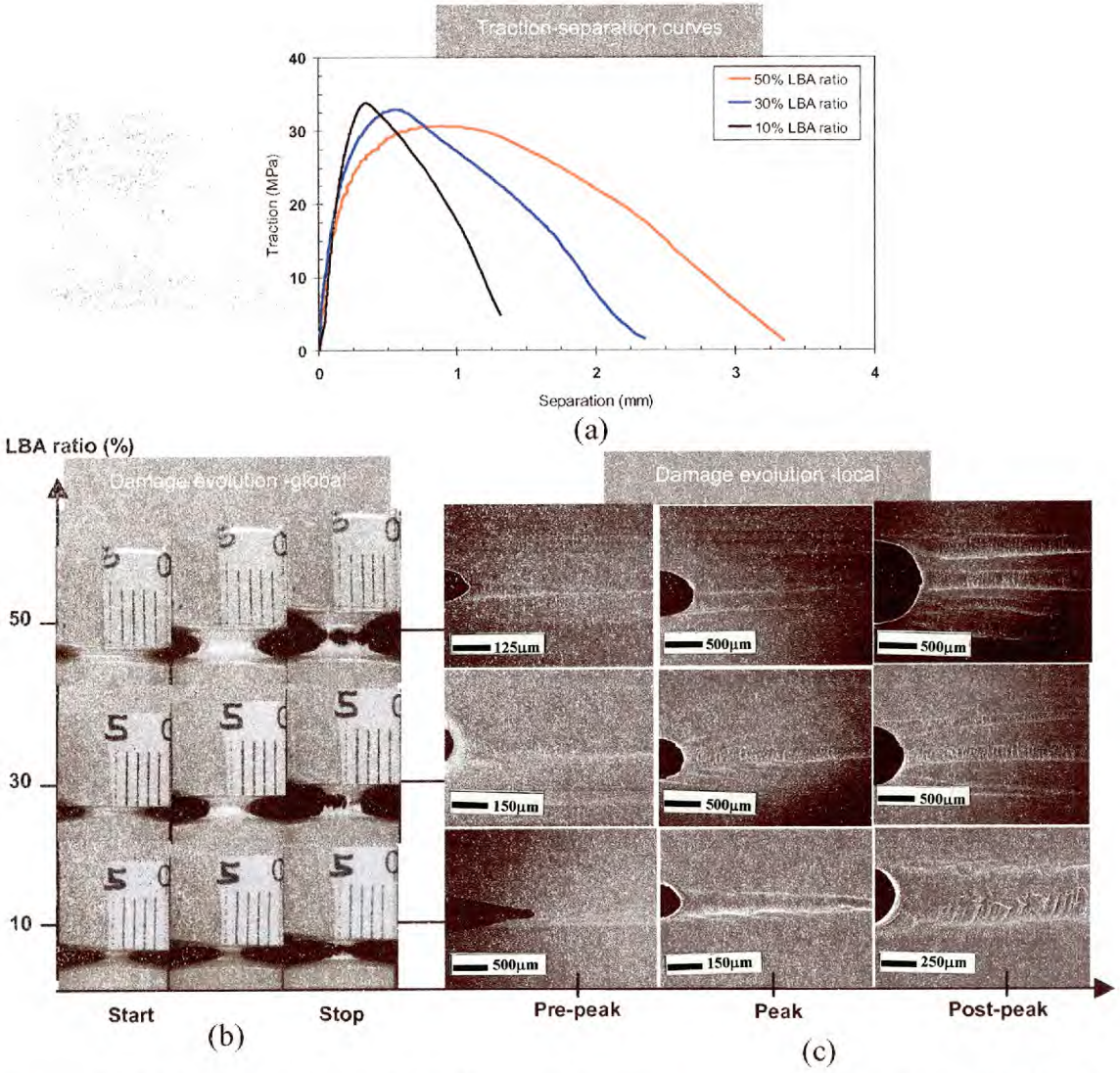

Figure 5.11 The effect of notch depth on the traction-separation behaviour of PE100 at 0.5mm/min. The specimen thickness is 10mm. (a) The measured traction-separation curves. (b) Photographs showing the sequence of fracture during testing. (c) SEM micrographs of sectioned specimen examined at different stages of loading.

The damage zone of each notch at the peak in Figure 5.11(c) shows a multiple craze structure. At this stage, the length of the damage zone is less than the ligament length. Beyond the peak, the dominant craze in the 10% LBA sample ratio seems to have impeded the growth of the secondary crazes. By comparison, the secondary crazes in the 30% and 50% LBA ratio have grown to a thickness that is roughly equal to the main craze. For this reason, both of the 30% and 50% LBA ratio samples are capable of a large post-peak extension. Eventually, the failure occurs predominantly along the primary craze after the fibrils have probably reached the critical drawn ratio.

The traction-separation properties measured at 50mm/min are shown in Figure 5.12. The trend of falling peak stress with increasing LBA ratio is similar to that seen at low and intermediate rates. In moving towards higher test rates, the crack tip ductility is almost suppressed as seen in Figure 5.12(b), resulting in substantial falls in the break separation values (Figure 5.12(a)). The fall in the break separation values is more significant in specimens with a higher LBA ratio. Consequently, the difference in the separation distance is small between the curves (Figure 5.12(a)). Another notable feature is the shape of each curve is quite similar. Also, the near similarity in the traction behaviour between the specimens could be accounted for the closeness in the energy values. Apparently, the difference in the behaviour (fracture energy) could no longer be differentiated solely on the basis of the constraint effects. It would appear that the effect of rate plays a more central role on the fracture properties at high rates of testing.

At the speed of 50mm/min, the peak stress in Figure 5.12(a) denotes the formation of the craze across the full ligament length. Subsequent loading beyond the peak generates voids as seen in the micrographs in Figure 5.12(c). Given that the traction curves in Figure 5.12(a) exhibited stable post-peak behaviour, the coalescence is likely to occur through the elongation of the voids and the elongation of the bridges of material between the voids. Remarkably, the fracture behaviour of the PE100 at this condition is more or less the same as with the PE80 (Figure 5.5).

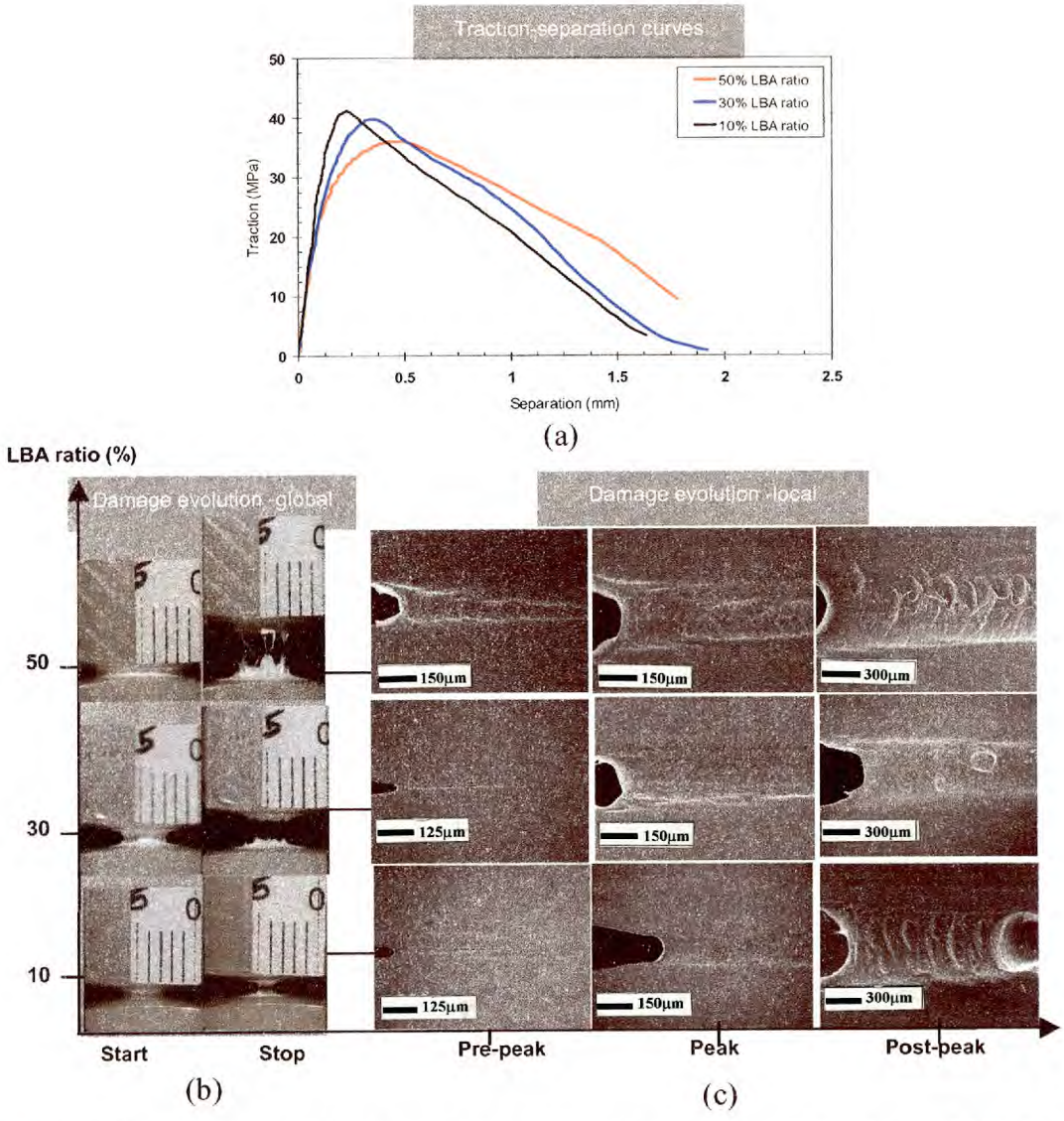

Figure 5.12 The effect of notch depth on the traction-separation behaviour of PE100 at 50mm/min. The specimen thickness is 10mm. (a) The measured traction-separation curves. (b) Photographs showing the sequence of fracture during testing. (c) SEM micrographs of sectioned specimen examined at different stages of loading.

5.3.3 The effect of notch depth in BMPE

Figure 5.13(a) shows the effect of notch depth on the traction-separation properties of BMPE measured at a fixed crosshead speed of 0.005mm/min. Figure 5.13(b) shows the sequence of fracture whereas 5.13(c) compares the damage zone of each notch at various stages of loading.

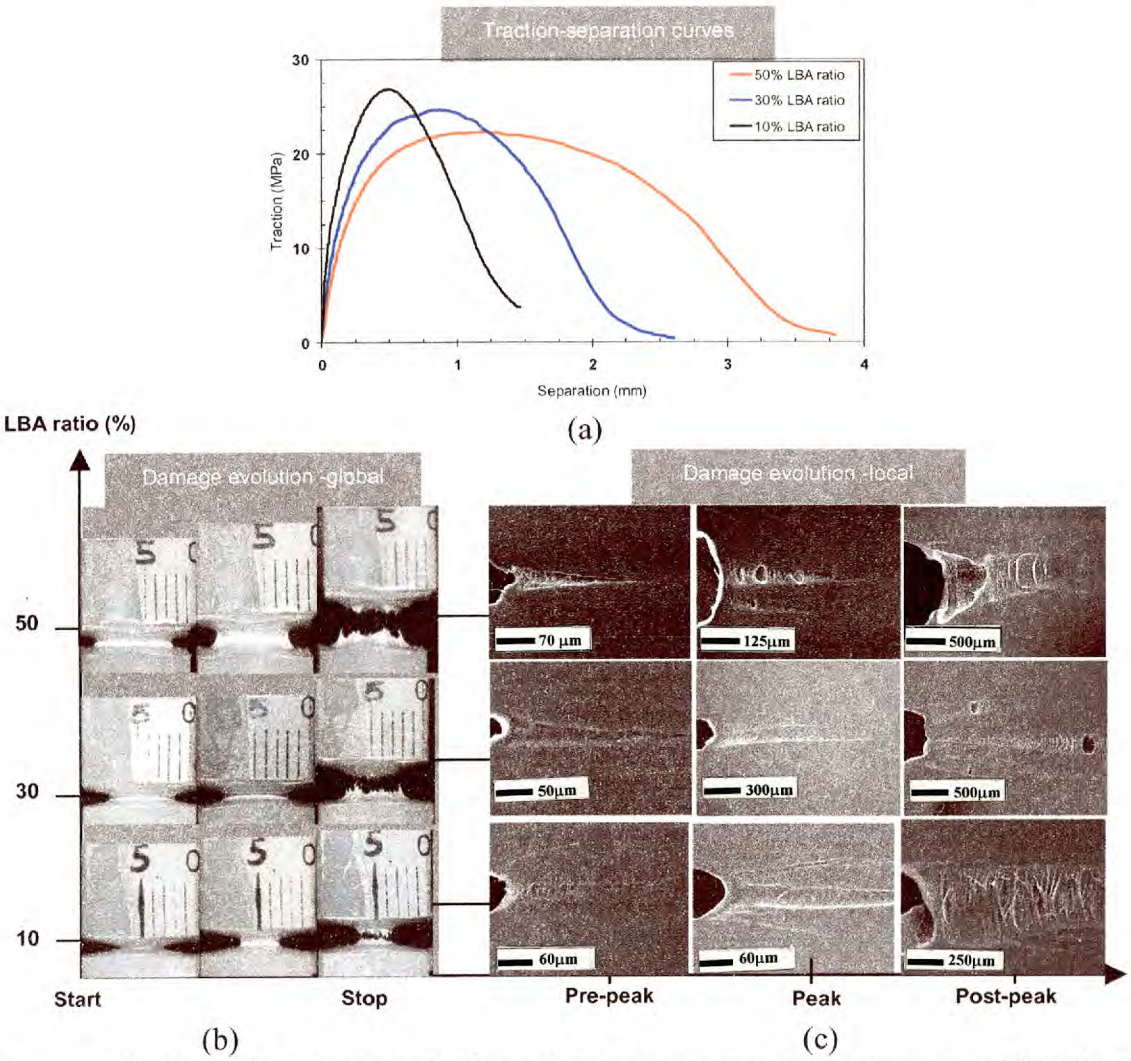

Figure 5.13 The effect of notch depth on the traction-separation behaviour of BMPE at 0.005mm/min. The specimen thickness is 10mm. (a) The measured traction-separation curves. (b) Photographs showing the sequence of fracture during testing. (c) SEM micrographs of sectioned specimen examined at different stages of loading.

The peak stress in Figure 5.13(a) falls with increasing LBA ratio. The energy of separation of the 10% LBA ratio is almost one-third that of the 50% LBA ratio whereas the 30% LBA ratio sample is almost half, indicating a constraint dependent behaviour at this speed. As there is insufficient notch tip constraint in the 50% LBA ratio sample, the material deforms by a shear yielding process as seen in the Figure 5.13(b). Because of this, the 50% LBA ratio has a larger post-peak extension than those of the 10% or 30% LBA ratio samples. It can be seen from the micrographs in Figure 5.13(c) that the damage is initiated with the nucleation of the craze at each notch while the tip behaviour at the peak showed the formation of the multiple craze structure At this stage, the dominant craze has spanned the ligament of the 10% LBA ratio specimen unlike for the

30% and 50% LBA ratio specimens. The multiple craze structure of the 10% LBA ratio detected during the peak appears to merge into a single craze structure at the post peak stage. There is also evidence of void growth as seen in Figure 5.14.

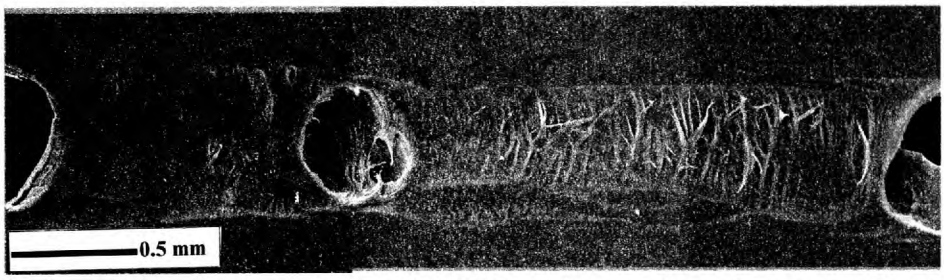

Figure 5.14 The damage structure in the 10% LBA ratio sample at the post-peak stage.

Beyond the peak, the multiple craze mechanisms continue to blunt the tips of the 30% LBA ratio. However, the secondary crazes which have initiated at each notch tip remain unconnected while the primary craze has grows across the ligament as seen in Figure 5.15. Ultimately, the cracks would probably propagate through the primary craze due to a higher number of voids initiated. Returning to Figure 5.13(c), the micrograph of the 50% LBA ratio shows a highly stretched notch tip structure during the post-peak stage. The fracture eventually occurred via the shear neck down of the outer rim of the ligament while the interior deformed through a process of voids coalescence. This gives rise to the characteristics "double cup" appearance associated with the ductile tensile fracture.

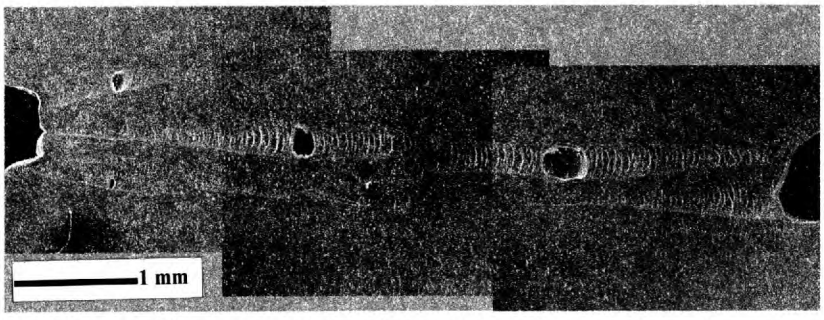

Figure 5.15 The damaged ligament of the 30% LBA ratio sample at the post-peak stage.

Figure 5.16 shows the constraint dependence of the traction behaviour of each LBA ratio measured at 0.5mm/min. As shown in Figure 5.16(a), the peak stress increases as the LBA ratio is lowered. On the other hand, the peak region becomes broader with an increase in the LBA ratio. Both of the 10% and 30% LBA ratio curves showed stable post-peak behaviour where the slope of the curve beyond the peak remained unchanged.

In contrast, the 50% ratio curve failed suddenly. According to the micrographs in Figure 5.16(c), the notch tip structure of the 50% LBA ratio is breached during the post-peak stage. A closer look at the damaged ligament in Figure 5.17 reveals a non-uniform thickening of the damage zone along the ligament length. Obviously, there is a sharp gradient of strain from the notch to the craze tip. The strain distribution being the greatest at the notch tip while the interior (craze tip) experiences the lowest strain. Consequently, the uneven thickening of the damage zone in the axial direction caused the notch tip material to be breached first thereby paving the way for the radial crack growth.

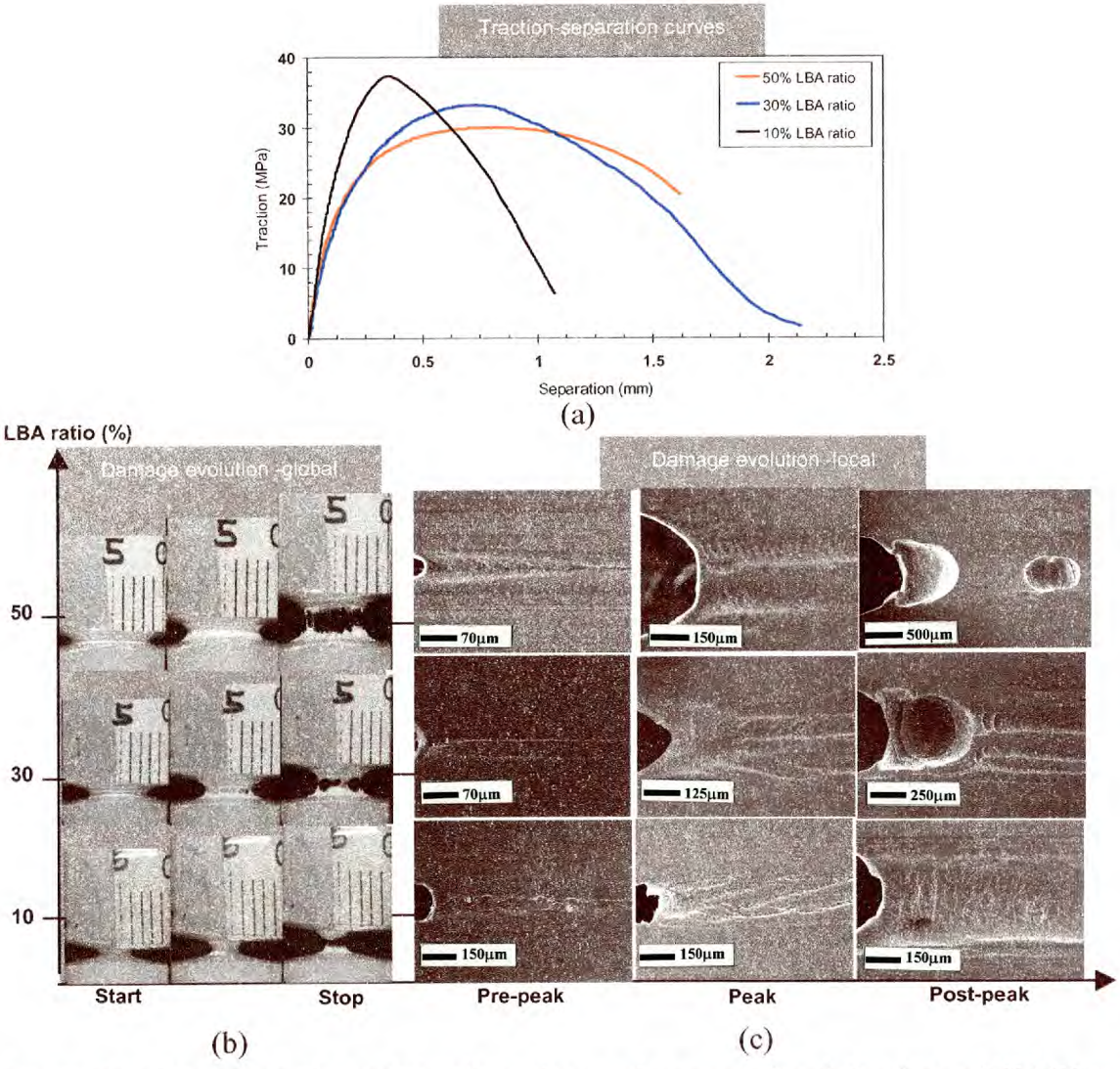

Figure 5.16 The effect of notch depth on the traction-separation behaviour of BMPE at 0.5mm/min. The specimen thickness is 10mm. (a) The measured traction-separation curves. (b) Photographs showing the sequence of fracture during testing. (c) SEM micrographs of sectioned specimen examined at different stages of loading.

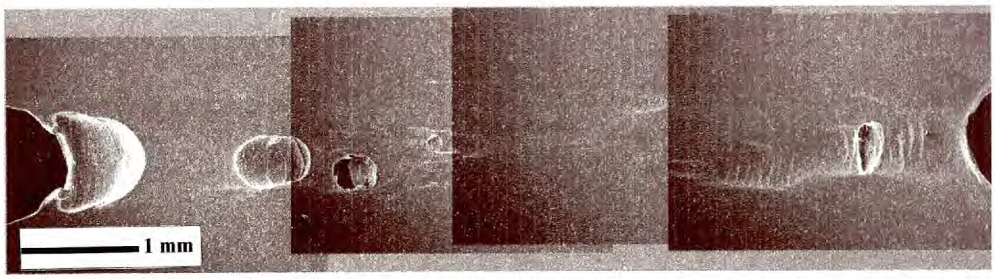

Figure 5.17 The damage structure of the 50% LBA ratio sample at the post-peak stages.

Figure 5.18 compares the traction-separation properties at 50mm/min.

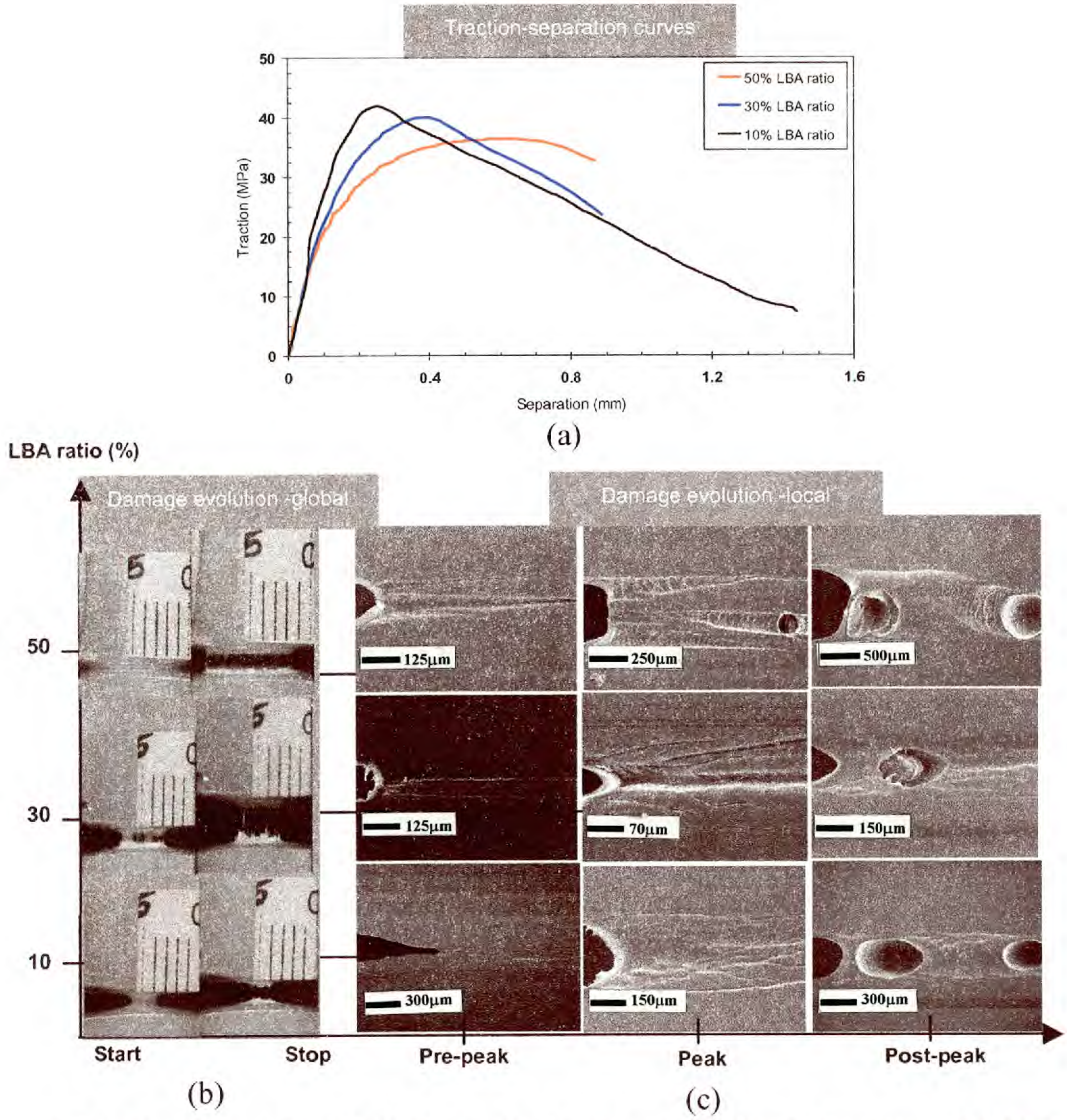

Figure 5.18 The effect of notch depth on the traction-separation behaviour of BMPE at 50mm/min. The specimen thickness is 10mm. (a) The measured traction-separation curves. (b) Photographs showing the sequence of fracture during testing. (c) SEM micrographs of sectioned specimen examined at different stages of loading.

The trend of failing peak stress with increasing LBA ratio is similar to the results measured at lower speeds. An increase in the test speed causes both of the 30% and 50% LBA ratio specimens to fail unexpectedly as reflected by the traction curves in Figure 5.18(a). Furthermore, the higher applied rate facilitated the growth of the damage to the ligament length by the time the peak load is reached. At this stage, all specimens show the formation of the multiple craze structure (Figure 5.18(b)). Another effect of high test speed appears to encourage the void initiation and the growth by multiple void interaction. As shown in Figure 5.18(c), an extension beyond the peak leads to voiding whilst the multiple crazes merged into a single craze. The higher rate of void growth in the 30% and 50% LBA ratio samples is likely to account for the post-peak instability. Figure 5.19 shows that the voiding becomes widespread immediately after the peak in the 50% LBA ratio sample.

Figure 5.19 The damaged ligament of the 50% LBA ratio sample prior to fracture tested at 50mm/min.

5.3.4 The effect of notch depth in HDPE

Figure 5.20 shows the traction-separation behaviour and the corresponding damage evolution of HDPE measured at 0.005 mm/min. As shown in Figure 5.20(a), both the initial stiffness and peak stress of the traction curves decrease while the separation distance increases with increasing LBA ratio. At 10% LBA ratio, the craze formed failed suddenly as seen in the Figure 5.20(b). Increasing the LBA ratio encourages a craze-crack growth behaviour to emerge, resulting in a localised fibrillation process at the ligament centre. The fibrillation process becomes more pronounced at 50% LBA ratio thereby increasing the separation distance and hence the energy to break (Figure 5.20(a)).

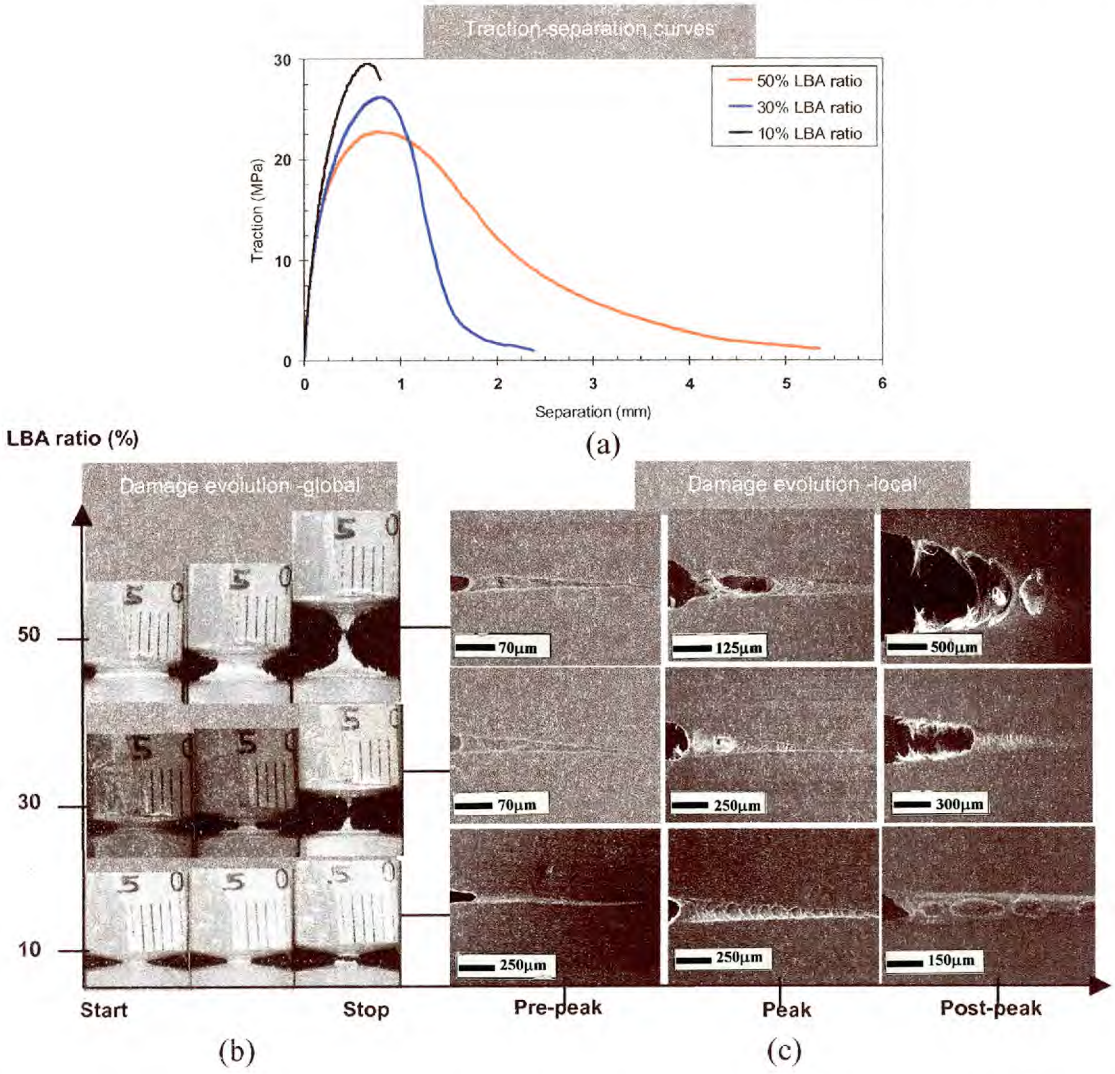

Figure 5.20 The effect of notch depth on the traction-separation behaviour of HDPE at 0.005mm/min. The specimen thickness is 10mm. (a) The measured traction-separation curves. (b) Photographs showing the sequence of fracture during testing. (c) SEM micrographs of sectioned specimen examined at different stages of loading.

It can be seen from the SEM micrographs in Figure 5.20(c) that the damage is initiated with the nucleation of the craze at each notch. At the peak load, the damage has spanned the ligament of the 10% LBA ratio specimen whereas the deformation is still localised at the notch tip of the 30% and 50% LBA ratio specimens. However, the craze length was longer in the 30% LBA ratio specimen but a larger fibril extension was observed in the 50% LBA ratio specimen. Further loading caused the fibril to fracture earliest within the craze region (inside the ligament) of the 10% LBA ratio specimen. On the other hand, the tip material of the 30% and 50% LBA ratio specimens was breached, resulting in an inward crack growth. The descending slope of the traction

curves showed a steep decline immediately after the peak confirmed the occurrence of the crack growth (Figure 5.20(a)). The change in slope towards the end indicated the fibrillation process as described earlier. Unlike the copolymers, the HDPE shows little signs of the blunting process even with an increase in the LBA ratio.

Figure 5.21 compares the traction-separation properties at 0.5mm/min.

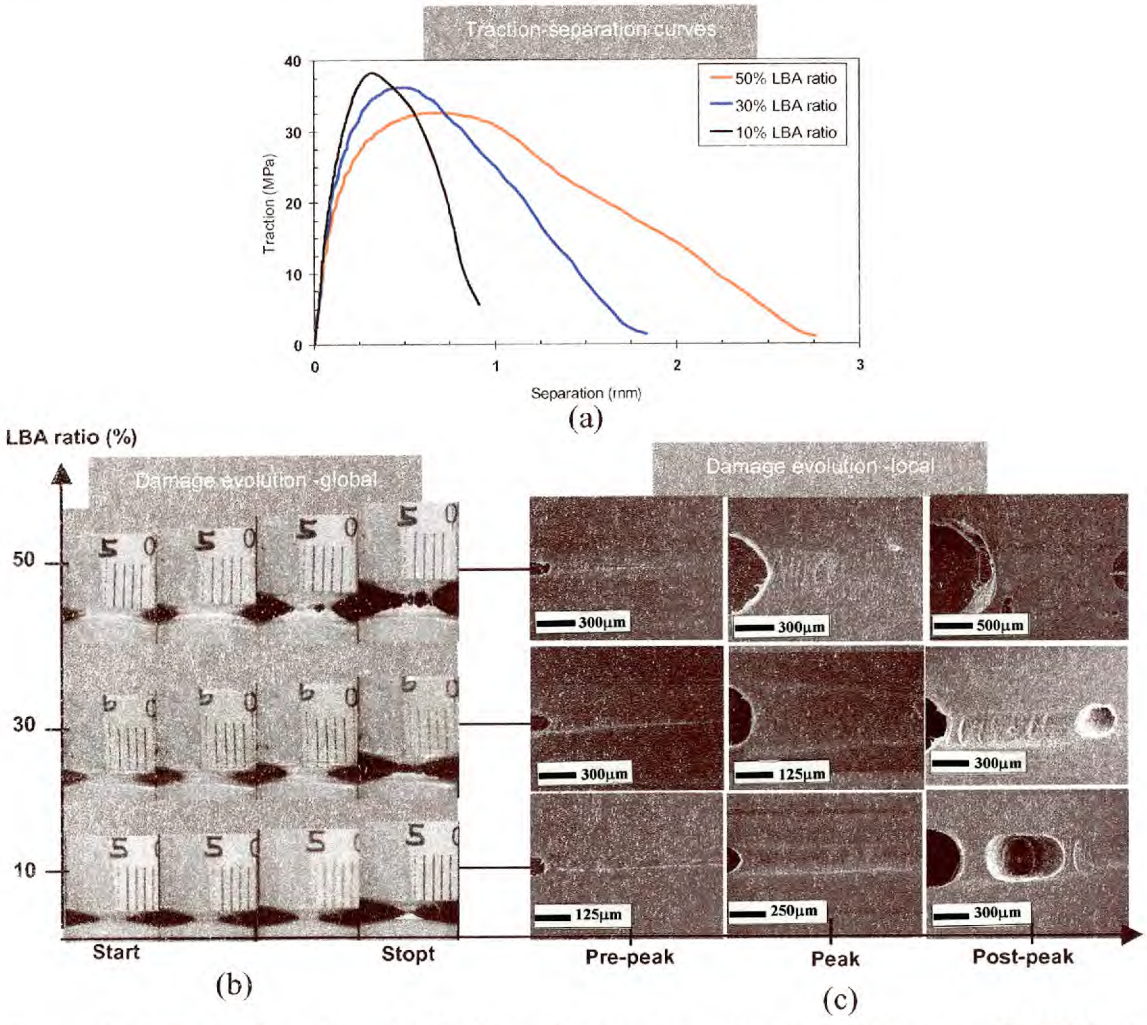

Figure 5.21 The effect of notch depth on the traction-separation behaviour of HDPE at 0.5mm/min. The specimen thickness is 10mm. (a) The measured traction-separation curves. (b) Photographs showing the sequence of fracture during testing. (c) SEM micrographs of sectioned specimen examined at different stages of loading.

Once again, the peak stress falls with increasing LBA ratio. Increasing the LBA ratio, on the other hand, increases the separation distance and hence the total energy values. At a LBA ratio above 10%, the process of blunting is not fully apparent from the images in Figure 5.21(b). Instead, the tip material is breached as the test proceeds which

resulted in the crack initiation. Upon examination of the notch tip structure in Figure 5.21(c), a well defined single craze structure at peak is observed. As damage progresses, voiding emerged in the damaged ligament. Subsequently, the materials deforms by a process of void coalescence which grows inward from the notch tips. The rate of the inward crack growth is comparable to the rates measured at 0.005mm/min. The only difference is the absence of the localised fibrillation process as the crack grows inward.

The traction-separation properties measured at 50mm/min are given in Figure 5.22.

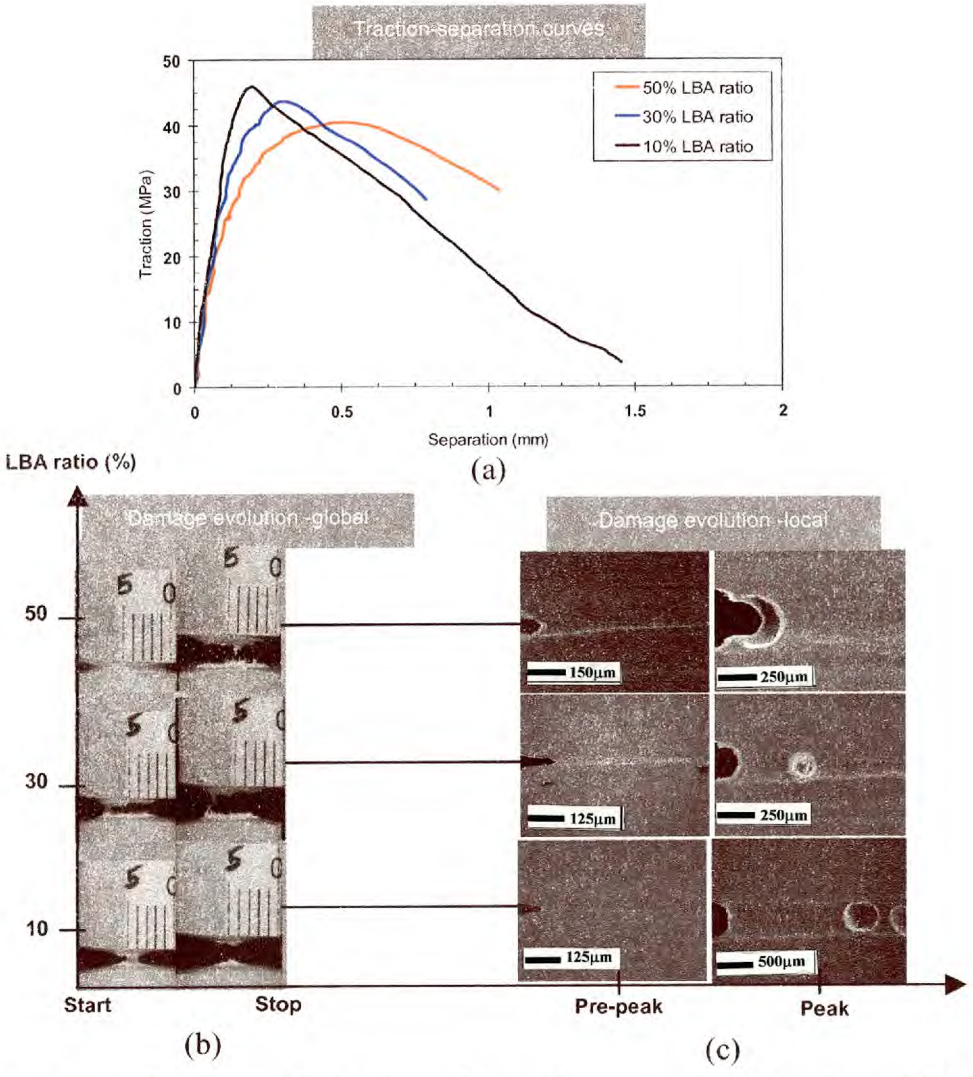

Figure 5.22 The effect of notch depth on the traction-separation behaviour of HDPE at 50mm/min. The specimen thickness is 10mm. (a) The measured traction-separation curves. (b) Photographs showing the sequence of fracture during testing. (c) SEM micrographs of sectioned specimen examined at different stages of loading.

The peak stress in Figure 5.22(a) falls with increasing LBA ratio as expected. At this speed, the peak stresses denote the cohesive strength representing the formation of a uniformly damaged ligament. Increasing the test rates has the effect of decreasing the break separation values as was seen also by the copolymers. As can be seen that the 30% and 50% LBA ratio curves failed in a brittle manner whereas the behaviour is more stable in the 10% LBA ratio curve. As it was too unstable to clamp the specimen, it is not possible to analyse the sectioned specimens at the post-peak stages. In the absence of tip blunting (Figure 5.22(b)), there is nevertheless clear evidence that further extension beyond the peak resulted in the immediate crack growth through void coalescence (Figure 5.22(c)).

5.3.5 Comparison of the fracture surfaces

Figures 5.23 to 5.26 show the fracture surfaces for PE80, PE100, BMPE and HDPE respectively. In each figure, the fracture surfaces are arranged in a x-y coordinate according to their LBA ratio and test speed. It can be seen in the Figure 5.23 that the fracture surface of PE80 showed a transition from craze fibril failure at low LBA ratio and at high test speed to one which exhibited gross drawing and macroscopic necking at high LBA ratio and at low test speed. The fracture surface of PE100, on the other hand, shows a hollow neck appearance (Figure 5.24) at high LBA ratio and at low test speed, indicating a shear mechanism near the surface and crazing on the interior. By comparison, the tip materials of BMPE experience higher fibril drawing with increasing LBA ratio at falling test speed (Figure 5.25). The more blunted tip increases the post-peak extension and thus delayed the onset of the crack growth process. By comparison, the HDPE showed a transition to localised materials fibrillation due to the inward crack growth (Figure 5.26)

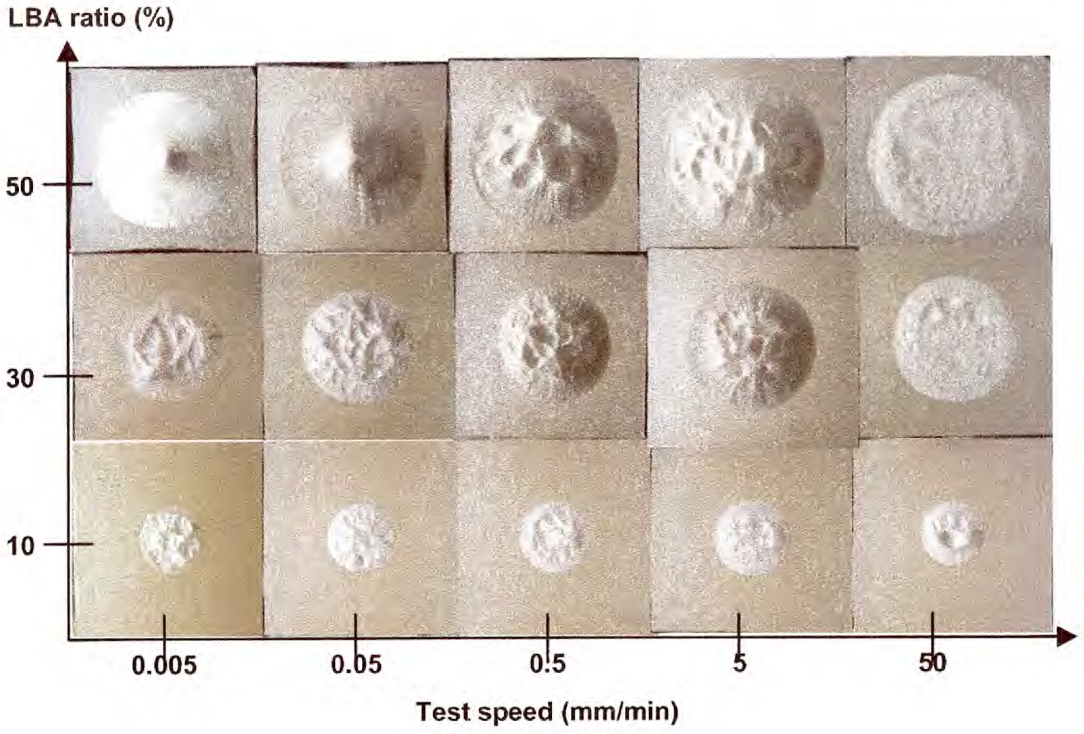

Figure 5.23 Comparison of the fracture surface of PE80 for different LBA ratios and test speeds with a 10mm specimen thickness. The photos are taken from a digital camera.

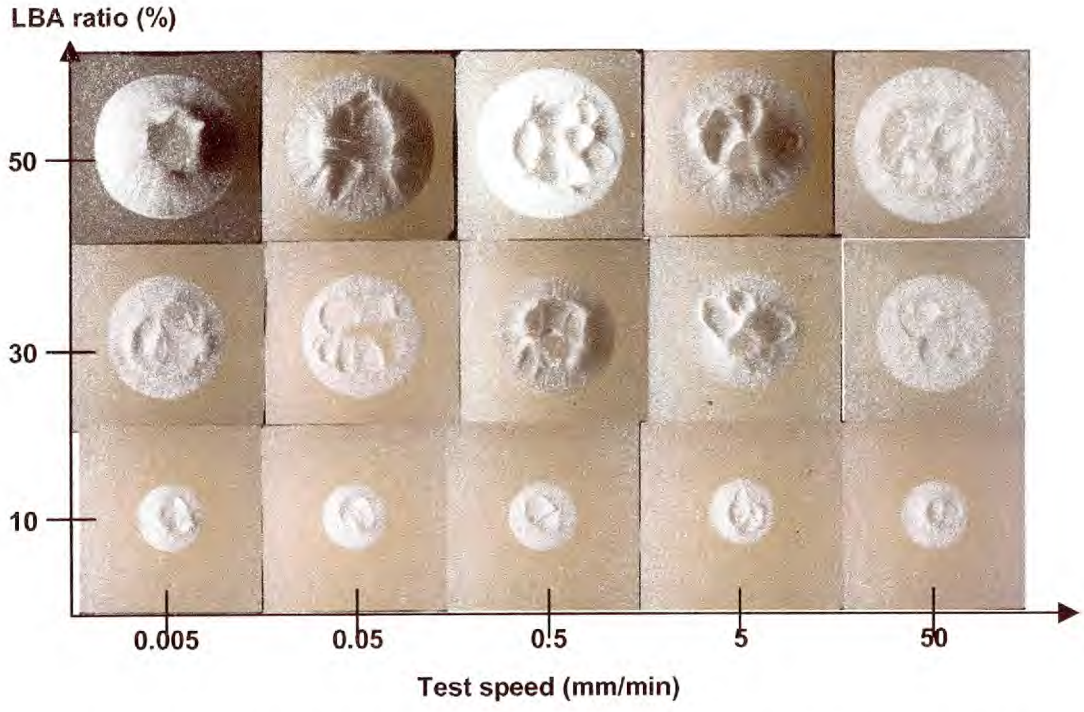

Figure 5.24 Comparison of the fracture surface of PE100 for different LBA ratios and test speeds with a 10mm specimen thickness. The photos are taken from a digital camera.

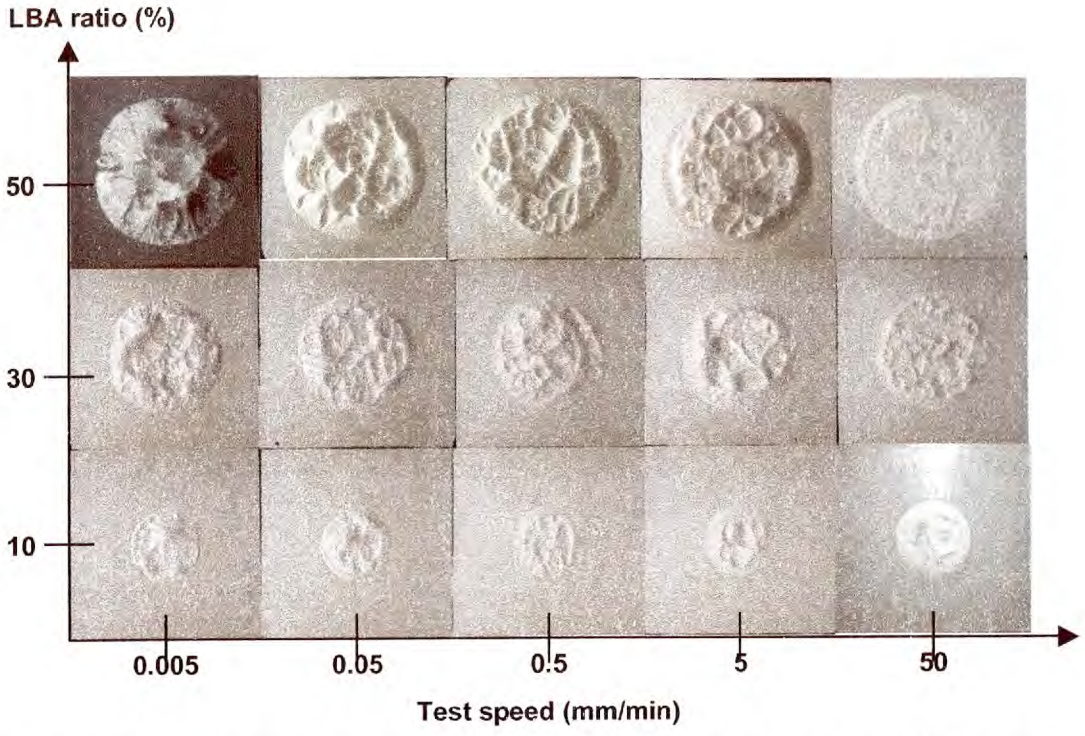

Figure 5.25 Comparison of the fracture surface of BMPE for different LBA ratios and test speeds with a 10mm specimen thickness. The photos are taken from a digital camera.

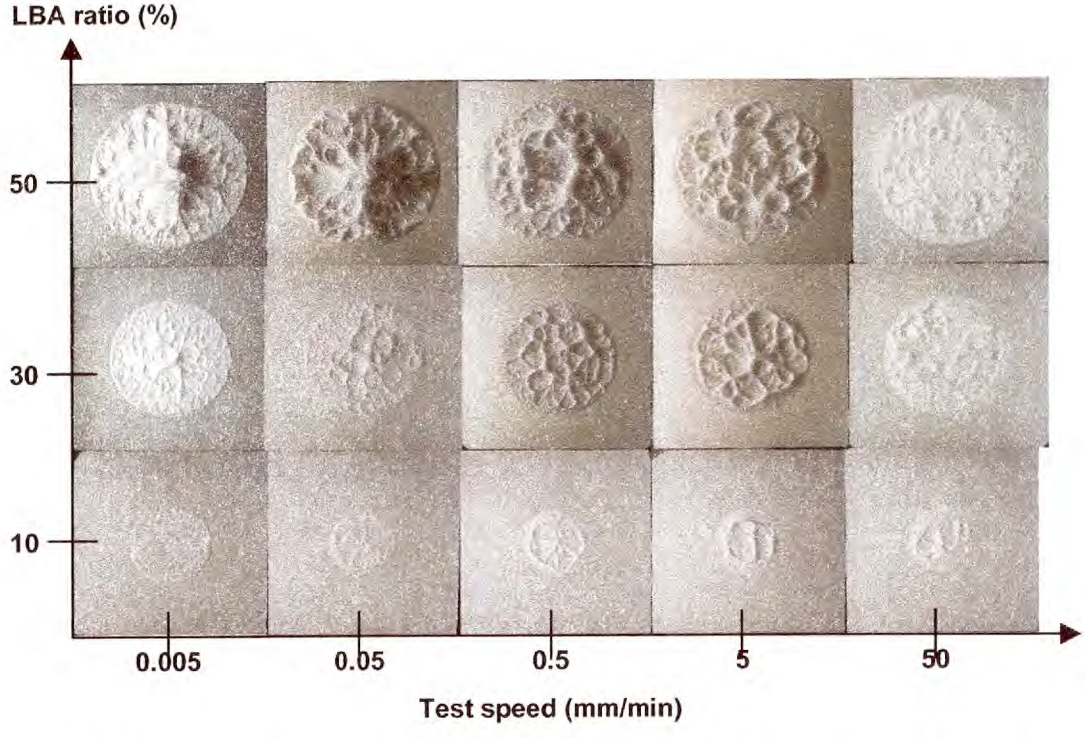

Figure 5.26 Comparison of the fracture surface of HDPE for different LBA ratios and test speeds with a 10mm specimen thickness. The photos are taken from a digital camera.

5.3.6 Summary of the effect of notch depth results

According to the results of the proceeding sections, the fracture surface/failure mechanism changes as the LBA ratio and test speed are varied. The change was most apparent for increasing LBA ratio at low speed. The effect of notch depth (i.e LBA ratio), on the other hand, appears less influential at high speeds. For a given notch depth, the change in the fracture behaviour is apparent across the entire speeds range. On the whole, the deeper the notch, the higher is the plastic flow constraint. Hence, a specimen with a 10% LBA ratio is likely to have the highest constraint while the 50% LBA ratio specimens would have the lowest constraint. In general, at a LBA ratio of 10%, the fracture surfaces showed constrained low-energy brittle failure where cavitation was preferred. As the LBA ratio increases, there was insufficient constraint to generate diffuse voiding in the ligament. As a result, the notch tip material flows more readily to blunt the tip. In some cases, it led to the formation of a continuous film on the outer rim of the fracture surface rather like the shear lips normally associated with plane stress fracture. Consequently, the energy to break at high LBA ratio was significantly higher. Normally, at low-intermediate test speeds and regardless of the LBA ratio, the peak stress denoted the onset of localised deformation at the notch tip due to the strain rate gradient from the notch tip to the craze tip. In moving towards higher rates, the peak represented the formation of a uniformly damaged ligament. These result are in substantial agreement with those of Pandya *et. al.* [2003a]. In summary, the onset and subsequent behaviour of the damage (craze) was found to be sensitive to the notch depth effects. As the constraint level was lowered, changes in the damage behaviour were observed thereby affecting the overall energy dissipated. It was noticed that at high constraint condition, the traction-separation properties were usually characterised by a small separation distance due to the limited extension of the craze. In contrast, at low constraint and low rate conditions the materials demonstrated a ductile response through distinctly different deformation mechanisms. As a result, the shape of the traction curves was broader due to the higher break extension value while increases the energy to break significantly.

5.4 The effect of specimen thickness

Figures 5.27 to 5.30 show the effect of specimen thickness on the traction-separation properties for PE80, PE100, BMPE and HDPE respectively.

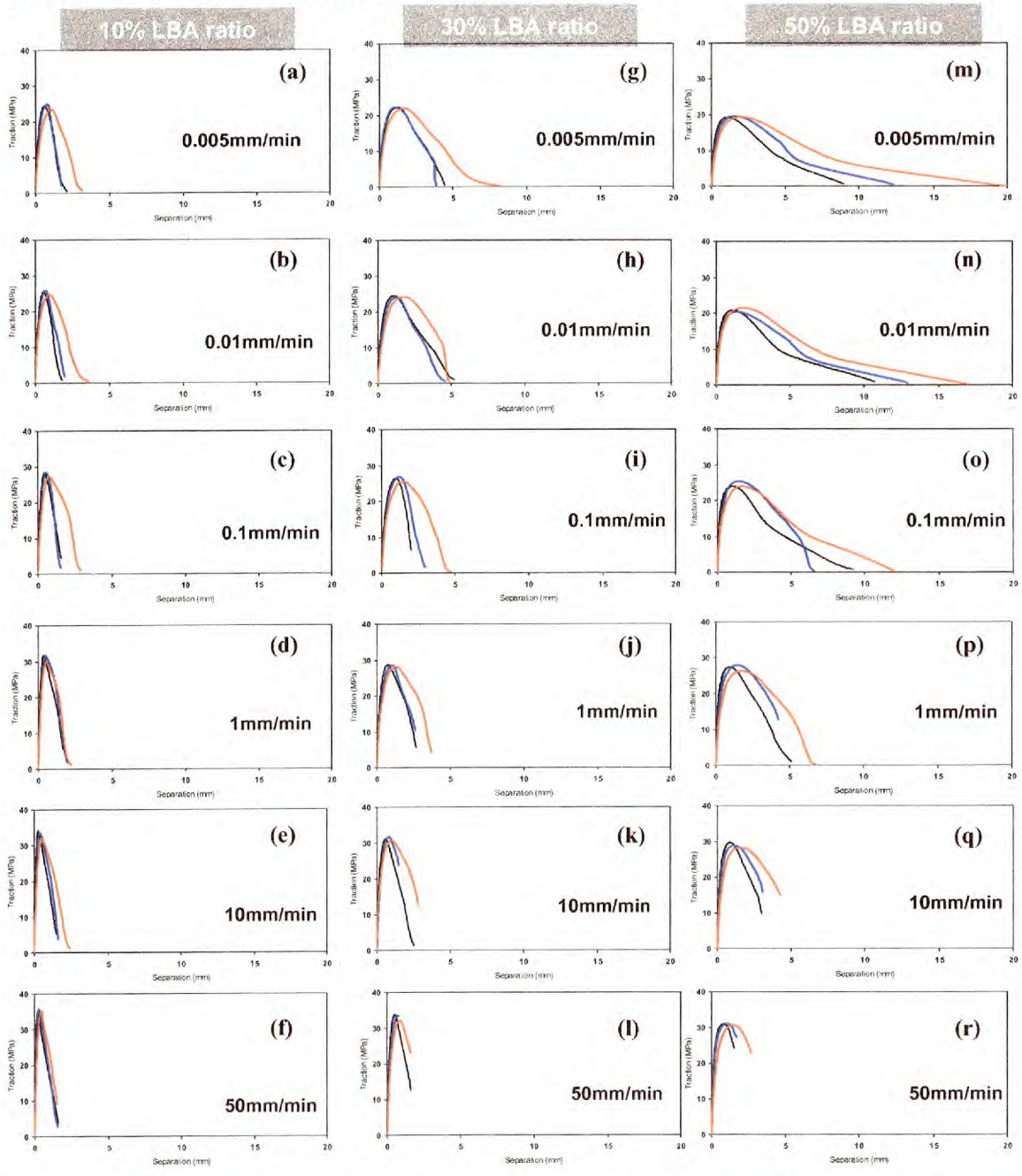

Figure 5.27 Size effects on the traction-separation properties of PE80. Specimens with 10% LBA ratio are shown in (a) to (f). Specimens with 30% LBA ratio are shown in (g) to (l). Specimens with 50% LBA ratio are shown in (m) to (r). The test speed is indicated in each graph. The specimen thickness is indicated as follows: black curve – 10mm specimen thickness, blue curve – 16mm specimen thickness and red curve – 20mm specimen thickness.

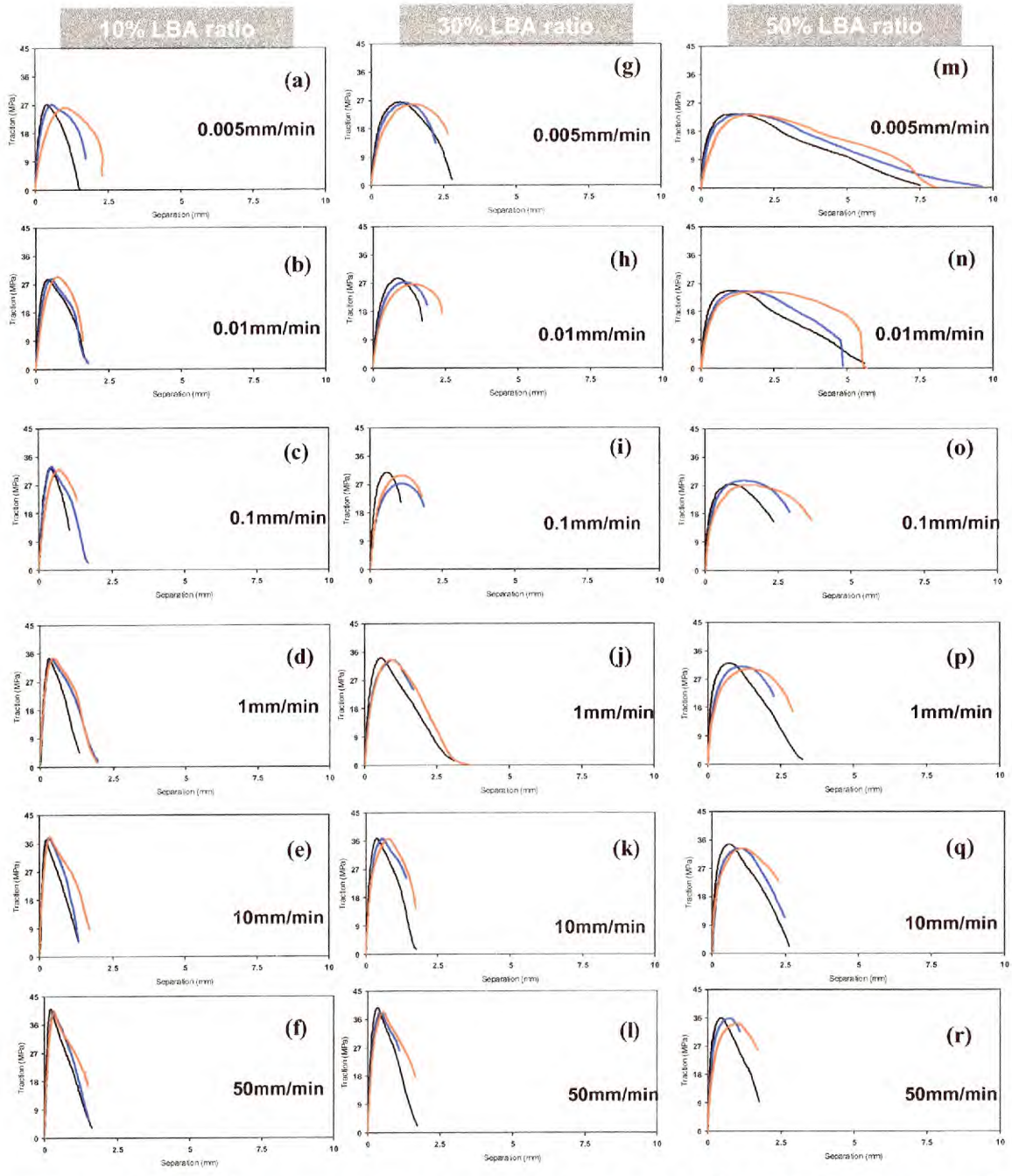

Figure 5.28 Size effects on the traction-separation properties of PE100. Specimens with 10% LBA ratio are shown in (a) to (f). Specimens with 30% LBA ratio are shown in (g) to (l). Specimens with 50% LBA ratio are shown in (m) to (r). The test speed is indicated in each graph. The specimen thickness is indicated as follows: black curve – 10mm specimen thickness, blue curve – 16mm specimen thickness and red curve – 20mm specimen thickness.

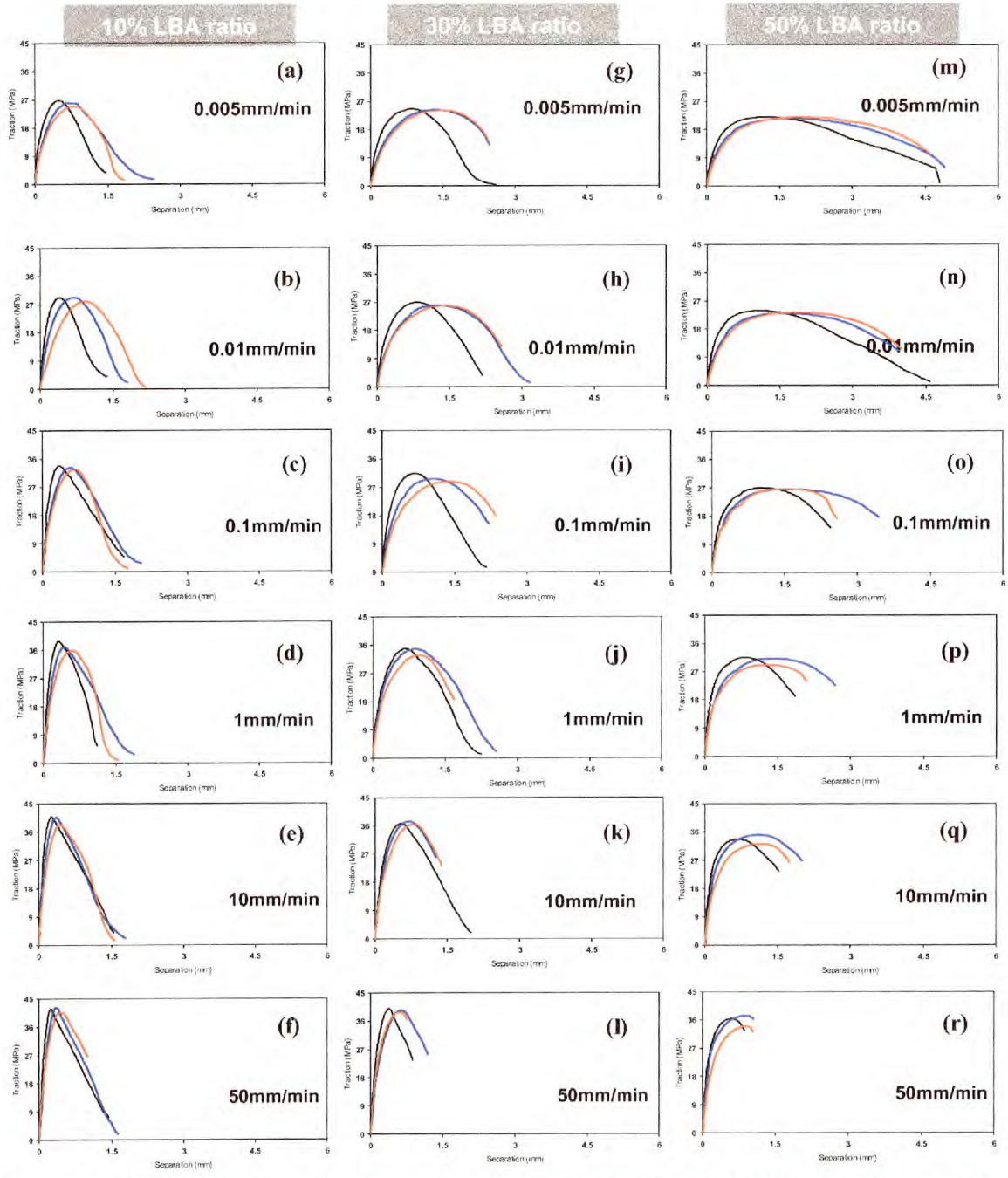

Figure 5.29 Size effects on the traction-separation properties of BMPE. Specimens with 10% LBA ratio are shown in (a) to (f). Specimens with 30% LBA ratio are shown in (g) to (l). Specimens with 50% LBA ratio are shown in (m) to (r). The test speed is indicated in each graph. The specimen thickness is indicated as follows: black curve – 10mm specimen thickness, blue curve – 16mm specimen thickness and red curve – 20mm specimen thickness.

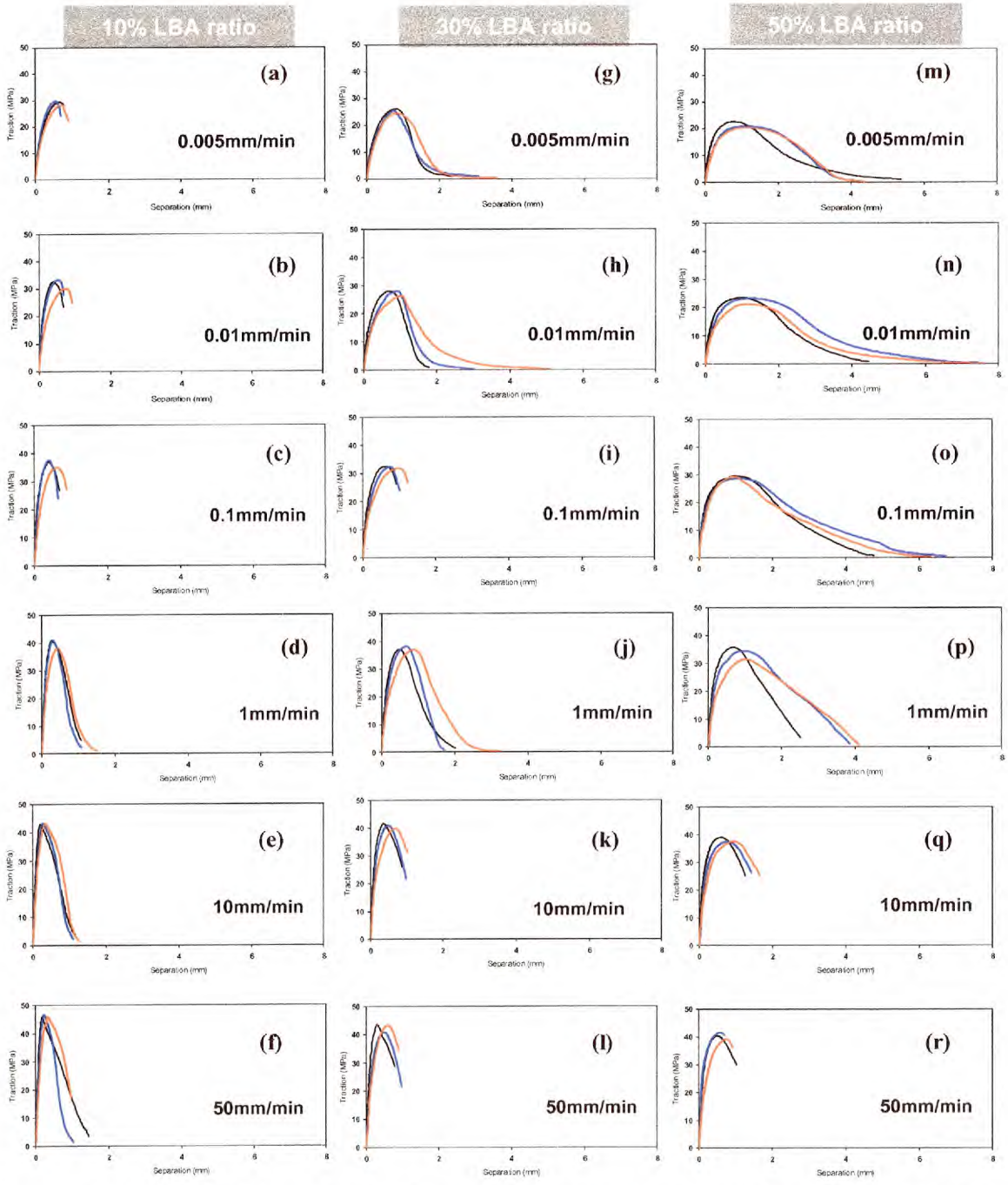

Figure 5.30 Size effects on the traction-separation properties of HDPE. Specimens with 10% LBA ratio are shown in (a) to (f). Specimens with 30% LBA ratio are shown in (g) to (l). Specimens with 50% LBA ratio are shown in (m) to (r). The test speed is indicated in each graph. The specimen thickness is indicated as follows: black curve – 10mm specimen thickness, blue curve – 16mm specimen thickness and red curve – 20mm specimen thickness.

In each figure, the first column ((a) to (f)) compares the traction curves of different sized specimens with a 10% LBA ratio. In the second column ((g) to (l)), the LBA ratio is increased to 30% while the third column ((m) to (r)) the LBA ratio is 50%. The traction-separation behaviour of the 10mm thickness specimen is represented by the black curve whereas the blue curve denotes the behaviour of the 16mm thickness specimen. The red curve corresponds to the traction-separation properties of 20mm specimen thickness. The experiments were performed between the speeds of 0.005 and 50 mm/min. The test speed is indicated in each graph.

The effect of thickness on the traction-separation properties of PE80 is shown in Figure 5.27. It can be seen from the Figures 5.27(a) to 5.27(f) that the constraint of the 10mm curve is more or less the same as the 16mm curve. In terms of the peak stress and separation distance, it is also about the same between the curves. The behaviour of the 20mm curve, on the other hand, showed a broader shape at low and intermediate speed due to a higher separation distance. Interestingly, as the test speed increases, the behaviour of 20mm curve resembles those of 10mm or 16 mm curves. One possible explanation is that the rate effects begin to take precedence over the effect of size. Examination of the fractures surfaces in Figure 5.31(a) shows that the fracture appearance between the different sized specimens is almost identical. As the LBA ratio is increased to 30% (Figures 5.27(g) to 5.27(l)), the trend observed is similar to the response at 10% LBA ratio. A similar argument to that invoked earlier can be used here. The most remarkable feature observed when the LBA ratio is 50% (Figures 5.27(m) to 5.27(r)) in that the characteristic of the traction-separation behaviour between the curves is very similar. There is evidence to be found from the fracture appearances given by Figure 5.31(b). It can be seen that the features of the surfaces between different sized specimens for instance, at 0.01mm/min is exactly the same which showed a fractured neck. Clearly, the same mechanism was responsible for the failure. On the whole, as the test speed was increased, the break separation values were reduced. The peak stress, on the other hand, showed an upward trend. More importantly, at a given test speed, the peak stress remained relatively constant with thickness. The traction-separation properties examined in PE100 (Figure 5.28), BMPE (Figure 5.29) and HDPE (Figure 5.30) produced similar analyses with those described in Figure 5.27 for the PE80. The

examination of the fracture surfaces in Figure 5.32 to 5.34 also supported the findings. These findings seem to suggest that the variation in constraint is not significant for fixed LBA ratio specimens of different thickness.

5.4.1 Summary of the effect of size results

At a given LBA ratio and test speed, the difference in the geometric constraint between the 10mm and 16mm or 20mm specimens may not be significant. The results of Figures 5.27 to 5.30 provided the evidence on the basis that there is negligible difference in the stress, separation and energy values between the different sized specimens. The fractured specimens given in Figures 5.31 to 5.34 also supported the findings. For instance, at a given test speed, the surface features between the different sized specimens shared common fracture characteristics, suggesting that the failure mechanism is the same. By comparison, the constraint was found to increase with an increase in the notch depth as examined in § 5.3. It would appear that the effect of (geometrical) constraint is likely a function of the notch depth and independent of the specimen thickness.

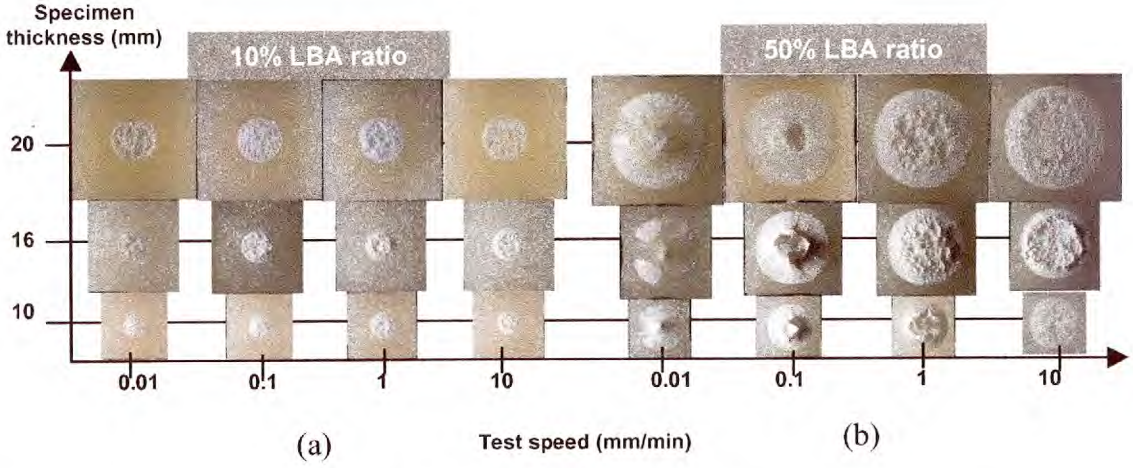

Figure 5.31 Comparison of the fracture surface of PE80 for different thickness at various test speeds. Specimens with (a) 10% and (b) 50% LBA ratio.
The photos are taken from a digital camera.

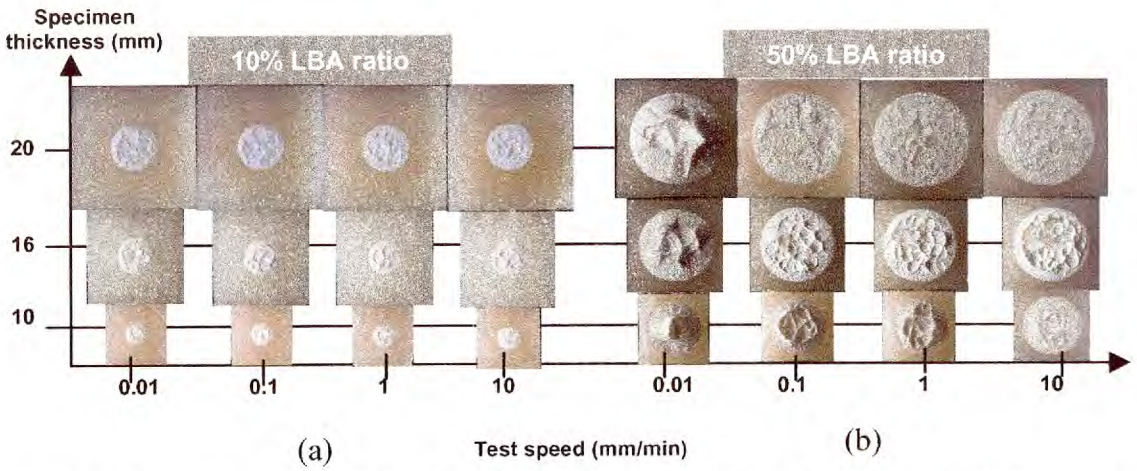

Figure 5.32 Comparison of the fracture surface of PE100 for different thickness at various test speeds. Specimens with (a) 10% and (b) 50% LBA ratio.
The photos are taken from a digital camera.

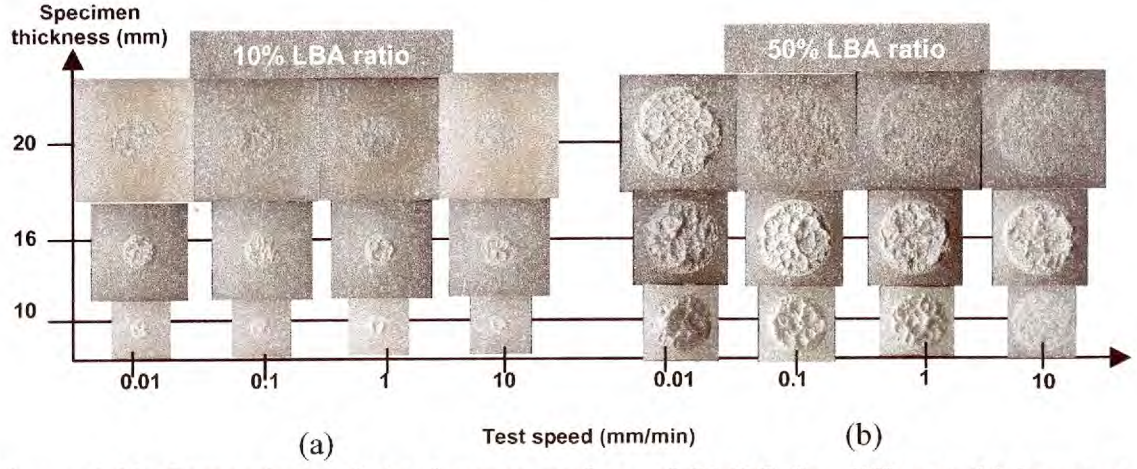

Figure 5.33 Comparison of the fracture surface of BMPE for different thickness at various test speeds. Specimens with (a) 10% and (b) 50% LBA ratio.
The photos are taken from a digital camera.

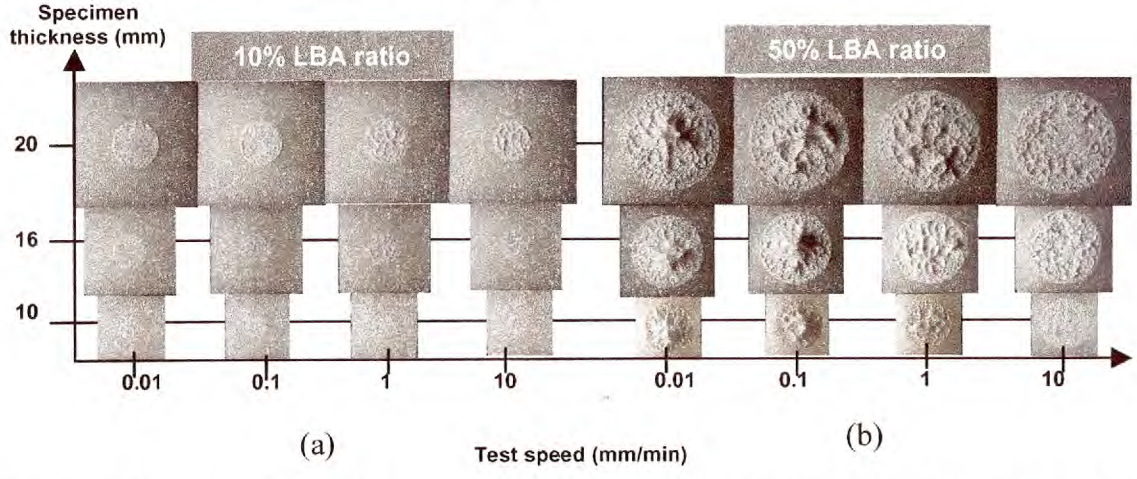

Figure 5.34 Comparison of the fracture surface of HDPE for different thickness at various test speeds. Specimens with (a) 10% and (b) 50% LBA ratio.
The photos are taken from a digital camera.

5.5 The effect of rate

Figure 5.35 shows the effect of rate on the traction-separation behaviour for each grade at different LBA ratio. The specimen thickness is 16mm. A number of tests were carried out under constant speed conditions over a range of loading speeds, from 0.005 to 50 mm/min.

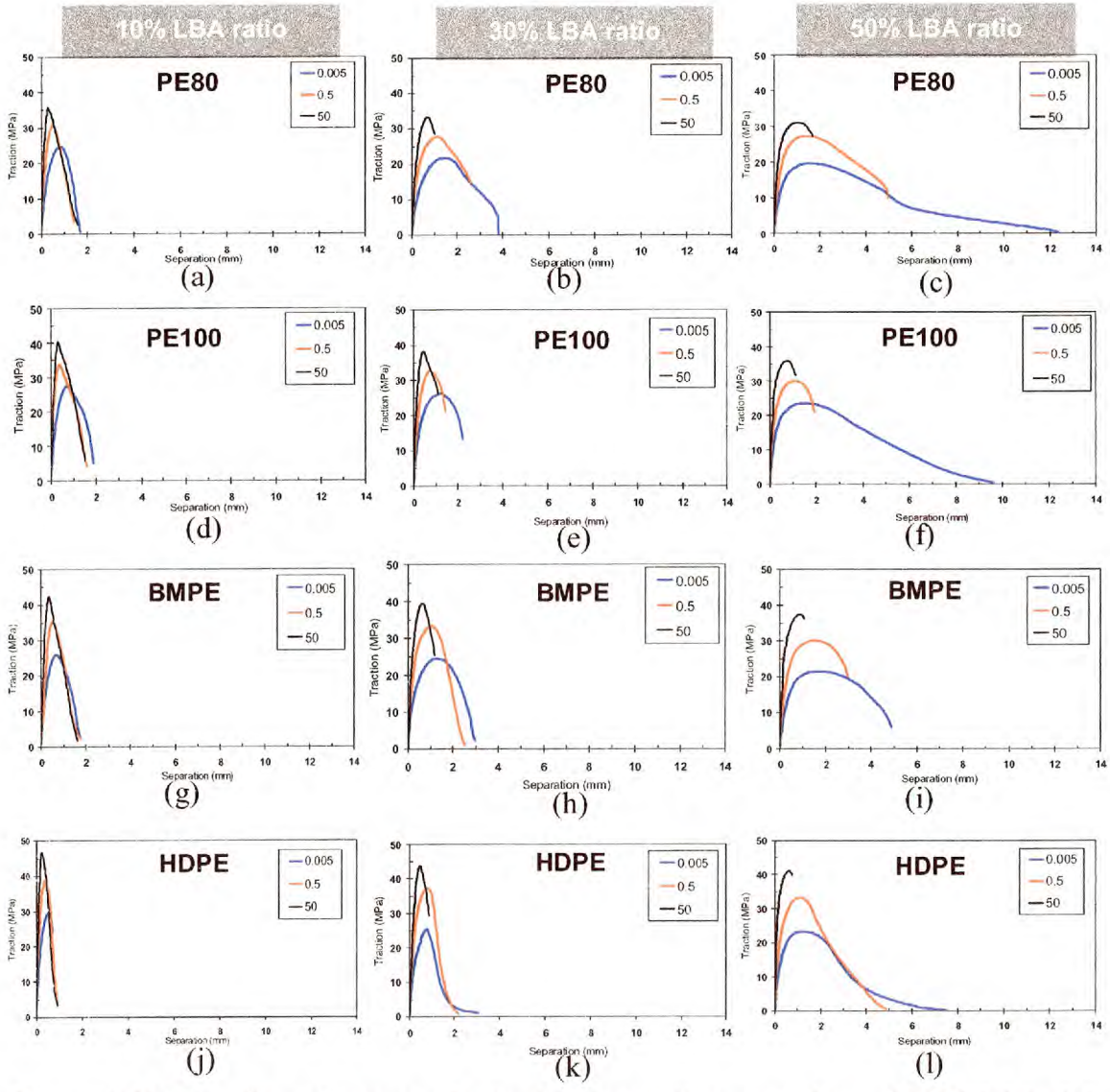

Figure 5.35 The effect of rate on the traction separation properties of PE80 (a) to (c), PE100 (d) to (f), BMPE (g) to (i) and HDPE (j) to (l). The specimen thickness is 16mm.

First, the effect of rate on the traction-separation properties at 10% LBA ratio is considered. As can be seen in Figure 5.35 (a), the peak stress of PE80 falls as the test speed decreases. The trend of falling peak stress with speed is a feature common to all

the grades. The dependency of the stress upon the test rates has been described in chapter 4 whereby the yield stress falls with falling test speed. As can be seen, the separation distances between the curves are comparable. The notable difference is in the shape of the curve being broader with falling test speed because of a smoother peak region. Consequently, the fall in energy value is negligible as the speed is lowered. The length of separation of PE100 (Figure 3.35(d)) is about the same at high and intermediate speeds. The separation distance, however, shows an increase at the lowest speed. The curve profile exhibited a narrow peak at high speeds and it becomes broader with a reduction in test speeds. The rise in the energy value with increased break extension is not large as compared with the value at high and intermediate speeds. This is due to the significant decrease in the peak stress at the low speed but nevertheless this is clear evidence that the PE100 demonstrated an increased resistance to fracture at this condition. The traction curves of BMPE shown in Figure 5.35(g) are similar to that seen in PE80. On the contrary, the break separation of HDPE (Figure 5.35(j)) decreases from an almost constant value at high and medium speeds to a much lower value at low test speeds. At high test speeds, the fracture surfaces between the grades showed a common feature that is marked by large voids as seen in Figure 5.36. The descending slope of the traction curves therefore corresponded to the softening behaviour due to void growth and coalescence.

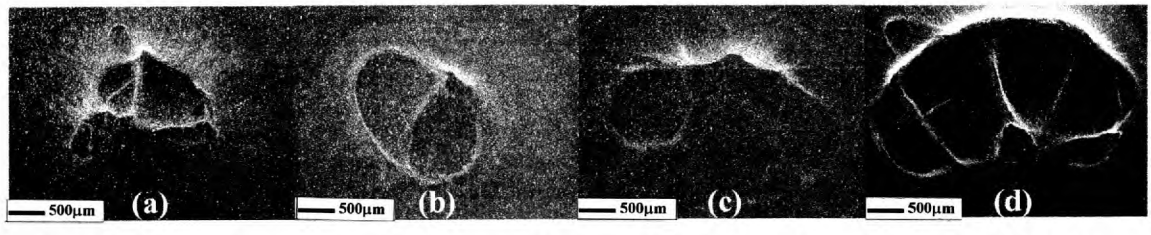

Figure 5.36 Fracture surfaces of (a)PE80, (b)PE100, (c)BMPE and (a)HDPE at 50mm/min. The LBA ratio is 10%.

On the other hand, the fracture features at 0.005mm/min given by Figure 5.37 are distinct between the grades. PE80 showed a surface consisted of a large number of voids interspersed between fibrils. By comparison, there were fewer voids in PE100. However, the surface actually comprised of a network of finely drawn fibrils as described previously by Pandya [2000]. In contrast, the fracture surface of BMPE made

up of warped films as opposed to the distinct fibrils seen in PE80. HDPE showed a rough and level texture with little sign of raised fibrils.

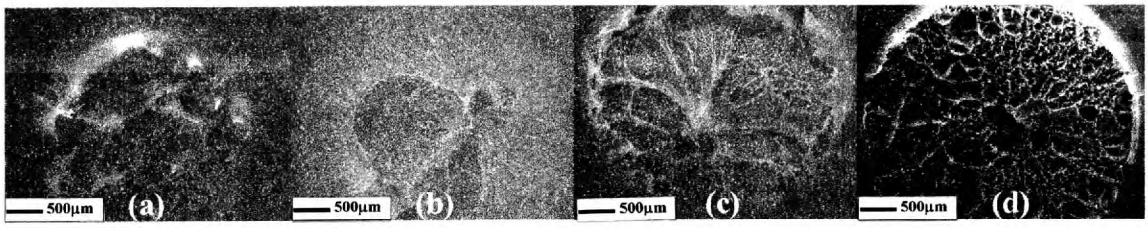

Figure 5.37 Fracture surfaces of (a)PE80, (b)PE100, (c)BMPE and (a)HDPE at 0.005mm/min. The LBA ratio is 10%. (x35)

At 30% LBA ratio, the rate dependent trends in the peak stress, which falls with the rates of testing, is observed in all the grades as given in the Figures 5.35(b), 5.35(e), 5.35(h) and 5.35(k). The main difference with the earlier analysis is that the separation distance showed an increase with decrease in test rates. For the copolymers, the energy values increase with decreasing test speeds. The reason for higher energy values was mainly due to the constraint dependent rise in the break extension value which negated the effect of falling peak stress that accounted for the loss in the energy values at 10% LBA ratio. On the contrary, the energy values of HDPE between 50 and 0.005 mm/min are comparable. At high rates of testing, the fracture surfaces in Figure 5.38 showed a rough and level texture consisted of islands or patches of craze matters. Such a feature is usually referred to as the mackerel pattern which is a variant of the patch pattern. This brittle-type behaviour is characterised well by the 50mm traction curve which displayed a brittle post-peak extension as seen in Figures 5.35(b), 5.35(e), 5.35(h) and 5.35(k). As the rate of testing is reduced to 0.005 mm/min, the features between the grades are unique as shown in Figure 5.39. The failure mechanisms of each grade have been identified separately in Figures 5.2, 5.8, 5.15, and 5.20 for PE80, PE100, BMPE and HDPE respectively.

Increasing the LBA ratio to 50%, one notes again the typical feature of the rate effects on traction curves: the fall in peak stress with speed while the separation distance increases as shown in Figures 5.35(c), 5.35(f), 5.35(i) and 5.35(l). It can be seen that the increase in the separation distance at 0.005mm/min for the PE100 is exceptionally high in relation to the higher speeds traction curves (Figure 5.35(f)). According to the figures, each material is capable of undergoing markedly different amounts of extension

that could be related to the mode of the deformation mechanisms which was examined in § 5.3. There is also evidence to be found in the fracture surface tested to failure at 0.005 mm/min as shown in Figure 5.40. The distinct fracture features exhibited by each grade would seem to stem from the differences in the structural properties, in additional to the constraint conditions. In contrast, the features between the grades compared at high rates are more or less the same (Figure 5.41), indicating the dominance of rate effects at this condition. A similar deduction can be drawn upon for the results discussed for the 10% and 30% LBA ratio.

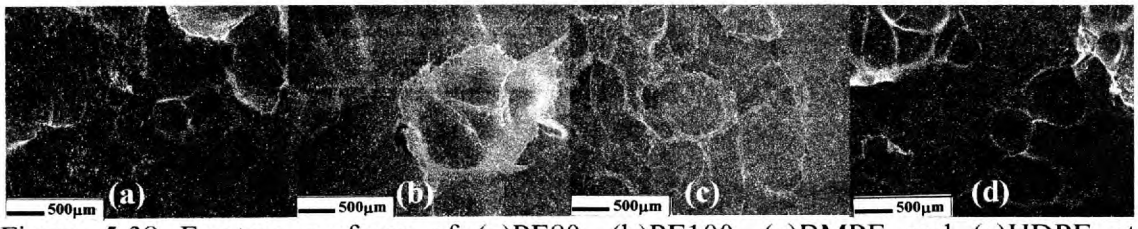

Figure 5.38 Fracture surfaces of (a)PE80, (b)PE100, (c)BMPE and (a)HDPE at 50mm/min. The LBA ratio is 30%.

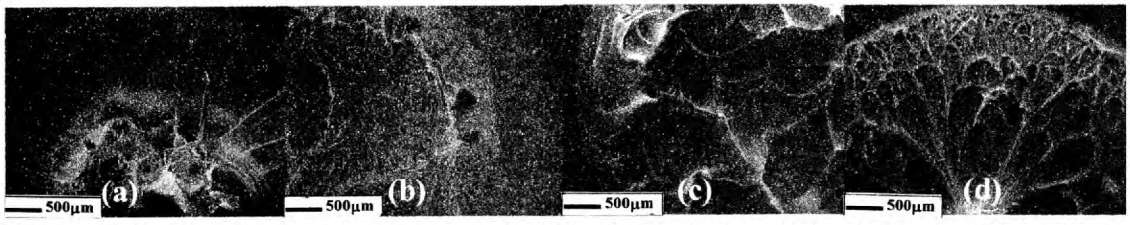

Figure 5.39 Fracture surfaces of (a)PE80, (b)PE100, (c)BMPE and (a)HDPE at 0.005mm/min. The LBA ratio is 30%.

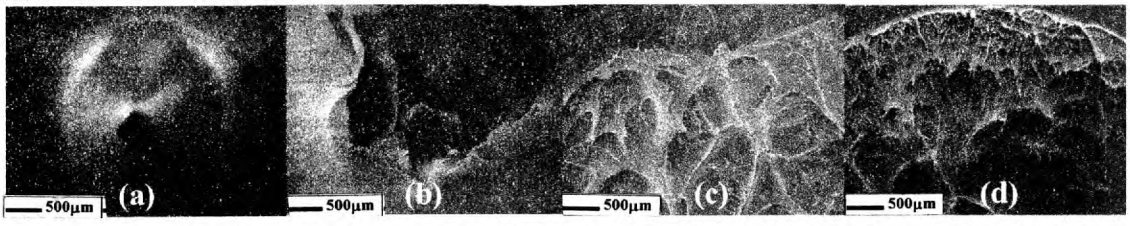

Figure 5.40 Fracture surfaces of (a)PE80, (b)PE100, (c)BMPE and (a)HDPE at 0.005mm/min. The LBA ratio is 50%.

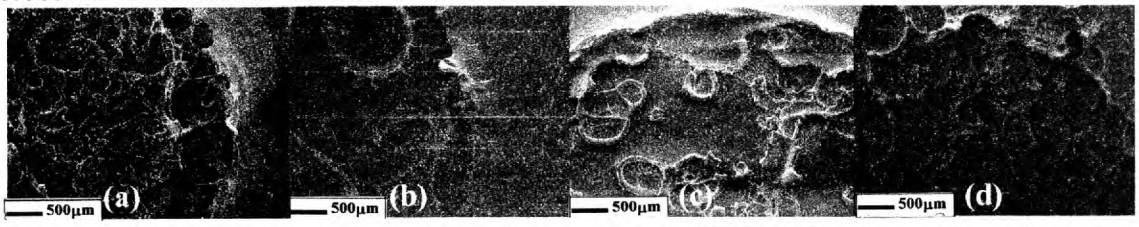

Figure 5.41 Fracture surfaces of (a)PE80, (b)PE100, (c)BMPE and (a)HDPE at 50mm/min. The LBA ratio is 50%.

As the rate of testing approaches the impact regime, the thermal effects become important. As can be seen in the Figure 5.42, there is a noticeable rise in the ligament temperature to around 27°C from the room temperature at 22°C when pulled at a speed of 50 mm/min. The result is not unexpected, given that the poor thermal conductivity of polymer could leads to the slow dissipation of the absorbed energy. For this reason, it could cause adiabatic heating and fibrillar melting thereby restricting the growth of the craze and the material toughness (Leevers [1995]). At low test speeds or quasi-static test conditions, the results indicated isothermal condition because of the longer test times, which allows the temperature (energy) build-up to be dissipated gradually without affecting the stress and displacement behaviour.

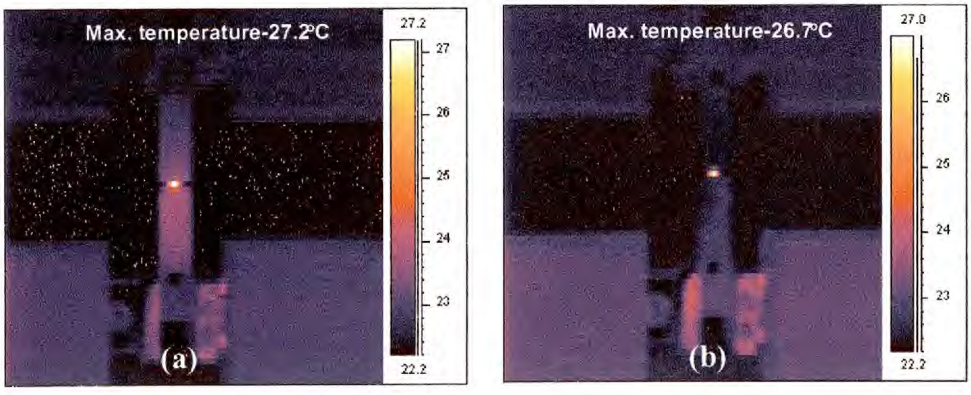

Figure 5.42 Thermal effects on (a) PE80 and (b) HDPE during testing at 50mm/min. The measurements are taken using the thermal scanner which detects the change in the surface temperature of the specimen.

5.5.1 Summary of the effect of rate results

The results demonstrate that the traction-separation properties of the materials are dependent on the rate at which the test is carried out (Pandya [2000]). The peak stress was found to increase with rising test speed. Generally, the tests at low speed found that the separation distance increases with increasing LBA ratio. The raise in break separation values was mainly attributed to the effects of structural properties and the degree of geometrical constraint. On the other hand, the effect of rate exerted a greater influence on the traction-separation behaviour at high test speeds than due to the differences in the molecular structural characteristics or constraints.

5.6 Comparison of the traction-separation behaviour

The traction-separation properties of each grade measured at 0.005 mm/min are shown in Figure 5.43. The LBA ratio is 50% and the specimen thickness is 10mm.

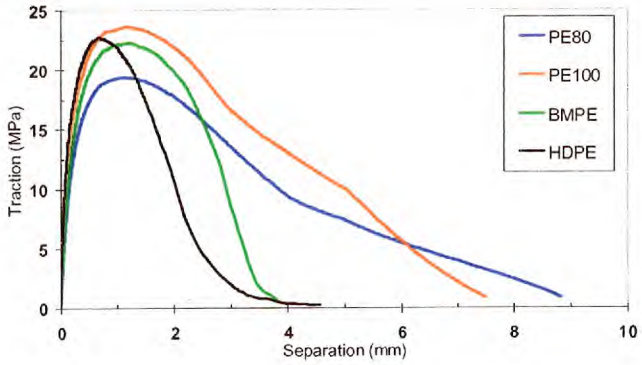

(a)

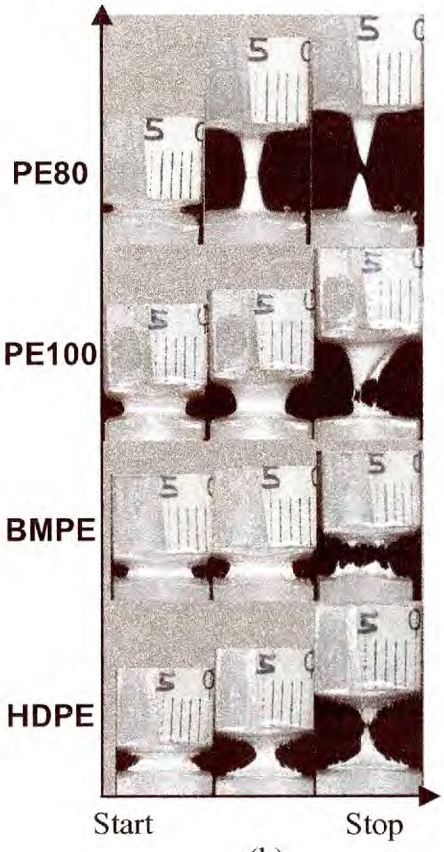

(b)

Figure 5.43 Comparison of the traction-separation behaviour between the different grades at 0.005 mm/min with a 50% LBA ratio. The specimen thickness is 10mm (a) Measured traction-separation curves. (b) The sequence of fracture during testing.

As can be seen from the Figure 5.43(a), the peak stress of PE100 is the highest amongst the materials followed by HDPE, BMPE and PE80. On the other hand, the separation distance is the highest in PE80 followed by PE100 while both of the BMPE and HDPE have comparable extension values. In terms of the separation energy, the energy dissipated in PE100 is the highest whereas HDPE has the lowest energy value. The energy value of BMPE is higher than that of the HDPE but lower than the PE80. The difference in the fracture behaviour between the grades in the Figure 5.43(b) should provide the reasons for the materials performance. It can be seen that PE80 showed large scale drawing from the bulk into the fracture zone causing excessive blunting of the tip, leading to homogenous ductile necking. Similarly, the PE100 shows large

macroscopic shear flows (see also Figure 5.8). By comparison, the degree of blunting (shear flow) in BMPE is lower than that of the pipe materials (see also Figure 5.13). In contrast, the blunting process was absent in HDPE which results in a craze-crack growth like behaviour to emerge (see also Figure 5.20). HDPE showed narrow shaped traction curves as opposed to the broader shaped curves associated with the pipe materials. Between the pipe materials, the energy value of the PE100 is higher than the PE80 due to the combination of high peak stress and large separate distance. Clearly, the manner in which the energy was dissipated via the deformation mechanism determined the overall separation energy. This suggest that PE100 will have a considerably higher resistance to slow crack growth that the others. A discussion of the structure-property relationship between the grades will be presented in the next chapter.

The traction-separation properties of each grade measured at 50 mm/min are shown in Figure 5.44. The LBA ratio is 10% and the specimen thickness is 10mm. As shown in Figure 5.44(a), the similarity in the shape of the curve between the grades is truly striking, suggesting a dominance of effects of rate over the structural properties differences at this rate. The closeness in the fracture behaviour can also be seen in the damaged ligament shown in Figure 5.44(b). The features have been highlighted in Figure 5.36. Apart from the difference in the peak strength, there is no great distinction between the curves. According to Figure 5.44(a), the stress required to produce a craze is highest in HDPE while it is the lowest in PE80. On the other hand, the peak stress between PE100 and BMPE are comparable. The materials ranking based on the yield stress in Figure 4.6 corresponded exactly with the ranking seen here for the peak stress. According to the stress-strain data, the yield strength decreases with the density of the material. Therefore, the plastic deformation would be easier in a low density material, with the low density PE80 exhibiting the lowest crazing (peak) stress than the others. One possible explanation is that the nucleation of microvoids is easier in the low density materials due to a high proportion of free volume.

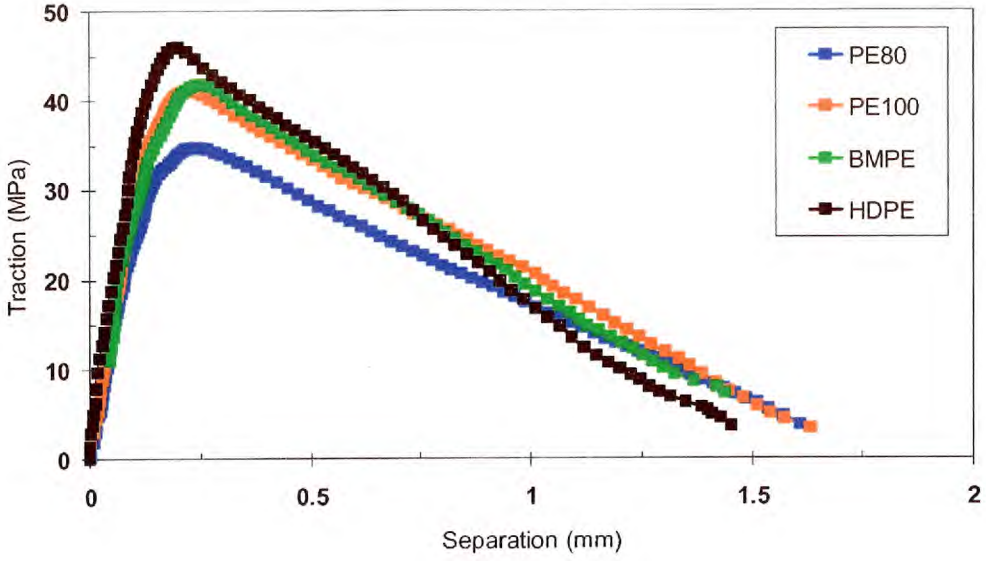

(a)

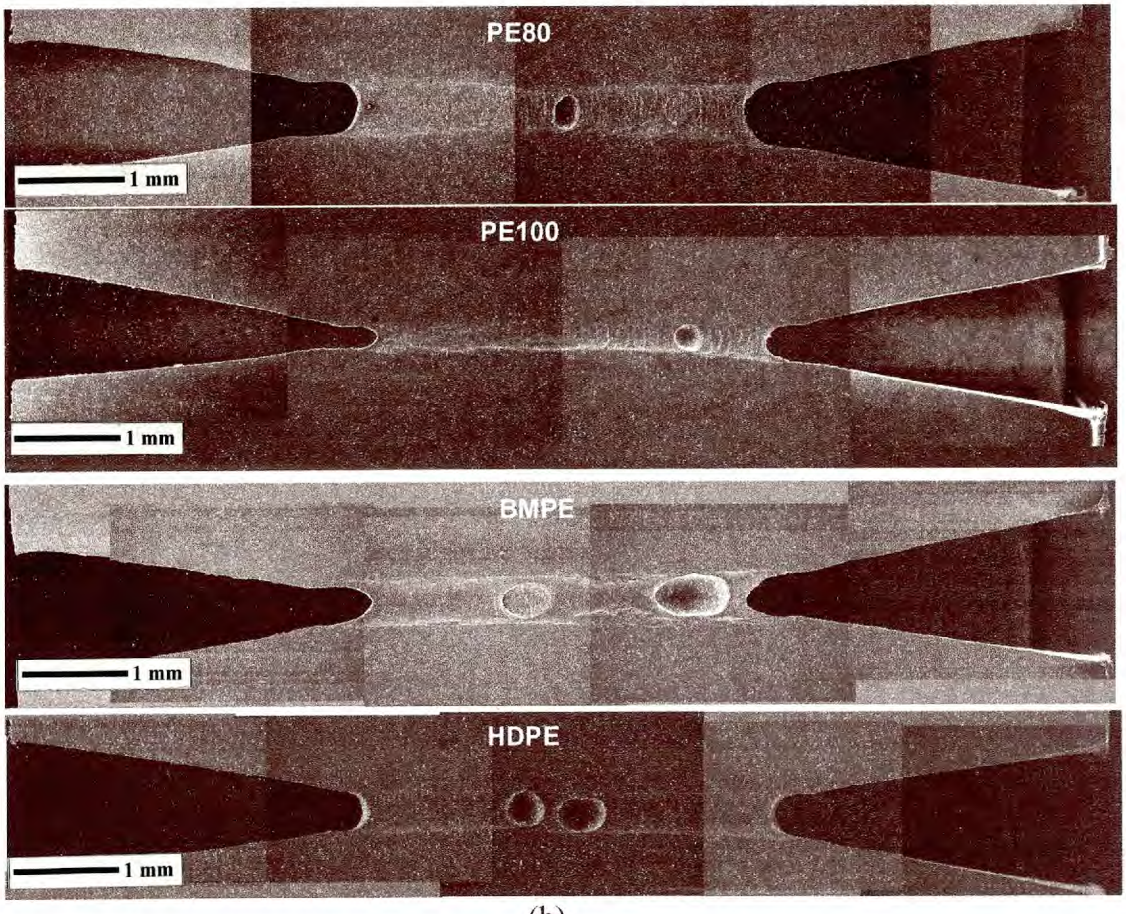

(b)

Figure 5.44 Comparison of the traction-separation behaviour between the different grades at 50mm/min with 10% LBA ratio. The specimen thickness is 10mm. (a) Measured traction-separation curves. (b) The damaged ligament at post-peak stage.

5.7 Variation of the cohesive parameters with rate and constraint

It is clear from the results presented earlier that the measured traction-separation curves are sensitive to the rate and constraint effects. Three parameters that emerged in the foregoing discussion were the cohesive stress, σ_{peak} the cohesive energy, Γ and the separation at decohesion, δ_{break} as illustrated in Figure 5.45. For a given test condition, these parameters provided a unique description of the traction-separation behaviour. Having identified the cohesive parameters, it is now possible to evaluate the variation in the cohesive parameters with rate and constraint. For clarity reason, the results were organised in the following ways. For example, the σ_{peak} data were divided into two groups: notch depth and size effects. Within each group, the data were plotted in the form of σ_{peak} as a function of test speed. In each figure there were six graphs, the first column consisted of three graphs which represented the notch depth effects data while the second column showed the effect of specimen thickness. Under the first column, the first graph compared the data between the 10mm specimens with different LBA ratio while the 16mm and 20mm specimens were shown in the second and third graphs respectively. The graphs were similarly arranged in the second column except that the specimen thickness was varied while the LBA ratio remained constant.

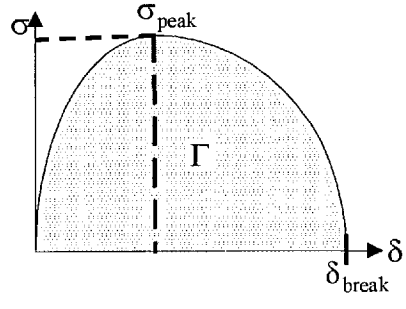

Figure 5.45 A schematic traction-separation curve showing the relationship between the cohesive stress, σ_{peak} the cohesive energy, Γ and the separation at decohesion, δ_{break}.

5.7.1 Variation of cohesive stress with constraint and rate.

Figures 5.46 to 5.49 show the variation of σ_{peak} with test speed of each material at various constraint conditions, along with the σ_y data presented previously in chapter 4.

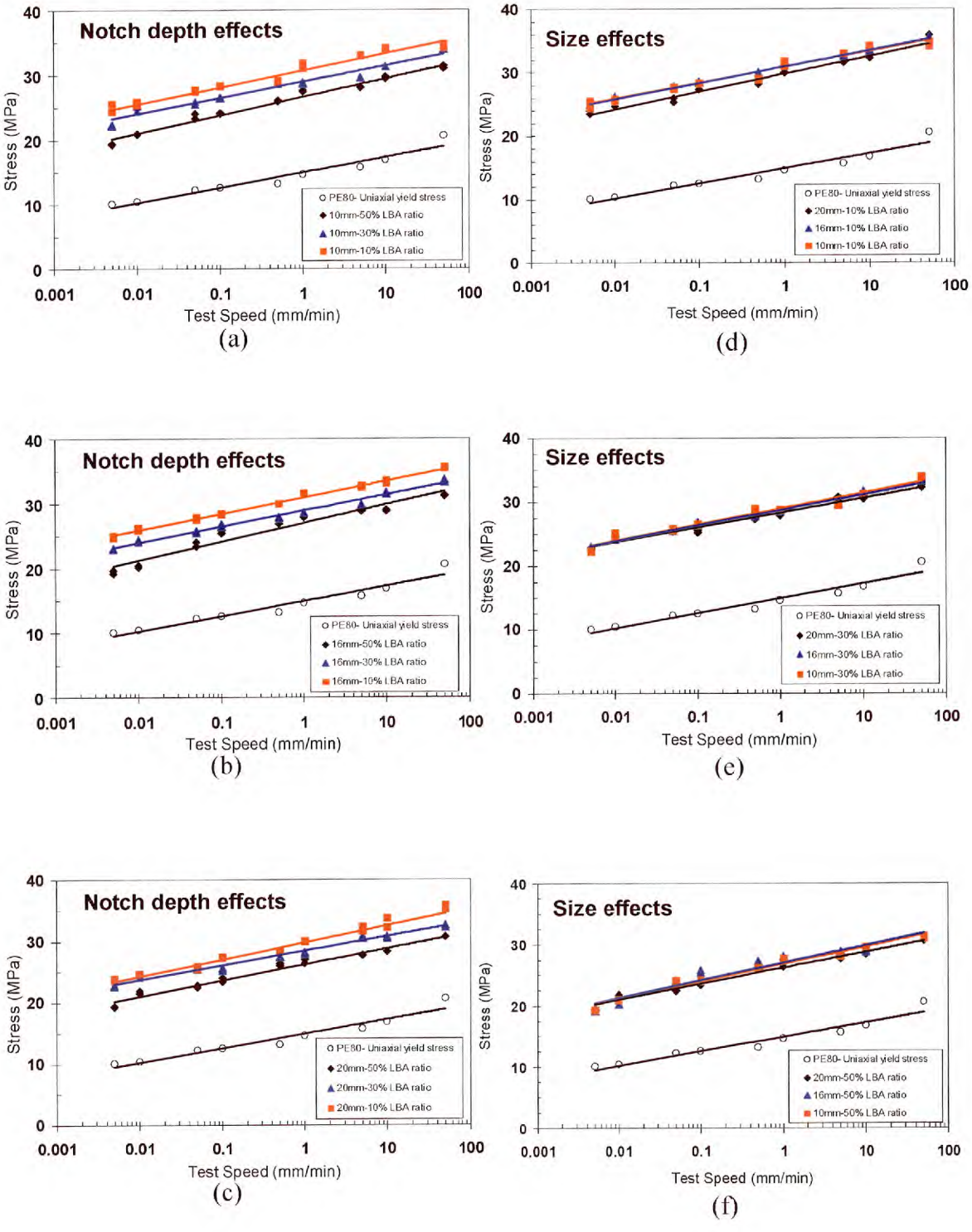

Figure 5.46 The effect of notch depth ((a) to (c)) and specimen thickness ((d) to (f)) on the σ_{peak} of PE80 at various loading speed.

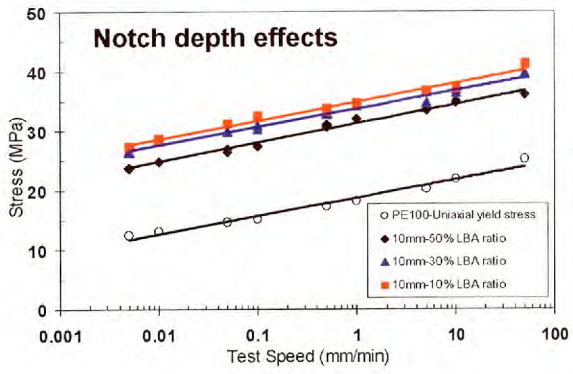

(a)

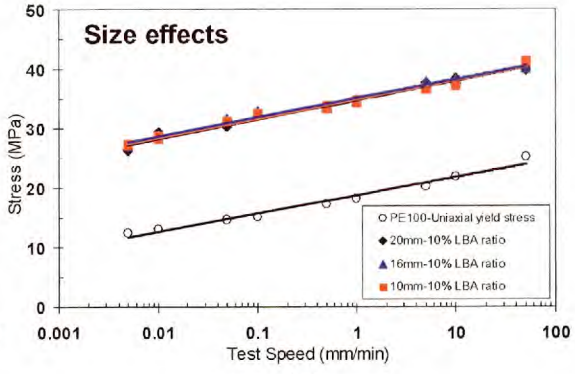

(d)

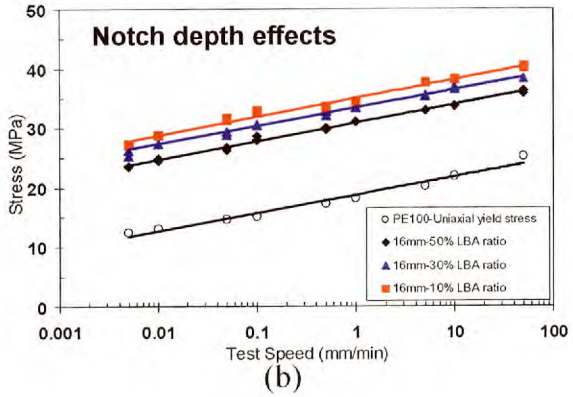

(b)

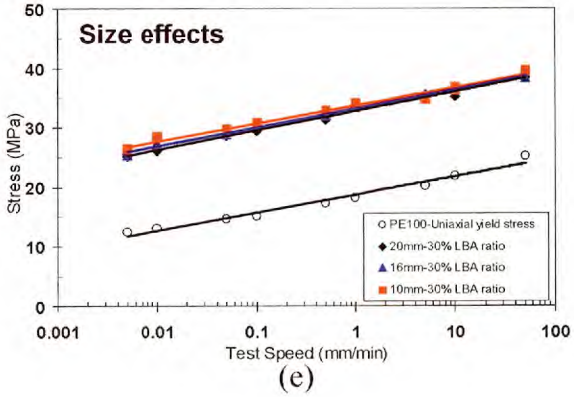

(e)

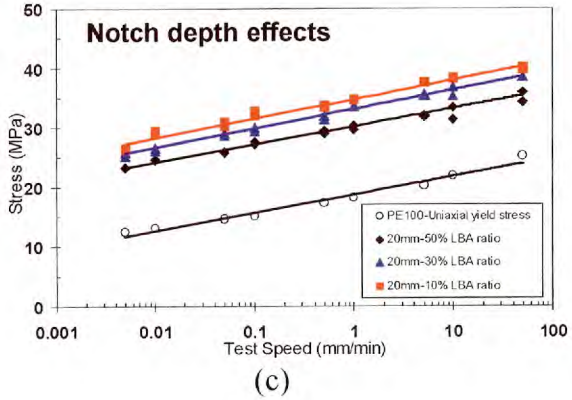

(c)

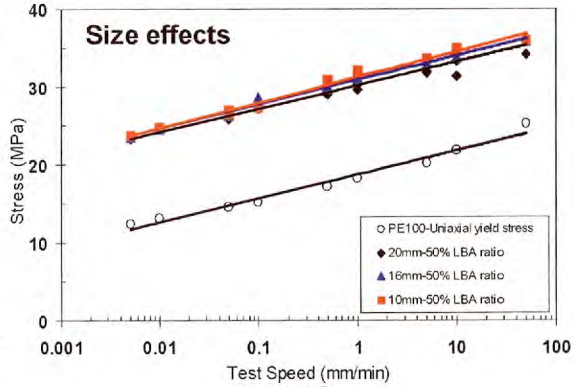

(f)

Figure 5.47 The effect of notch depth ((a) to (c)) and specimen thickness ((d) to (f)) on the σ_{peak} of PE100 at various loading speed.

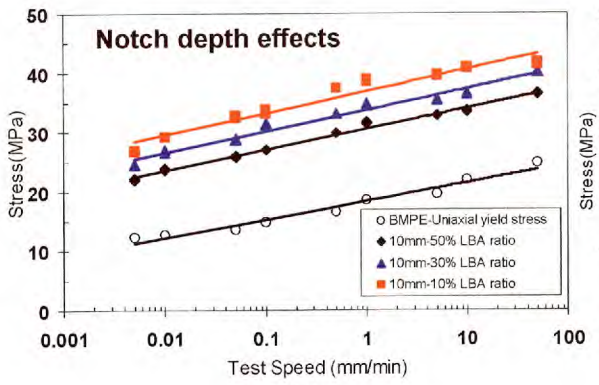

(a)

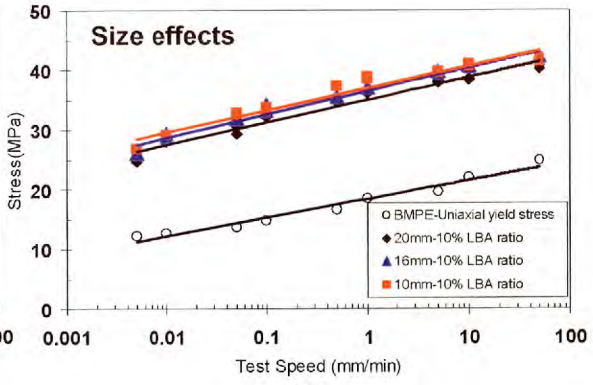

(d)

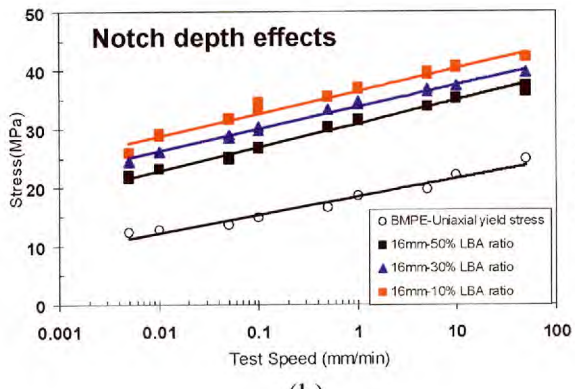

(b)

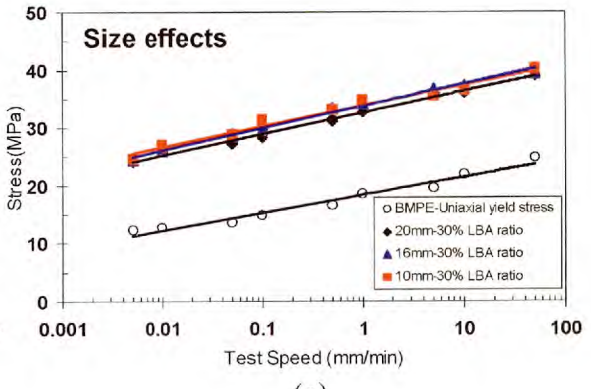

(e)

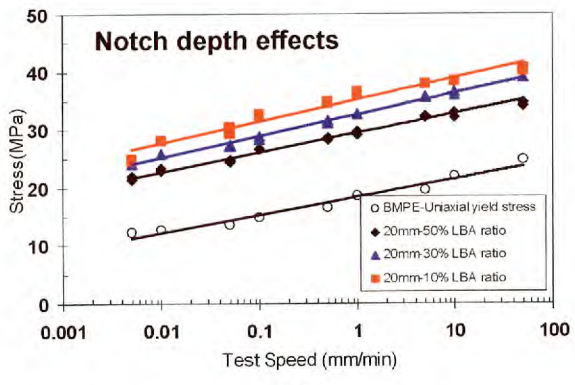

(c)

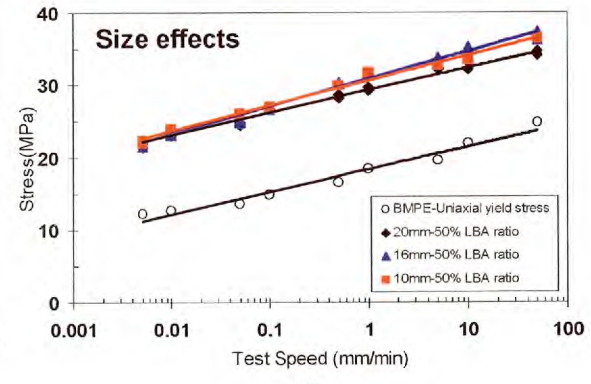

(f)

Figure 5.48 The effect of notch depth ((a) to (c)) and specimen thickness ((d) to (f)) on the σ_{peak} of BMPE at various loading speed.

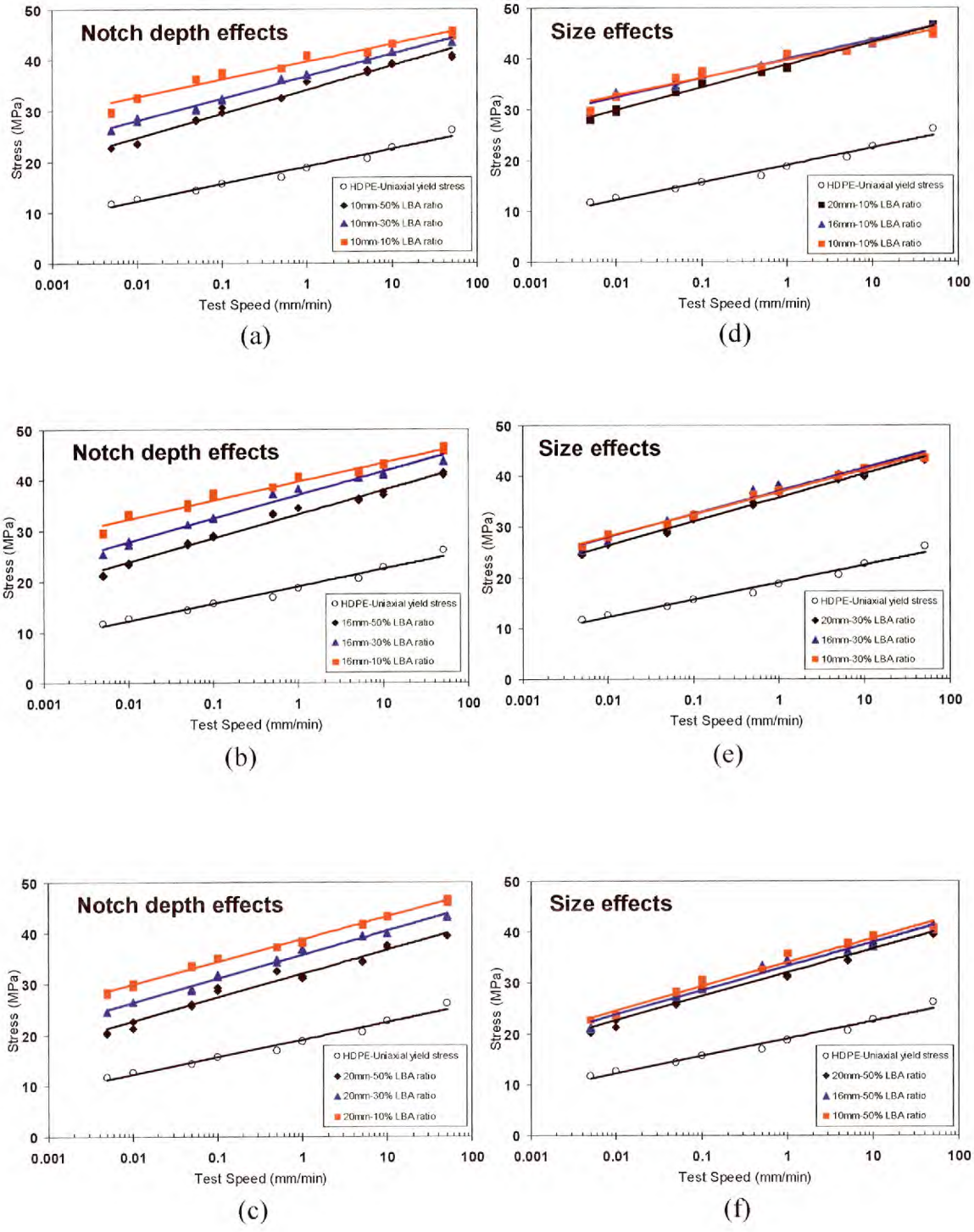

Figure 5.49 The effect of notch depth ((a) to (c)) and specimen thickness ((d) to (f)) on the σ_{peak} of HDPE at various loading speed.

As can be seen in Figure 5.46, the σ_{peak} and σ_y of PE80 increase with the logarithm of test speed and both showed an almost linear rise in the stress value. Generally, the steep gradients of stress which exist at a notch would produce a deformation constraint so that the σ_{peak} exceeds σ_y. Therefore, the greater the degree of triaxial stress developed in the notch vicinity, the higher is the constraint and hence the higher would be the tensile stress required to induce deformation. As revealed in Figures 5.46(a) to 5.46(c), the σ_{peak} data of 10% LBA ratio (deep notch specimen) is much higher than that of the σ_y (notch-free dumbbell sample). It can also be seen that the σ_{peak} data of 10% LBA ratio specimen occupies an upper stress band while the 50% LBA ratio specimen occupies a low stress band. The triaxial tensile stress state of the deep notch specimen (i.e. 10% LBA ratio) is obviously greater than that of the shallow notch specimens (30% and 50% LBA ratio) thereby giving rise to the higher σ_{peak} values. In contrast, the variation in the σ_{peak} values between specimens of different thickness is negligible as shown in Figures 5.46(d) to 5.46(f). This suggests that the σ_{peak} is a material property though a function of the constraint in that it is independent of the specimen size. The σ_{peak} trends in PE100 (Figure 5.47), BMPE (Figure 5.48) and HDPE (Figure 5.49) are similar to PE80.

5.7.2 Variation of separation at break with rate and constraint

Figures 5.50 to 5.53 show the variation of δ_{break} with test speed at various constraint conditions for PE80, PE100, BMPE and HDPE respectively. According to Figure 5.50(a) the δ_{break} values of 10% LBA ratio remain at an almost constant value across the speed range while the 30% and 50% LBA ratio δ_{break} data showed an upward trend with falling test speed. However, the rise in the δ_{break} values is more significant in the 50% LBA ratio. It appears that the effect of an increase in ligament length (i.e. LBA ratio) is to reduce the plastic flow constraint. As the constraint is decreased, the notch tip materials flow more readily to blunt the tip as was described earlier in §5.3.1. However, the 50% LBA ratio samples seem to show signs of a low speed (<0.05mm/min) plateau region. One might speculate that as the test speed is decreased further, a transition from ductile to brittle behaviour may emerge as the value of δ_{break} begins to fall. On the other hand, the high plastic flow constraints in the 10% LBA ratio specimen tend to promote

fracture (crazing) rather than flow, with the formation of homogeneous craze across the ligament throughout the speed range as was seen also by the fracture surfaces in Figure 5.23. At high loading rate (>10mm/min), the δ_{break} values from different LBA ratio converge. It is likely that the craze growth is severely restricted due to fibrillar melting as suggested by Leevers [1995]. Pandya *et. al.* [2003b] reported that crazing was suppressed as test rates were increased beyond 50 mm/min and showed a transition from ductile towards brittle behaviour. The δ_{break} trends in Figures 5.50(b) and 5.50(c) for specimen thickness of 16mm and 20mm respectively are similar to Figure 5.50(a).

Figures 5.50(d) to 5.50(f) show the variation of δ_{break} values with test speed between different sized specimens with identical LBA ratio. As can be seen from the figures, the difference in the δ_{break} values between the 10mm and 16mm specimens is not fully apparent whereas the 20mm specimens showed an upper bound δ_{break} values across the entire speed range. However, at a given test speed, the facture surfaces between the 20mm and the smaller specimens did not revealed a difference in the failure mechanisms as seen in Figure 5.31. In moving towards higher rates, the δ_{break} values of each thickness converge. This is consistent with the results reported in the proceeding section suggesting a thermal controlled material response.

The δ_{break} trends of PE100 in Figure 5.51 resemble with that seen in PE80. The notable difference being the raising trend in break separation values with falling test speed. The δ_{break} values of BMPE were also affected by the variation in notch depth but the response was slightly different. It can be seen from the Figures 5.52(a) to 5.52(c) that at low test rates the rise in the δ_{break} values with increasing LBA ratio is not as large as compared with PE80 or PE100, indicating a greater plastic flow constraint in BMPE. By comparison, HDPE showed a transition from ductile towards brittle behaviour at the low speed regimes. The transition point becomes more pronounced with 50% LBA ratio in which a marked drop in the δ_{break} values is seen in Figures 5.53(a) to 5.53(c). On the other hand, the effect of size appears to be less noticeable on the δ_{break} values, which is in good agreement with the results of §5.4.

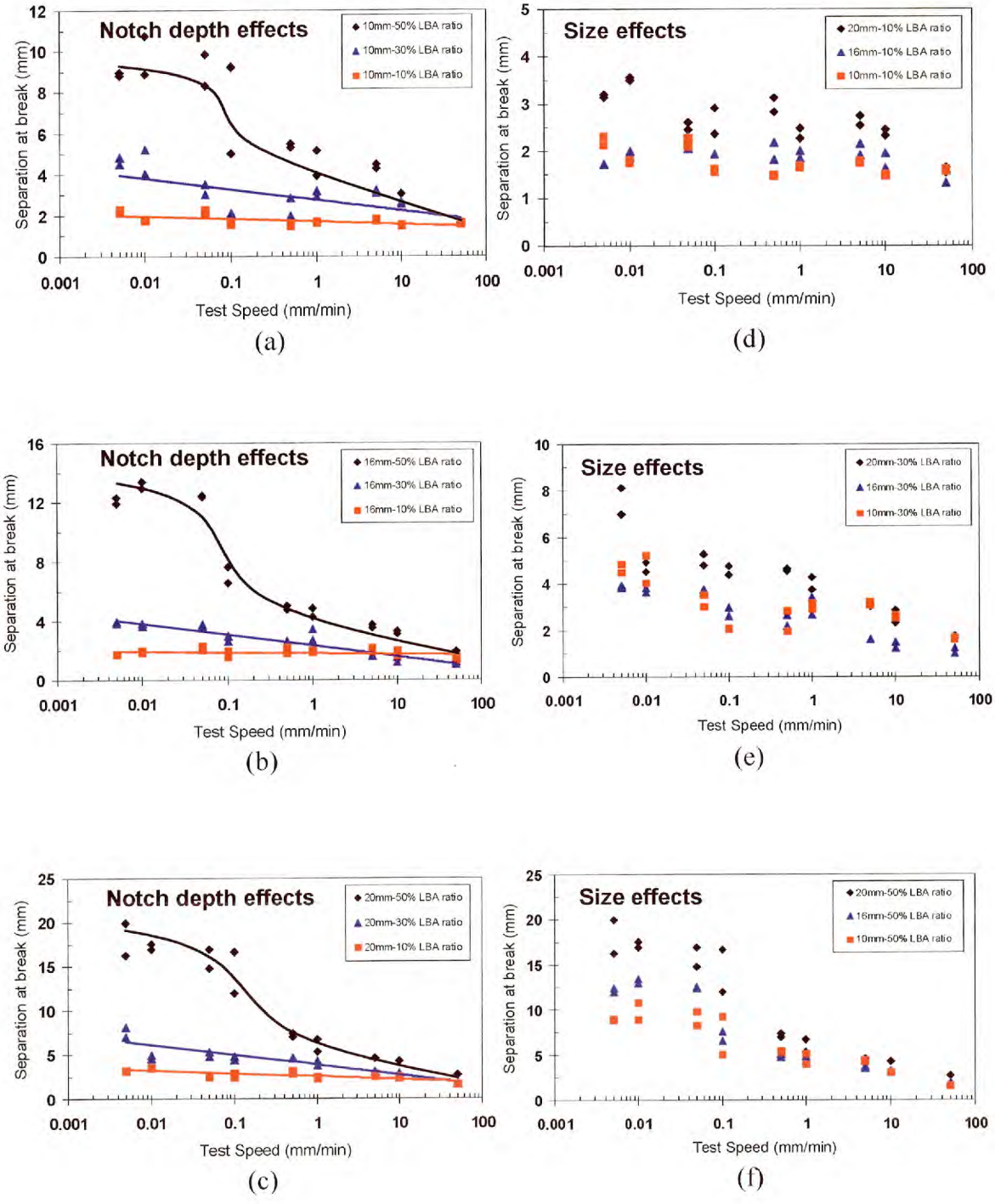

Figure 5.50 The effect of notch depth ((a) to (c)) and specimen thickness ((d) to (f)) on the δ_{break} of PE80 at various loading speed.

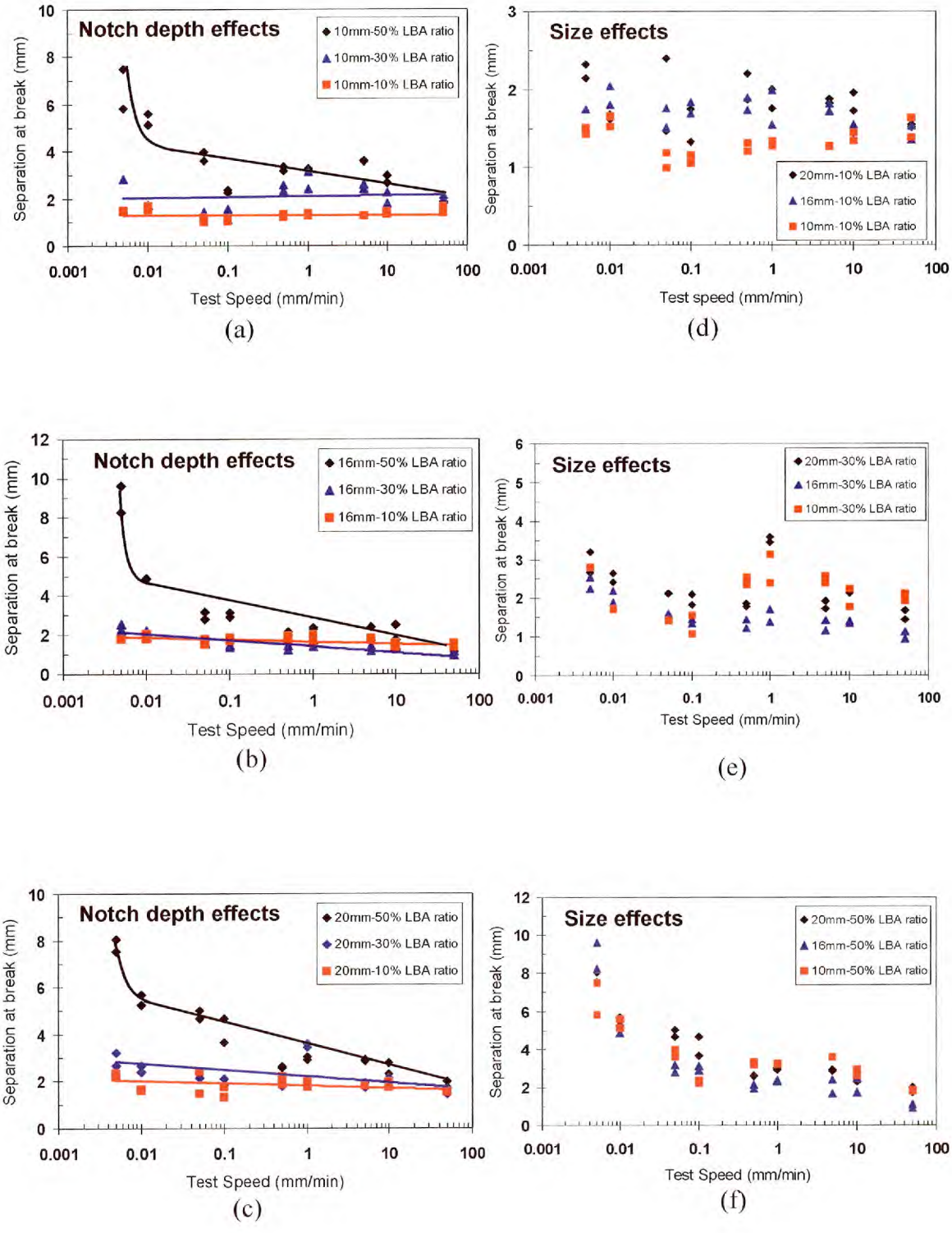

Figure 5.51 The effect of notch depth ((a) to (c)) and specimen thickness ((d) to (f)) on the δ_{break} of PE100 at various loading speed.

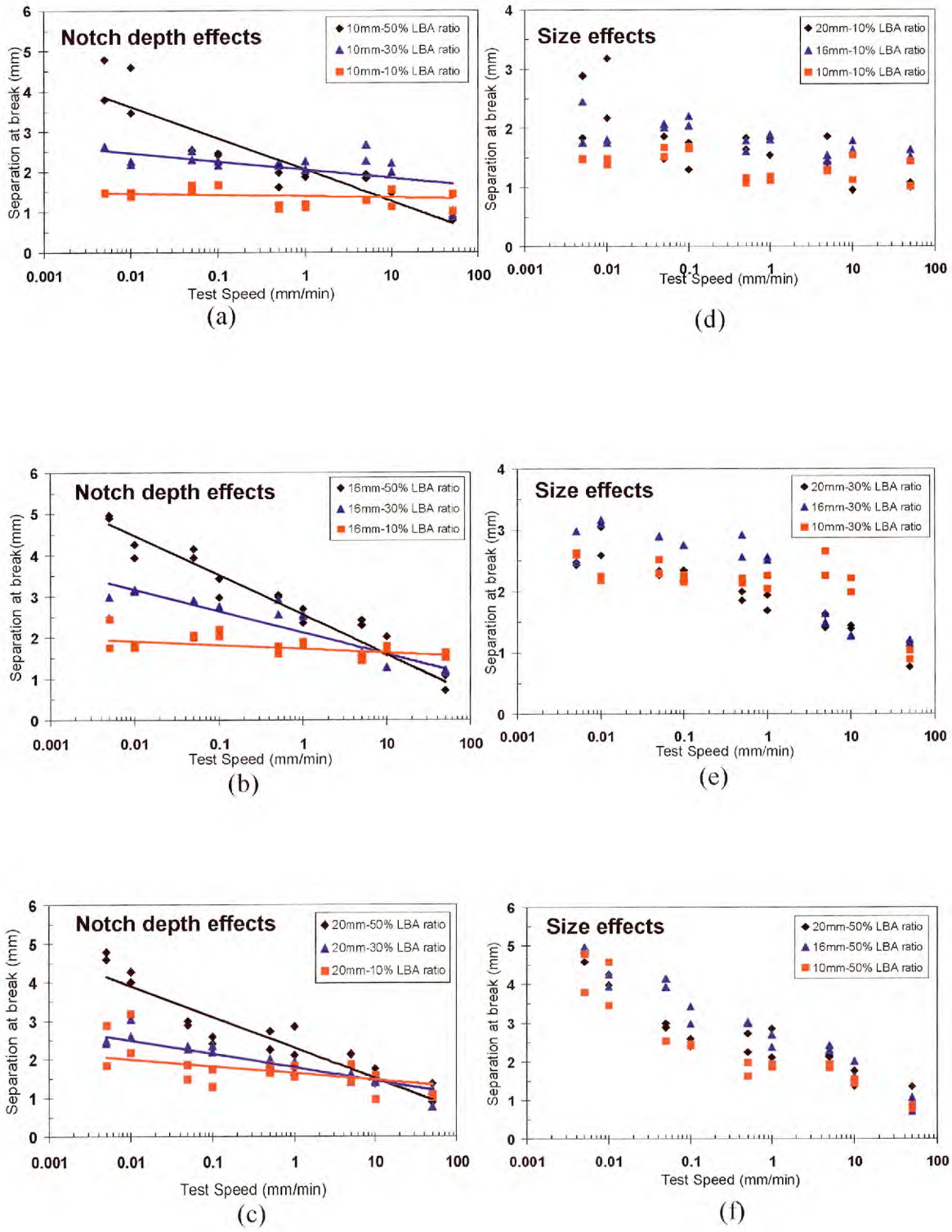

Figure 5.52 The effect of notch depth ((a) to (c)) and specimen thickness ((d) to (f)) on the δ_{break} of BMPE at various loading speed.

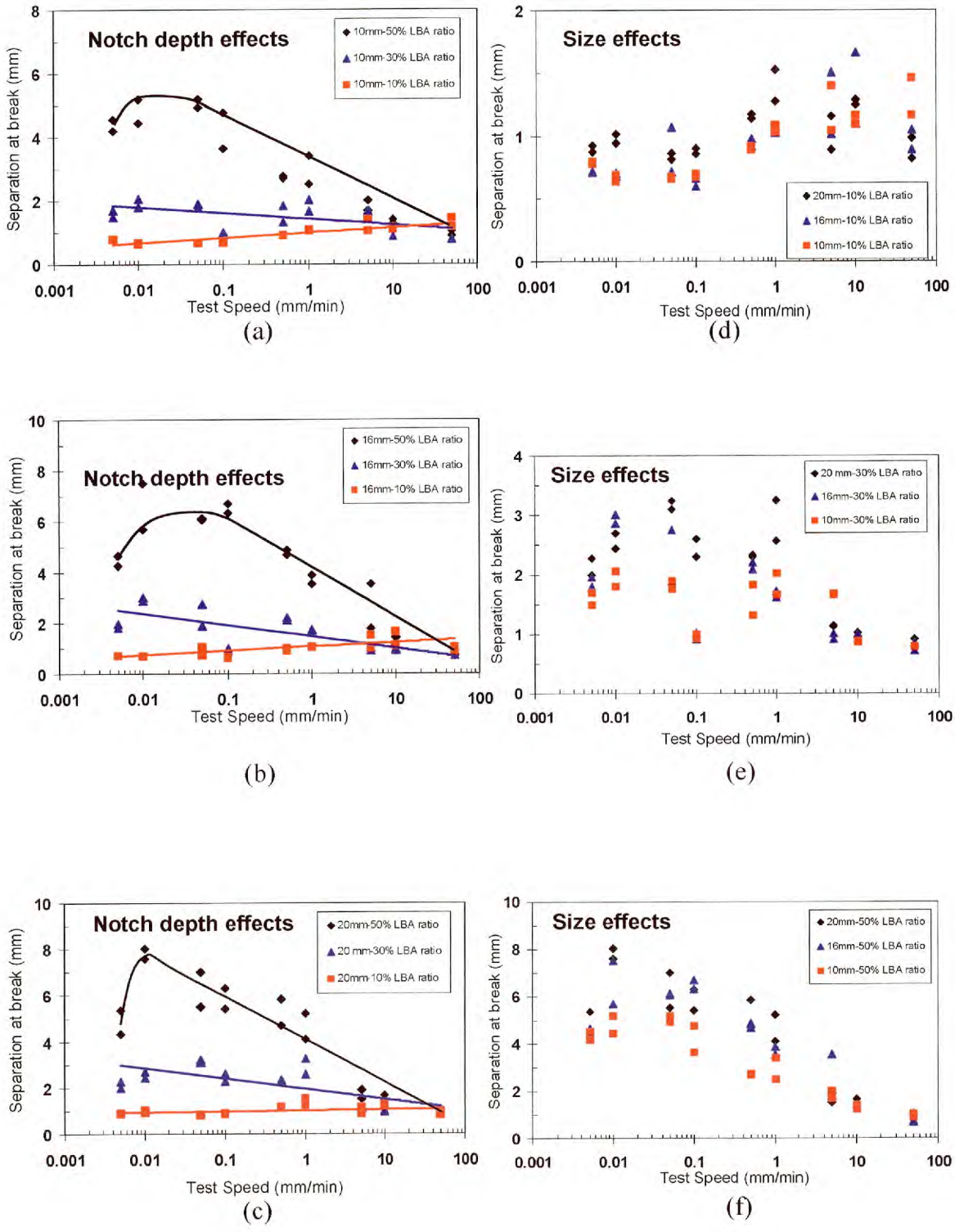

Figure 5.53 The effect of notch depth ((a) to (c)) and specimen thickness ((d) to (f)) on the δ_{break} of HDPE at various loading speed.

5.7.3 Variation of cohesive energy with rate and constraint

Figures 5.54 to 5.57 show the variation of Γ with test speed at various constraint conditions for PE80, PE100, BMPE and HDPE respectively.

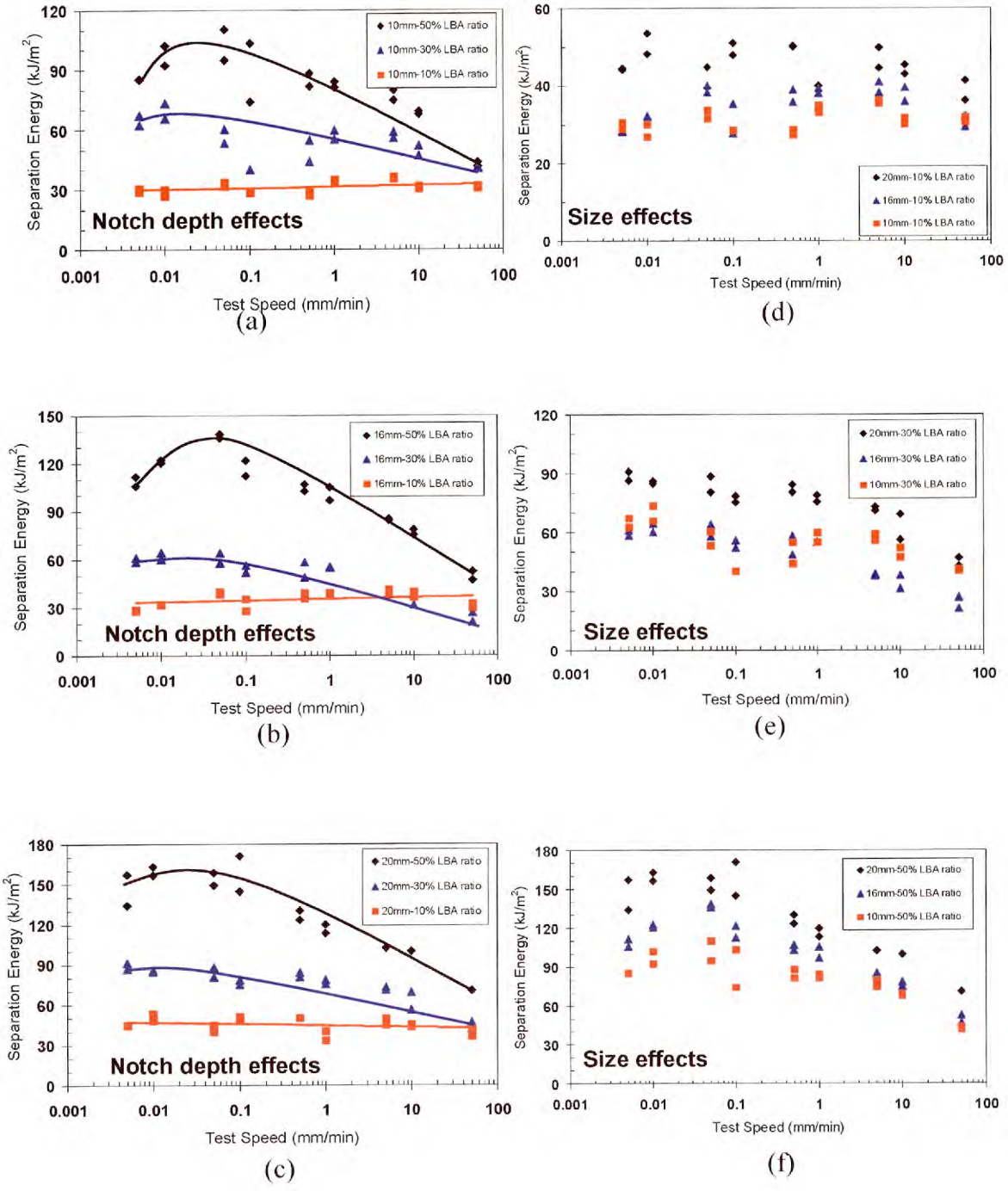

Figure 5.54 The effect of notch depth ((a) to (c)) and specimen thickness ((d) to (f)) on the Γof PE80 at various loading speed.

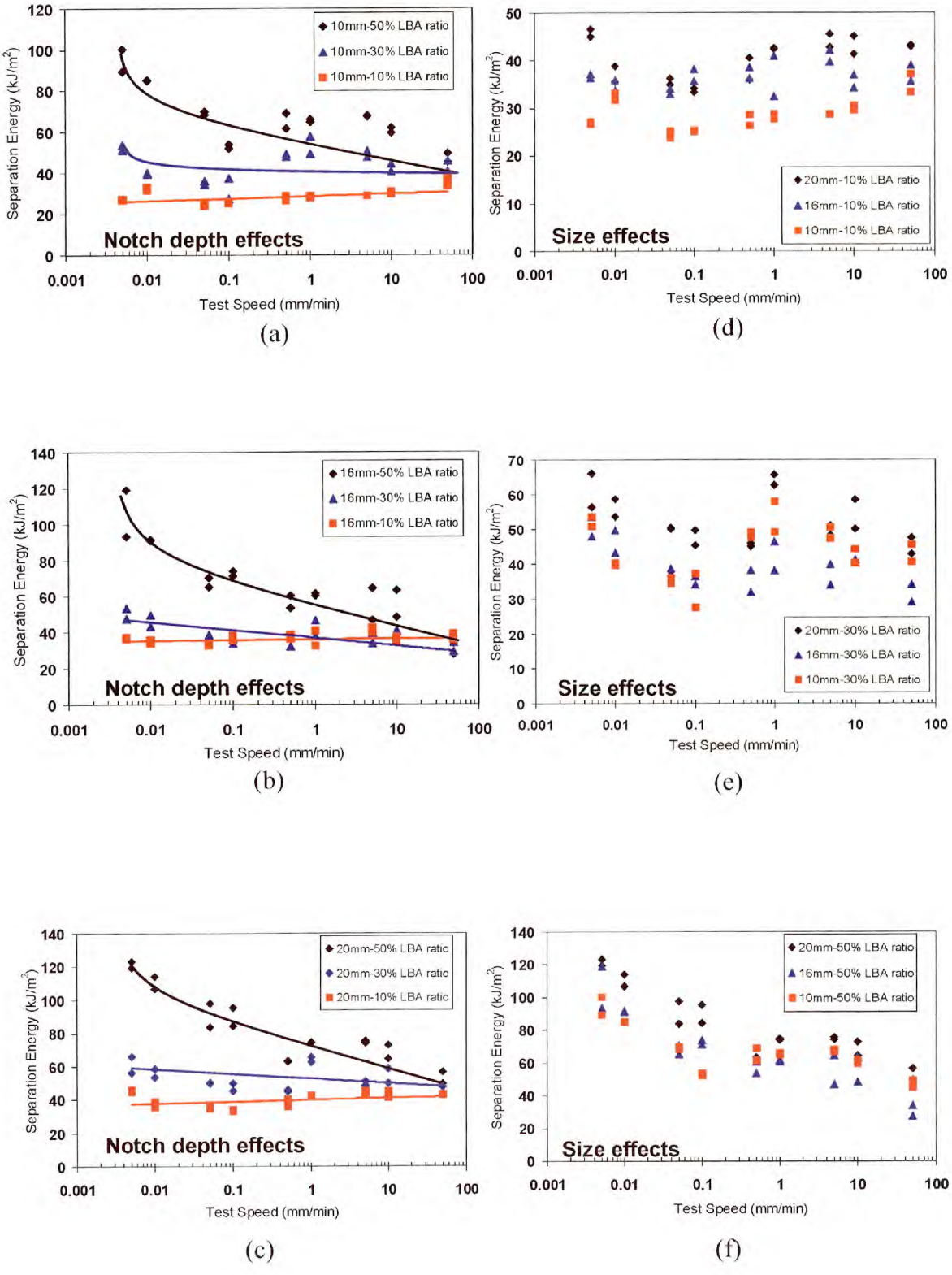

Figure 5.55 The effect of notch depth ((a) to (c)) and specimen thickness ((d) to (f)) on the Γof PE100 at various loading speed.

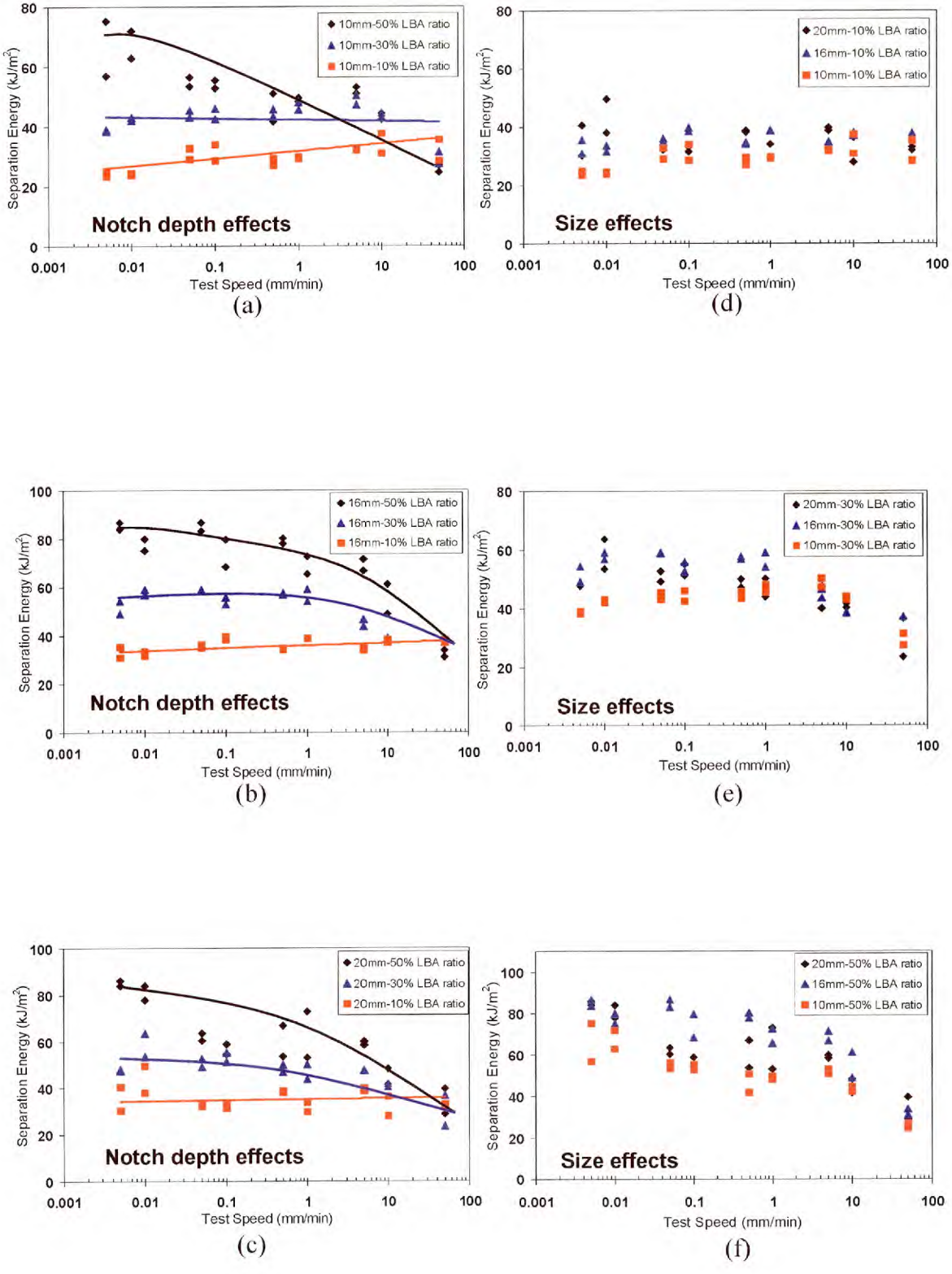

Figure 5.56 The effect of notch depth ((a) to (c)) and specimen thickness ((d) to (f)) on the Γof BMPE various loading speed.

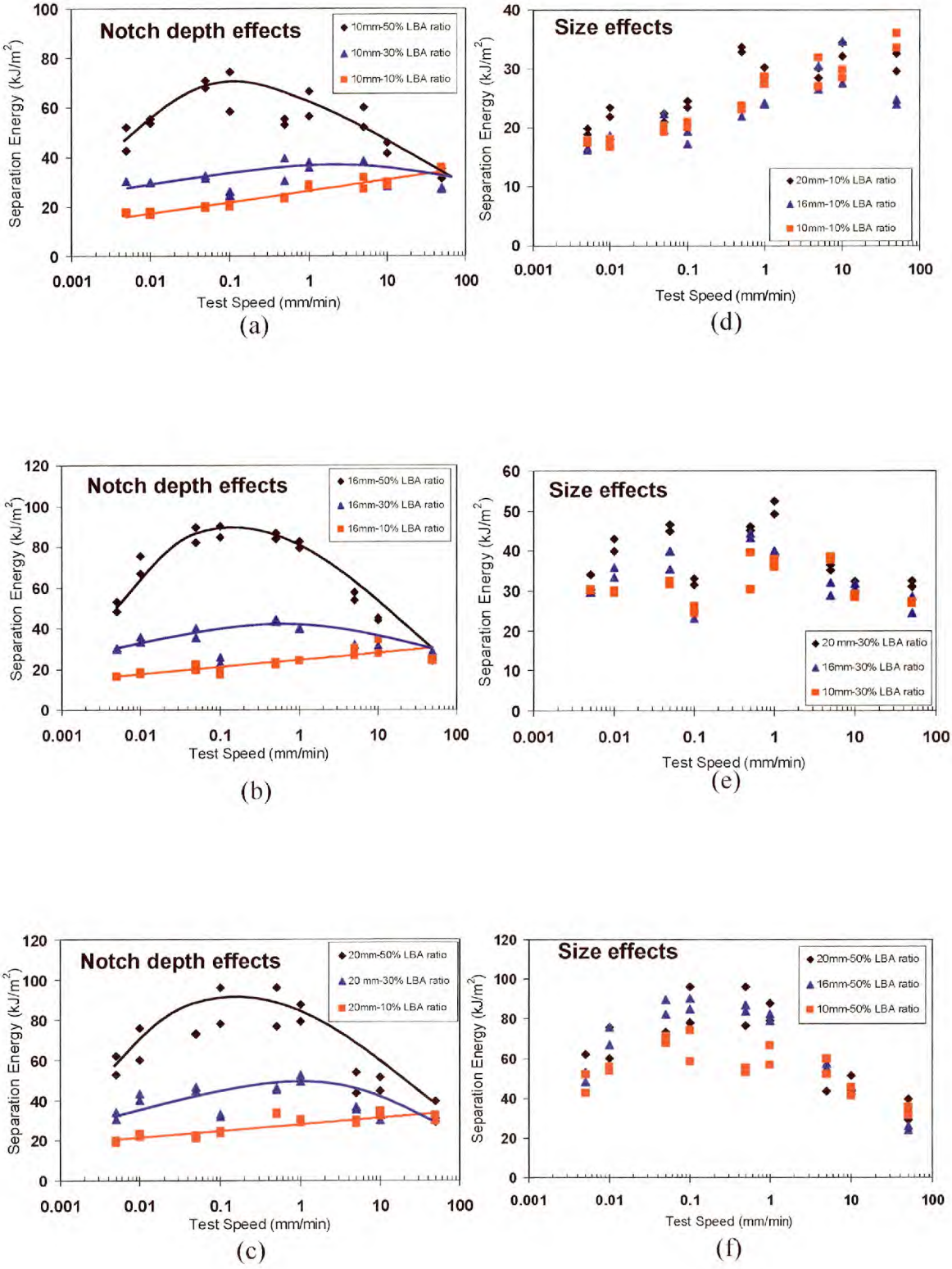

Figure 5.57 The effects of notch depth ((a) to (c)) and specimen thickness ((d) to (f)) on the Γof HDPE at various loading speed.

As can be seen from the Figure 5.54(a), the energy values of the 10mm specimen with a 50% LBA ratio occupies an upper energy band while the 10% LBA ratio occupies a lower energy band. By comparison, the energy value of the 30% LBA ratio lies between the bands. The energy values of the 10% LBA ratio remained at a relatively constant value between the speeds of 0.005 and 50 mm/min. In contrast, the energy for 50% LBA ratio increases due to the changing deformation behaviour as was seen by the fracture surfaces in Figure 5.23. The energy values are higher because of an increase in the δ_{break} values with falling test speed as seen in Figure 5.50(a) even though that the σ_{peak} values in Figure 5.46(a) showed a decline. In moving towards lower test rates (<0.05mm/min), the fall in energy values was due mainly to the drop in the δ_{break} values. On the contrary, the difference in energy value is small at high test rates. Similar energy trends were observed with 30% LBA ratio. It would appear that there is a transition in behaviour from being constraint dependent at the low speed regime to a rate dependent trend in the energy values at high rates. Increasing the specimen thickness to 16mm (Figure 5.54(b)) or 20mm (Figure 5.54(c)) produced similar energy trends.

Figures 5.54(d) to 5.54(f) compare the energy values between specimens of different thickness. On the whole, the 20mm specimen occupied an upper energy band while the smaller sized specimens filled up the lower bands. In each figure, the same energy trends were observed between the 20mm specimen and the smaller size specimen albeit a slight difference in the energy values. This is due to the fact that more material becomes available for the plastic deformation energy absorption as the thickness is increased. However, the mechanics of deformation between the specimens are the same. By comparing the energy trends of size effects against the notch depth effects (Figures 5.54(a) to 5.54(c)) it becomes apparent that the variations in energy values are driven mainly by the changes in the notch depth.

One important observation to emerge from the foregoing discussion is the dependency of the energy values on the δ_{break} values at low speed regime. Comparison of the energy trends (Figure 5.54) with the δ_{break} (Figure 5.50) and the σ_{peak} (Figure 5.46) behaviour shows that changes in energy are dominated by changes in the length of separation. As the energy transitions are driven primarily by changes in deformation mechanisms they do not necessary coincide with the stress. This is because any changes in the failure mechanism are not readily apparent from the slope of the stress – speed

data which appears not to change with speed. It may be noticed that the trends in the energy values best reflect the changing features of the fracture surfaces in Figure 5.23. Similarly, the energy trends of PE100 (Figure 5.55), BMPE (Figure 5.56) and HDPE (Figure 5.57) were mainly governed by the effect of notch depth which in turn depends on the δ_{break} trends rather than due to the effect of size.

5.8 Crack tip constraint

In the proceeding sections, the results showed that the degree of geometrical constraint (plastic flow) acting at the crack /notch tip increases with an increase in notch depth (a decrease in LBA ratio). It is clear from the result presented in Figures 5.46 to 5.49 that the high geometric constraint found in the 10% LBA ratio specimen (for a given thickness) elevated the degree of triaxial stress developed in the notch vicinity, causing yielding to occur at stress levels (i.e. σ_{peak}) exceeding the uniaxial yield stress of the material. This is because it is more difficult to spread the yielded zone in the presence of triaxial stresses. On the other hand, the σ_{peak} values fall with decreasing notch depth signifying the reduction in the geometric constraint. One of the most noticeable features with the notch depth effects is to raise the δ_{break} values of the materials (Figures 5.50 to 5.53). The increase in the δ_{break} values is due to a greater degree of crack tip ductility which depends upon the size (volume) of the notch tip plastic zone, which in turn depends upon the geometric constraint. It is known that the notch tip plastic zone size increases with a decrease in constraint, thereby leading to a greater degree of crack tip ductility. This was confirmed by the 50% LBA ratio sectioned specimen which shows a larger whitened area surrounding the tips than those of the deep notched specimen. For this reason, the fracture ductility increases (Figures 5.54 to 5.57) as the crack tip is readily blunted resulting in the increase of the δ_{break} values on the macroscopic scale. As the state of stress acting at the crack tip determines the geometric constraint, it is possible to quantify the notch tip constraint level. Accordingly, a parameter called the crack tip constraint factor, M can be defined to describe the elevation of the applied stress at yield by an equation of the form:

$$M = \frac{\sigma_{peak}}{\sigma_y} \qquad (5.1)$$

When M =1 it would represent the plane stress case. A limiting M value, on the other hand, would denote a maximum constraint condition and represents a lower bound to the material toughness.

Figures 5.58 to 5.61 show the computed M against test speed for PE80, PE100, BMPE and HDPE respectively. One trend common to all the materials is the decrease in the M values as the test speed increases. Comparison of the M values between specimens of different LBA ratio (Figures 5.58(a) to 5.58(c), 5.59(a) to 5.59(c), 5.60(a) to 5.60(c), 5.61(a) to 5.61(c)) shows that the constraint factor is the highest for specimens with the 10% LBA ratio while constraint is the lowest for specimens with a 50% LBA ratio. Therefore, as M increases (at the expense of the plastic zone size) with decreasing rate, one might expect a highly constrained failure normally associated with cavitation and voiding. The analyses performed in Figure 5.36 confirmed this point showing that the fracture surfaces consisted of voids and fibrils in each grade. On the other hand, a low M at low rates would be likely linked to a ductile fracture mode owing to a much larger notch tip plastic zone size which subsequently blunted the tip. These effects were accompanied by an increase in fracture toughness. The phenomenon has been described respectively in the Figures 5.2, 5.8, 5.13 and 5.20 for each grade. At high loading rates, the M values from different conditions converge. It would appear that the differences in deformation mechanisms observed due to different M values at low speeds become increasingly indistinguishable at high rates as was seen also by the fracture surfaces in Figures 5.23 to 5.26 for PE80, PE100, BMPE and HDPE respectively. By comparison the variation of M between specimens of different thickness is not significant (Figures 5.58(d) to 5.58(f), 5.59(d) to 5.59(f), 5.60(d) to 5.60(f), 5.61(d) to 5.61(f)), suggesting that M could be independent of the thickness effects.

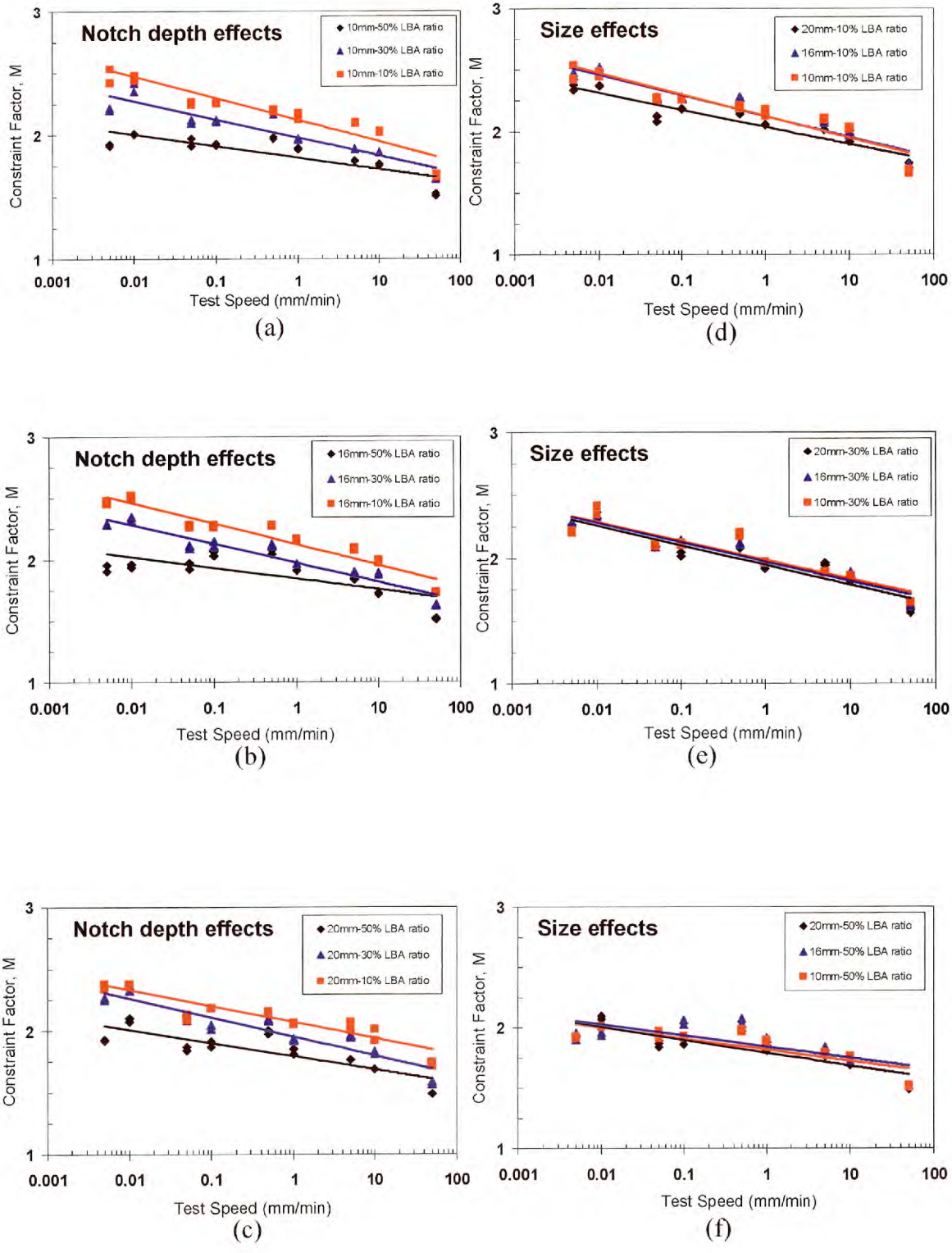

Figure 5.58 Variation of M with test speed of PE80. The effect of notch depth (a) to (c) and specimen thickness (d) to (f) on the constraints.

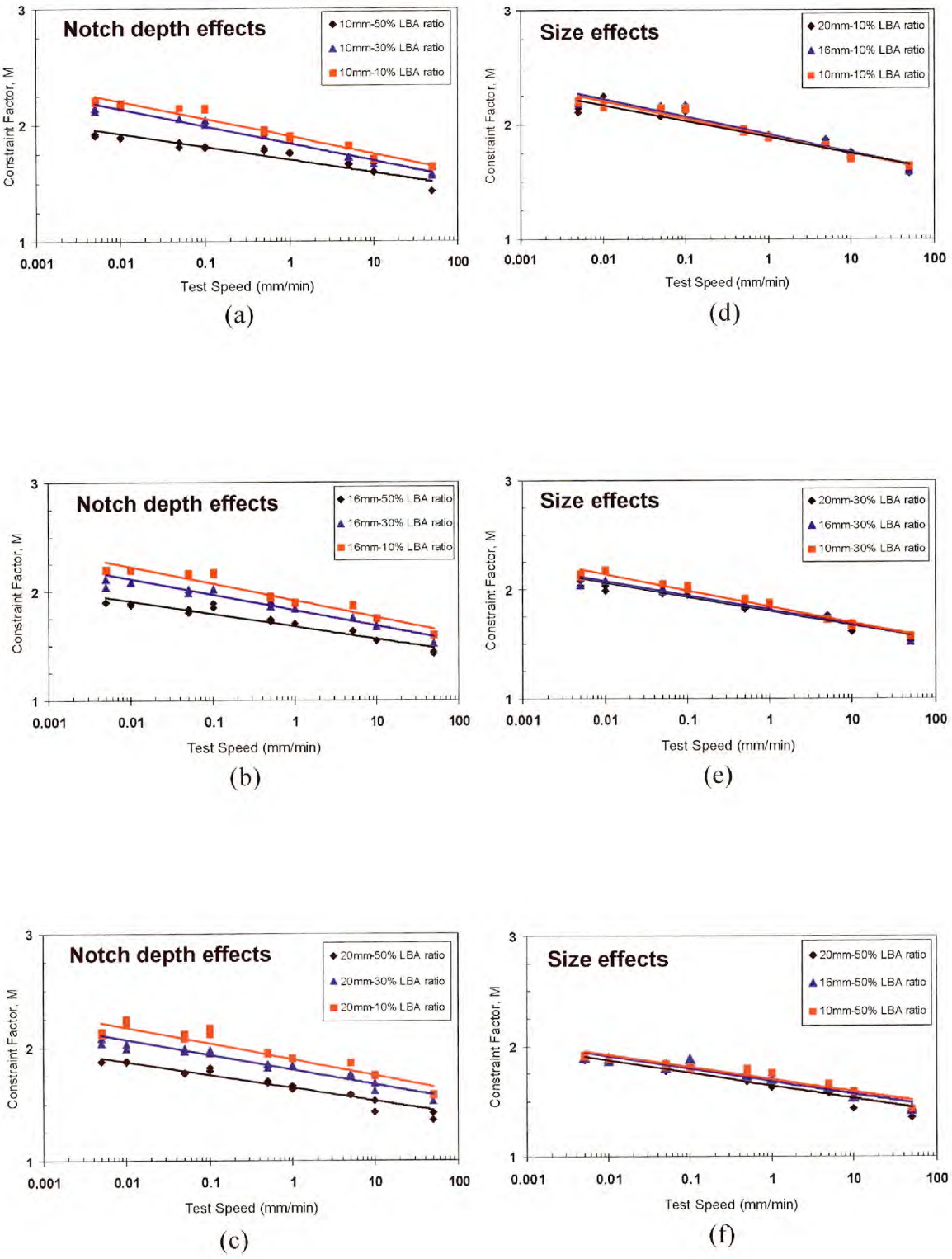

Figure 5.59 Variation of M with test speed of PE100. The effect of notch depth (a) to (c) and specimen thickness (d) to (f) on the constraints.

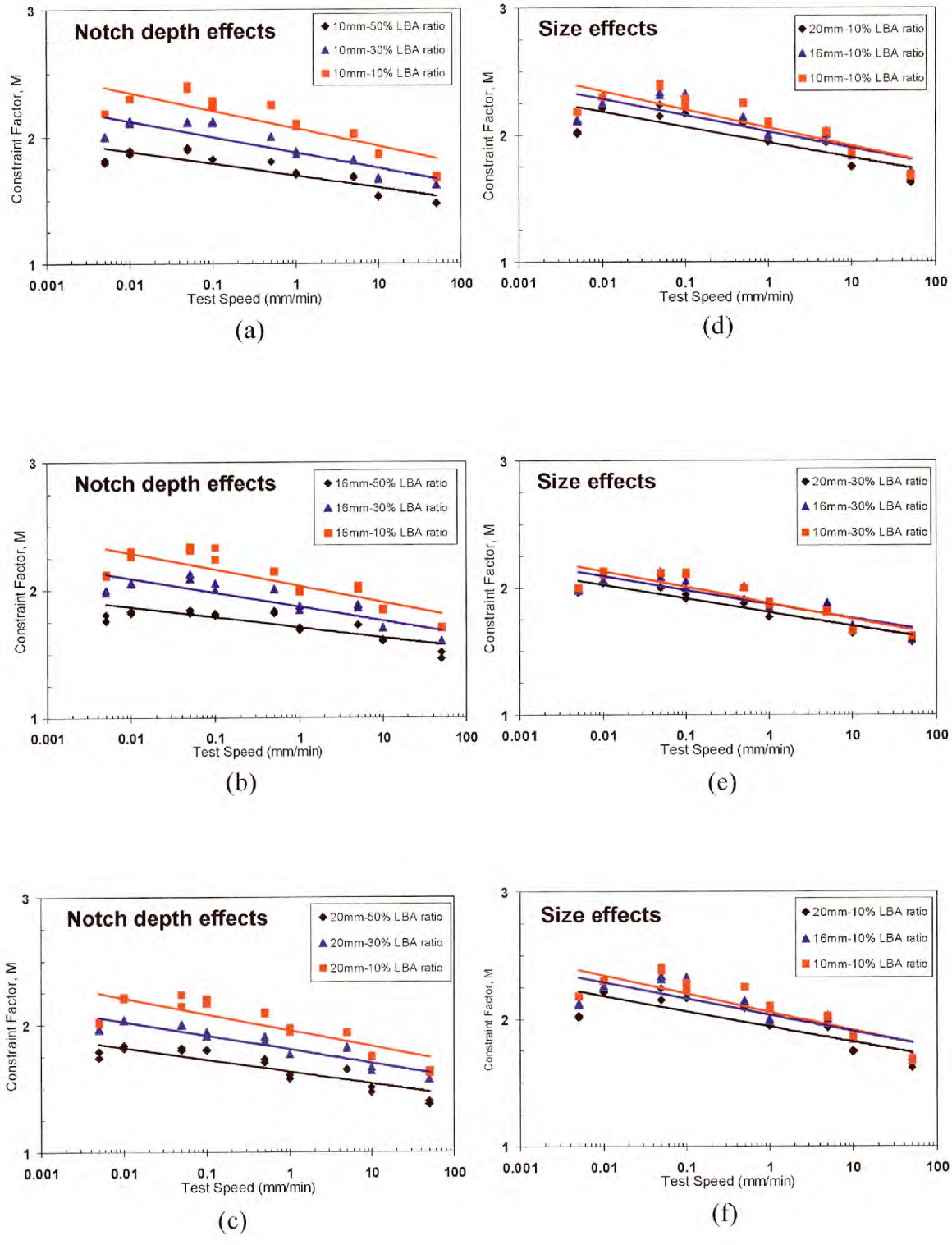

Figure 5.60 Variation of M with test speed of BMPE. The effect of notch depth (a) to (c) and specimen thickness (d) to (f) on the constraints.

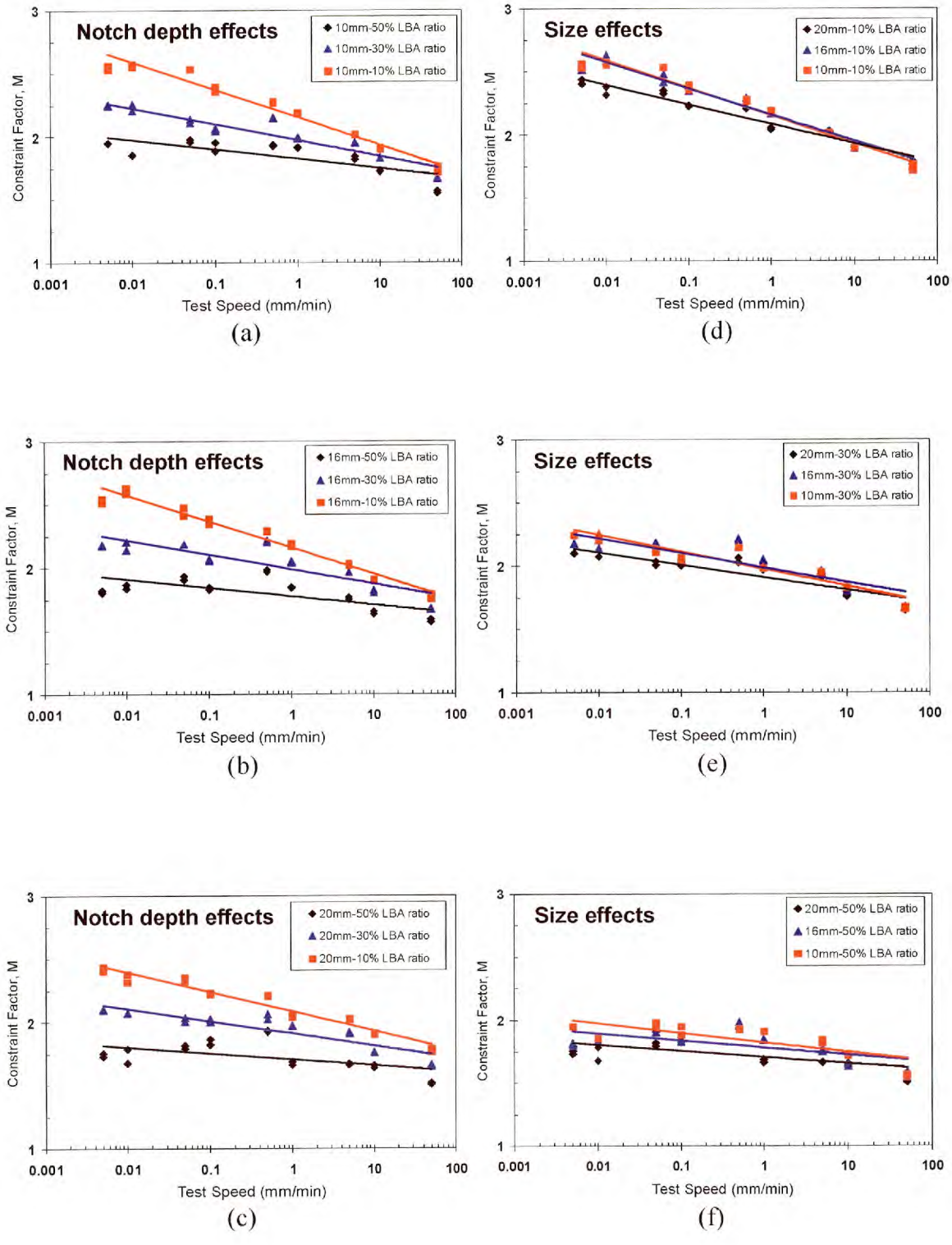

Figure 5.61 Variation of M with test speed of HDPE. The effect of notch depth (a) to (c) and specimen thickness (d) to (f) on the constraints.

5.9 Conclusions

The deformation mechanisms of four different grades of polyethylene were compared between the test speeds of 0.005 and 50 mm/min at various constraint conditions using a circumferentially notched tensile specimen. A wide range of experimental data of the rate and constraint effects on the fracture behaviour was analysed. The onset and subsequent evolution of the damage (craze) was found to be sensitive to constraint effects, in addition to rates. In particular, the effect of notch depth was found to exert a greater influence on the material response than through the thickness effects. Kirk *et. al.* [1993] also reported the greater effect of crack depth than that of the specimen size for a metal alloy. It was shown that the deeper the notch, the greater was the notch tip (plastic) constraint to promote constrained brittle failure where cavitation was preferred. As the notch tip constraint was relieved through a larger ligament diameter, the crack tip ductility was increased to invoke the blunting process, which in turn increased the δ_{break} and Γ values. It is this mechanism (crack tip blunting) which initiated the ductile failure mode. On the contrary, the constraint between specimens of different thickness was found to be similar. Furthermore, the stress (σ_{peak}) required to initiate the damage process remained constant with size, suggesting that σ_{peak} is a property of the material though a function of M. However, the effect of constraint became less noticeable at high test speeds where the fracture characteristics appeared identical (by process of voids nucleation, growth and coalescence), suggesting a dominance of effects of rate. Under conditions of decreasing extension rate, it was possible to differentiate the material response at different constraint conditions as the deformation behaviour was unique. On this basis, the study was able to identify the different damage and failure process associated with each grade at the low speed regime. The deformation characteristics of each grade is summarised as follows.

PE80 – Under conditions of high constraint, a multiple craze structure was developed. The fracture proceeded mainly via the deformation of the primary craze through void coalescence while the secondary crazes appeared redundant. At intermediate constraint, the secondary crazes were found to play a contributory part in the overall blunting process. As constraint was reduced further, there was a transition from one ductile mechanism (multiple crazing) to another ductile mechanism (shear

yielding). Hence, the fracture energy was raised significantly, demonstrating a high resistance to SCG.

PE100 – The damaged ligament at high constraint conditions showed the formation of a highly fibrillated craze structure where void nucleation was absent, suggesting that the failure mechanism is likely through fibril creep. By lowering the constraint, the degree of crack tip blunting increased via multiple crazing. However, there were comparably fewer secondary crazes in the structure than those seen in PE80 but the crazes were thicker. PE100 also exhibited large macroscopic plastic flow at the lowest constraint examined but through different mechanisms. The deformation behaviour was found to consist of both shearing and crazing in which the shear mechanisms prevailed on the surface while crazing was active on the interior.

BMPE –The main feature of the damage associated with this grade was the formation of multiple crazes. The deformation process occurring under conditions of high constraint is similar to those reported for PE80. However, the rate of void growth appears to be higher in this material. As the constraint was reduced, multiple crazing continued to blunt the tip but it was also accompanied by the formation of large void. At the lowest constraint, the tip material was breached after it underwent a significant amount of tip blunting. However, the crack tip ductility is very much lower than those of the PE80 or PE100.

HDPE – The main feature of the damage associated with this grade was the formation of a single craze structure. At high constraint conditions, the material showed little post-peak ductility due to diffuse voiding. As the constraint was lowered, HDPE did not display any sign of tip blunting. It is possible that the extent of plasticity surrounding the crack tip is very much lower than those of the copolymers. The damage once initiated often led to the growth of radial cracks. Hence, the fracture behaviour may be regarded as unstable during slow crack growth as it could lead to a brittle mode of fracture.

Having analysed the various deformation and failure mechanisms, it is now possible to review the relationship between the mechanical properties and the microstructure, which is the topic of discussion for the next chapter.

Chapter 6
The structure-property analysis of polyethylene

6.1 Introduction

In addressing the long term performance and reliability of the pipes, it is important to identify the key variables central to the SCG performance. As can be seen in the Figure 6.1, a large number of parameters can influence the fracture behaviour of the material.

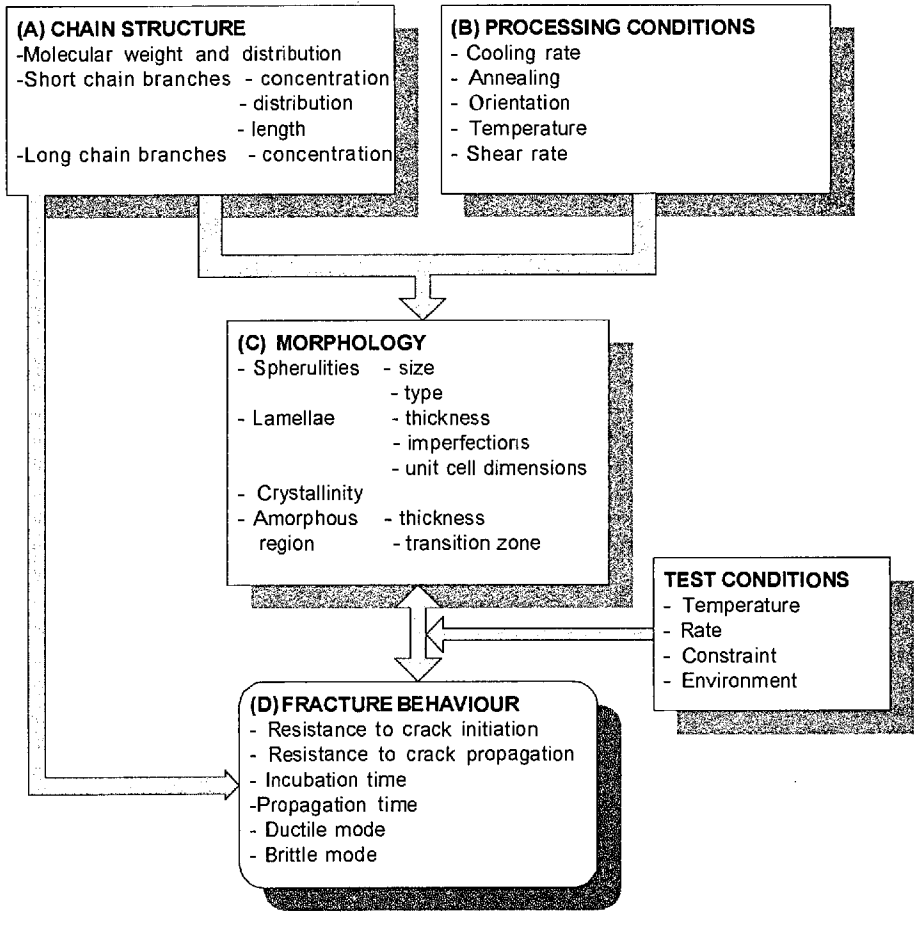

Figure 6.1 Overview of parameters affecting the fracture behaviour of polymers. (*from* Egan and Delatycki [1995]).

Clearly, it is not practical to include all these parameters in a single study. However, according to the Figure 6.1 the polymer characteristics such as the chain structure can affect the material response directly. This is especially true in respect of the SCG performance. This chapter will concentrate on the effect of the chain structure, in addition to the deformation rate and specimen geometry, on the mechanical properties and the linkage between them governing the SCG performance will be discussed.

6.2 Structure-property analysis at low rates

6.2.1 Damage comparison at high constraint conditions

Figure 6.2 compares the craze structure of PE80, PE100, BMPE and HDPE at low test rates under conditions of high notch tip constraint.

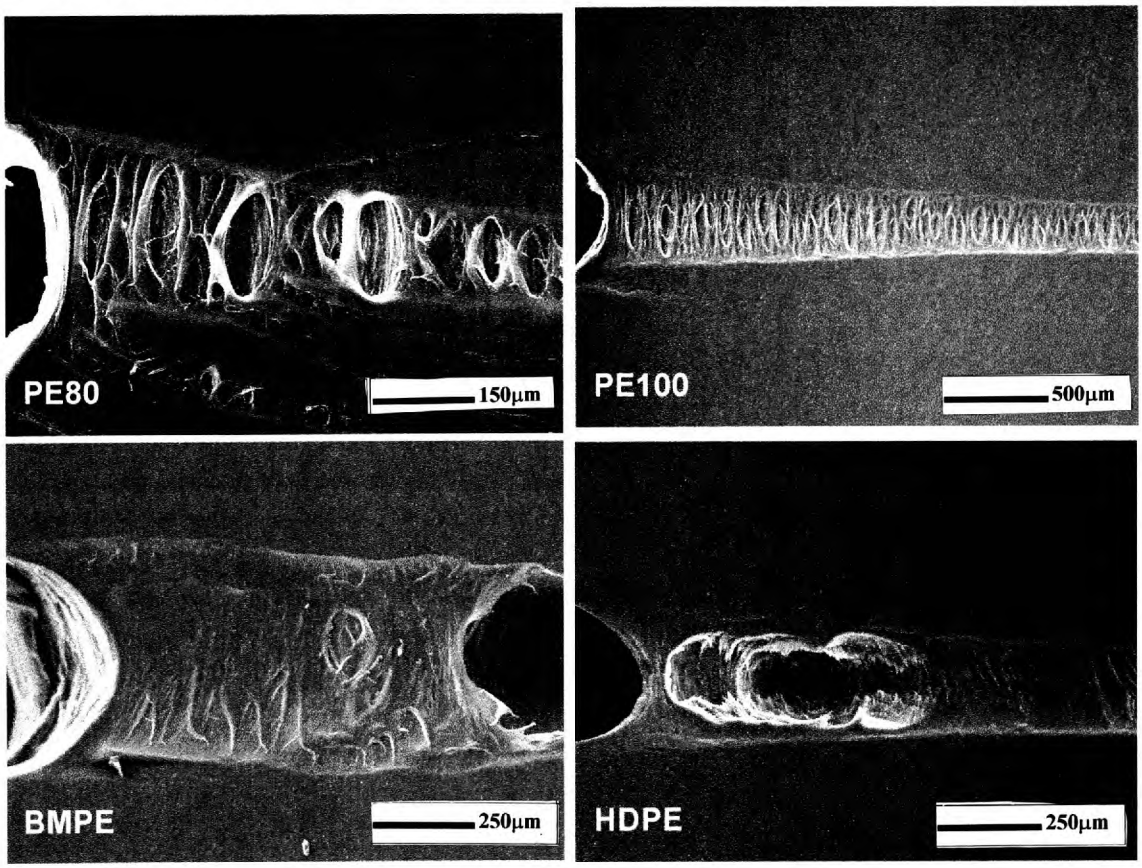

Figure 6.2 Comparison of the damage structure between the different grades at low rates and high constraint conditions.

It can be seen that a multiple craze structure has formed in PE80 in which the thickness of the secondary crazes are smaller than the primary craze. There is also evidence of multiple crazing in PE100 and BMPE but there are fewer secondary crazes. In PE100 the structure showed a highly fibrillated craze. By comparison, the extent to which the fibrils can be drawn in BMPE is lower than that of PE100. The breakdown of the fibril eventually leads to void formation. In contrast, the craze structure of HDPE showed widespread voiding. The onset of fibrillar creep may have taken place much earlier than that of the copolymers. This can be seen in the thinning of fibrils and the failure at the midribs. However, little information is available to offer an explanation on the formation of multiple crazing. Nevertheless, it would appear that the low density in PE80 encourages the nucleation of multiple crazes due to a high proportion of free volume, which has conventionally been attributed to low crystallinity, as opposed to the high density HDPE where a multiple craze structure is absent.

In PE80 the fibrils showed a greater resistance to fracture than that of BMPE or HDPE. This may be explained by considering the rate of disentanglement of the materials. In the absence of short chain branch (SCB) content, the high molecular weight HDPE is likely to depend on the long molecular chains to produce the network of entanglement. Moreover, the longer molecule is likely to increase the concentration of inter-crystalline links and hence increases the overall entanglement density in the amorphous domain. Although unknotting of entanglements may becomes difficult but under SCG conditions any positive effect may be overridden by the ease of chain sliding through the crystalline regions of the fibrils because of the relatively smooth chain. One manifestation of this is the higher rate of void growth. Although the breadth of the molecular weight distribution (MWD) is similar in HDPE and BMPE (see Figure 3.2) in BMPE it has a higher SCB content of 1.5 branches per 1000 C atoms. For this reason, it appears that SCB has a beneficial effect of stabilising the craze structure where the fibrils showed a greater capacity to draw prior to failure. From this viewpoint, it is obvious that the high SCB content in PE80, which has 4.5 branches per 1000 C atoms, would provide a good impediment to the disentanglement process that occurs after the fibrils reached their natural draw ratio. Even though PE80 has a lower molecular weight, M_w and contains a smaller fraction of high molecular weight material (see Table

3.1), any negative effect may be overcome by the advantage of having a high SCB content. This comparison thus identifies the importance of the existence of a high SCB content in improving the long term resistance to SCG.

The highly fibrillated craze and the absence of voids in PE100 seem to suggest that the material deforms via a combination of fibrillar creep and surface drawing mechanisms. There is also evidence of cross-tie fibrils thereby giving the craze some lateral load bearing capacity as seen in Figure 6.3. The surface draw mechanism is probably missing in HDPE. The micrograph also conveys some information about the strength of the fibrils in PE100 in relation to PE80. First, the fibrils showed constant thickness throughout the length, indicating that fresh material is constantly being drawn into the fibrils thereby maintaining the draw ratio, λ as widening continues. Second, the absence of fibrils thinning might imply that the rate of fibrillar creep is low. In PE100 the SCB content is 2.5 branches per 1000 C atoms which is nearly half of those in PE80. Despite the lower SCB content, PE100 appears to have a much larger λ which is consistent with the results of O'Connell *et. al.* [2003]. Normally, as branch concentration increases the natural draw ratio decreases but also interferes with the disentanglement. On the other hand, an increase in M_w would increase chain entanglement and thus reduce the creep (O'Connell *et. al.* [2003]). Because of this, PE100 is likely to show a greater resistance against creep than PE80 in which the M_w is almost half of PE100. Further evidence of this is provided by the MWD of PE100 (Figure 3.2) in which the high molecular weight fraction is greater than that of PE80. As a result, the capacity of the molecular entanglement network to deform is likely to increase. On a macroscopic scale, the high deformation capacity is captured by an increase in the separation distance at low test rates as seen in Figure 5.51. On the whole, PE100 is likely to have a combined effect of extending the period of growth during craze widening as well as hindering the disentanglement processes that occur after the fibrils reach their natural draw ratio. The first effect could be attributed to the high value of λ while the optimisation of molecular weight chains and short chain branches accounted for the improved disentanglement resistance. These results are in substantial agreement with those of Pandya [2000] and Pandya and Williams [2000a,b].

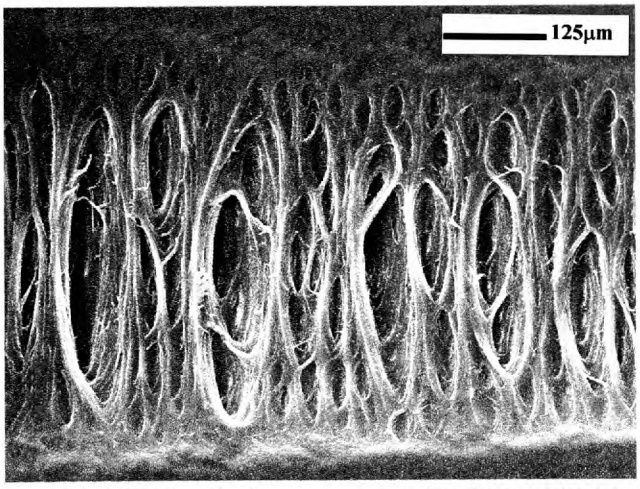

Figure 6.3 The detailed structure of fibrils in PE100.

6.2.2 Damage comparison at low constraint conditions

Figure 6.4 compares the damage structure of PE80, PE100, BMPE and HDPE at low test rates under conditions of low notch tip constraint. For all materials, the damage was initiated in the craze.

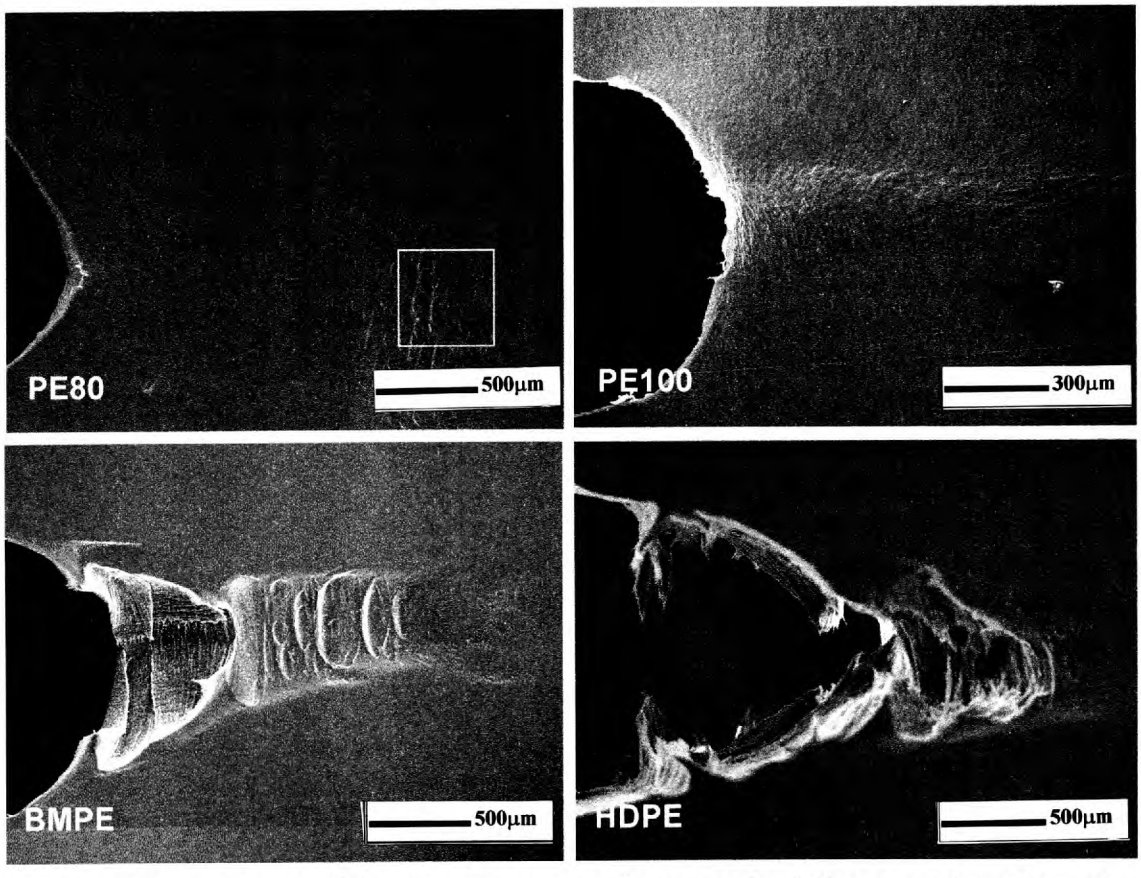

Figure 6.4 Comparison of the damage structure between the different grades at low rates and low constraint conditions.

As the crack tip constraint is reduced, there is a competition between shear deformation zones and craze formation in the pipe materials. It is therefore possible that the shear bands may have nucleated from the tips of the (initial) craze due to the local stress concentration. As can be seen from the micrograph in Figure 6.4, the notch tip of PE80 is severely blunted which is caused by the localised shear flow. Far from the tip, some voids have nucleated together with the formation of few strands of fibril as seen in Figure 6.5. Similarly, PE100 is characterised by the large macroscopic shear flow of the ligament. The difference being the coexistence of craze-like features and shear deformation bands. The interaction between these two mechanisms caused excessive blunting of the tip. Given that the structural properties of the materials were not varied the transition from crazing to shear therefore appears to depend on the state of the constraint. Kramer and Berger [1990] provided a possible explanation for the craze-shear transition. According to the study, the transition from crazing to shear transformation occurs when the shear yield point is less than the stress for crazing. If the σ_{max} is taken as the measure of the stress to initiate damage then σ_{max} obtained at a high constraint condition is likely to represent the crazing stress since the damage is characterised by the formation of crazes (Figure 6.2). It was shown that σ_{max} decreases as the constraint was lowered (Figures 5.46 to 5.49). Therefore, it seems that the lower triaxial stress state may have favoured shear yielding by lowering the damage stress (σ_{max}) point below the crazing stress. As a result, shear yielding becomes increasingly competitive with crazing as the constraint is reduced.

By comparison, the tip structure of BMPE in Figure 6.4 revealed a highly stretched texture, which is followed by a structure seemingly filled with voids. In HDPE the crack has breached the tip wall, leading to a craze-crack growth behaviour to emerge. It appears that the difference in the fracture behaviour compared with that observed in the high constraint situation is due to the effect of constraint but the difference in the material response primarily depends on the molecular characteristics as seen by the fracture surface in Figure 6.6.

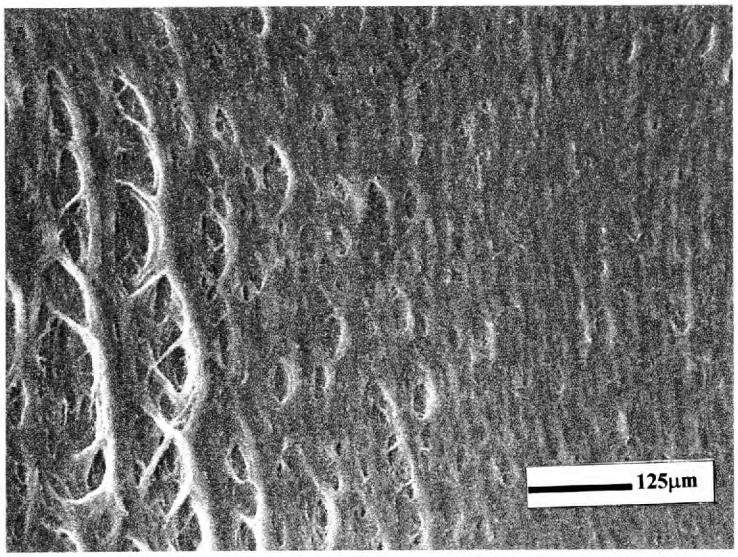

Figure 6.5 Magnified view of the damaged zone in PE80.

It is interesting to note from the Figure 6.6 that the copolymers showed bulk thinning as evidenced from the edges of the specimen. The extent of the bulk thinning (drawing) is most severe in the pipe materials whereas in HDPE the deformation is confined to the ligament area. This further emphasises the point that the surface draw mechanism is probably less prevalent in HDPE as indicated earlier in Figure 6.2.

Returning to Figure 6.6, it would seem that the addition of SCB promotes the blunting process (i.e. localised shear flow) provided a favourable stress (constraint) state coexisted. The high degree of plastic flow exhibited by the pipe materials due to the craze-shear transition produces a very large increase in the failure time. Consequently, the resistance to SCG can be expected to be extremely high at low constraint conditions. Although, BMPE has more or less the same concentration of M_w and SCB content as PE100, it did not exhibit a transition from crazing to shear deformation as did PE100. This is probably caused by the higher rate of void growth as evidenced from the micrograph (Figure 6.4), which may have hindered the transformation. Therefore, it would appear thatSCB is more effective than M_w for increasing resistance to SCG and may also account for the craze-shear transition in the PE100 or PE80. In addition, the large macroscopic plastic flow associated with the pipe materials could be closely akin to the cold draw behaviour as discussed in chapter 4. It becomes apparent that the blunting process is a prerequisite to invoke the ductile deformation mode. However, in

the absence of the blunting mechanism, the localise craze formed in HDPE eventually developed into a planar crack as seen in Figure 6.4.

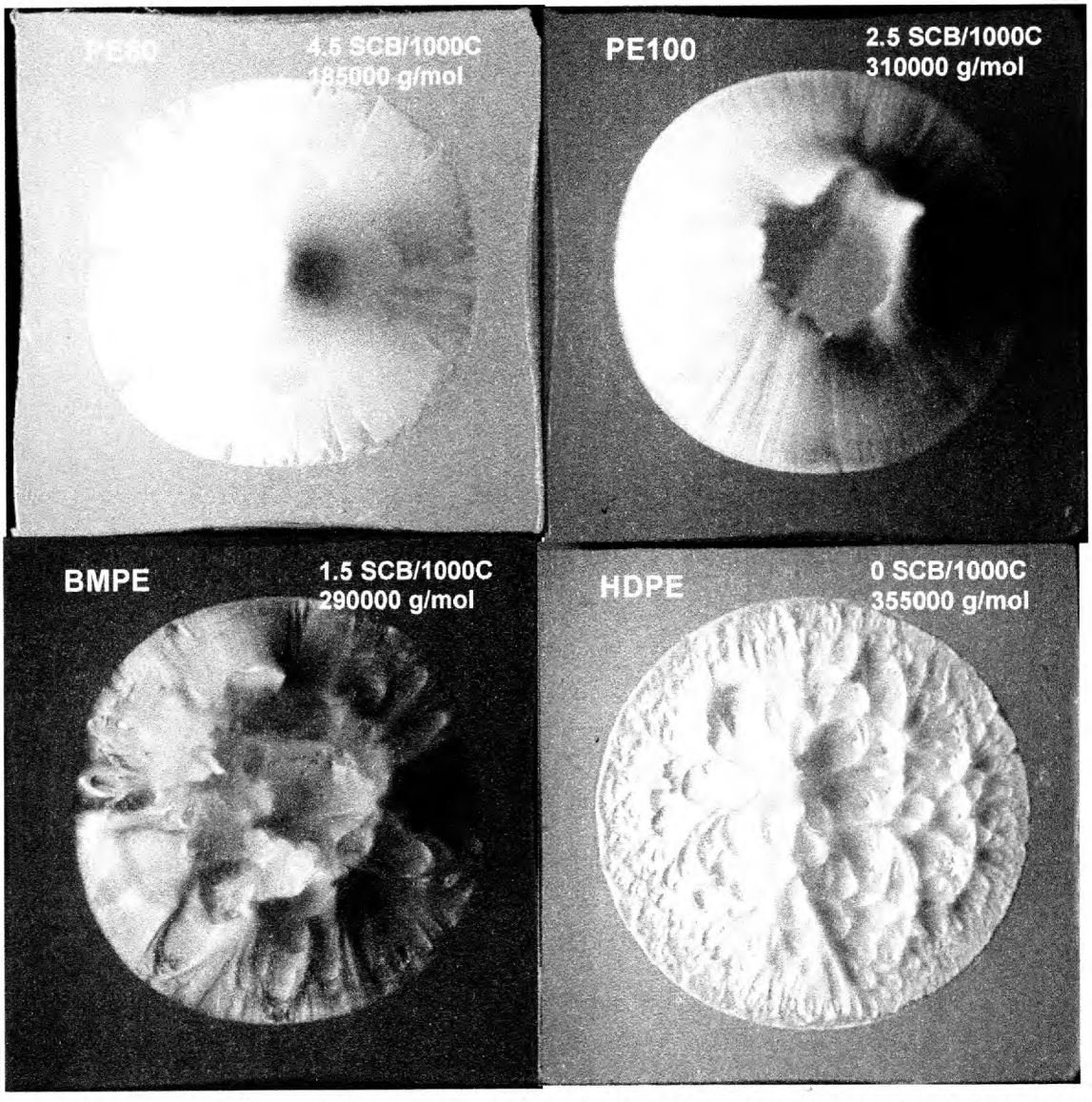

Figure 6.6 Comparison of the fracture surface between the different grades at low rates and low constraint conditions. Information on top right hand corner of each image indicates the SCB content and M_w. The photos are taken from a digital camera.

6.3 Structure-property analysis at high rates

Figure 6.7 compares the craze structure of PE80, PE100, BMPE and HDPE at high test rates under conditions of high notch tip constraint. As can be seen from the micrographs, the damaged structure of each grade showed a single fibrillar craze

structure with voids nucleated at random locations. As the loading rate increases, the damage characteristics of the grades become identical, suggesting a dominance of effects of rate over the property differences. These features have been highlighted and described in detail in Figures 5.36 and 5.44.

As the constraint is reduced, the effect of higher test rates somehow overwhelm the crack blunting mechanism and the crack propagates with very little apparent ductility, resulting in a fracture surface that is rough and comprised of patches of craze matter as seen in Figure 6.8. This is a feature common to all the grades. The results thus emphasis the importance of rate effects over the effect of structural properties and constraint at high rates. It is expected that the adiabatic heating/deformation would play a central role in the ductile-brittle transition in high loading rates. However, the role of this mechanism on the material behaviour was not examined here as it is outside the scope of the present investigation.

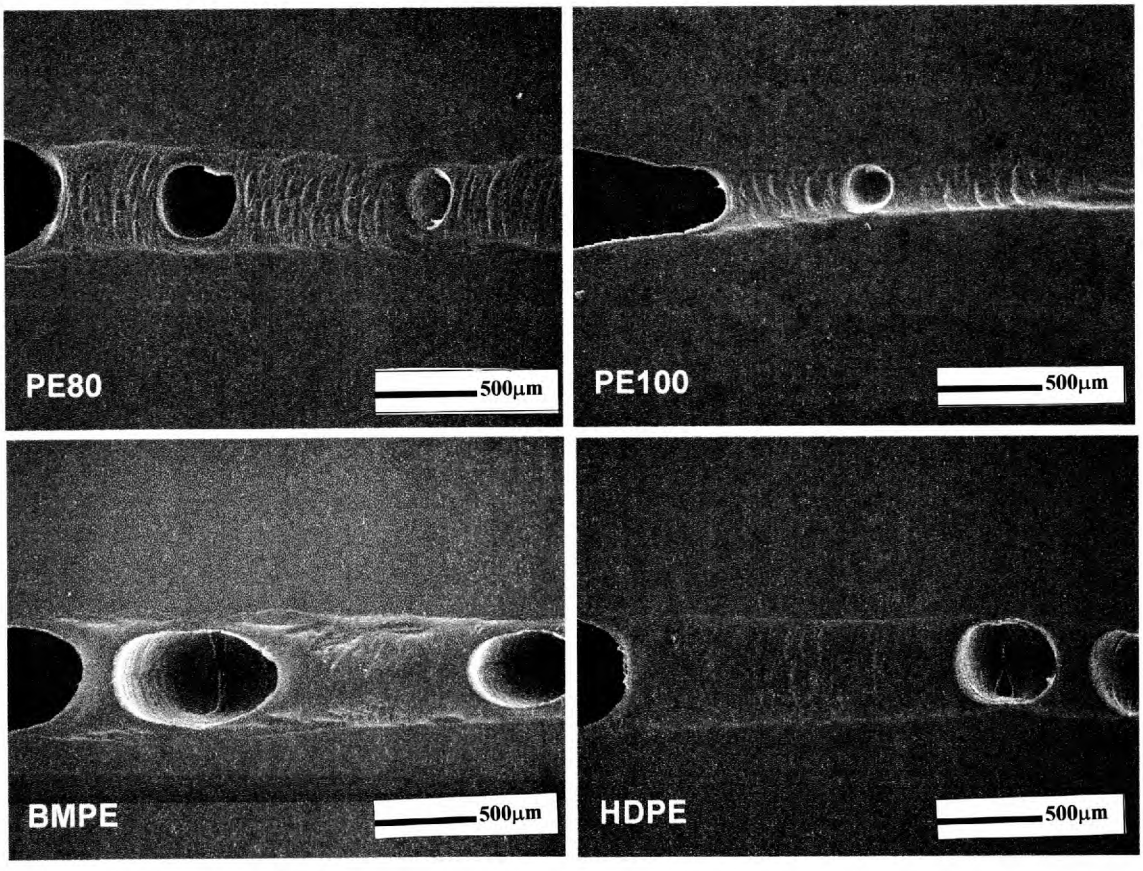

Figure 6.7 Comparison of the damage structure between the different grades at high rates and high constraint conditions.

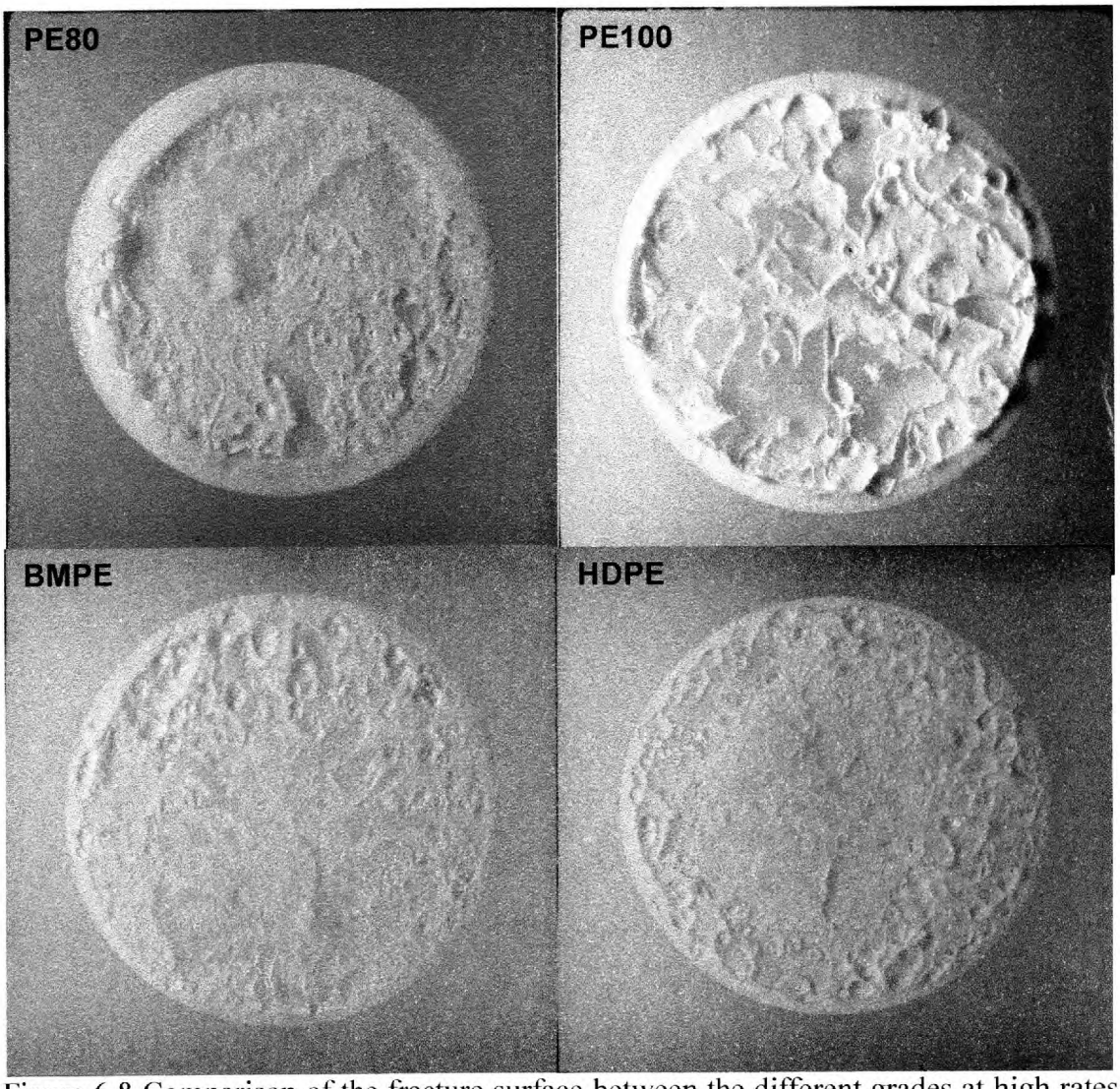

Figure 6.8 Comparison of the fracture surface between the different grades at high rates and low constraint conditions. The photos are taken from a digital camera.

6.4 Conclusions

At high constraints and low test rates, the combination of a high M_w and the addition of SCB were found to improve the resistance to SCG much beyond a single parameter (M_w or SCB) effect. As the crack tip constraint was reduced, it was found that the short chain branches are more effective than M_w for increasing resistance to SCG. This is because a high SCB content appears to encourage the crack blunting mechanism to materialise thereby arresting the crack initiation/ propagation and thus enhanced the SCG

performance. At high test rates, on the other hand, the material response is thought to be controlled by adiabatic effects rather than due to the molecular composition.

Chapter 7
Numerical Study

7.1 Introduction

The motivation for the numerical study can be traced to Pandya *et. al* [2000, 2001] and Ivankovic *et. al.* [2003]. In these studies, a family of measured rate-dependent cohesive curves was incorporated as the local fracture criterion in the prediction of the crack growth in polyethylene using three-point bend specimens. These studies revealed the limitation of such an approach as a mean of generating a unique criterion for every instance of crack advance due to the constraint effects along the crack path which was not adequately modelled in the simulations. Furthermore, these studies did not examine in the first instance the appropriateness of the measured cohesive laws for the numerical simulations. This can be addressed through the simulation of the CNT tests, which is the objective of the chapter. Ultimately, the present study will serve as the platform for the development of a fully predictive fracture model.

The Finite Volume (FV) method will be employed to simulate the CNT tests. FV is one of several numerical procedures that can be used to discretise and solve the governing equations of continuum mechanics into a system of algebraic equations that are solvable using computers. Several commercial numerical packages are available for solving continuum problems. One such package is FOAM (Field Operation And Manipulation) which is written in C++ language based on an open architecture design that allows the customisation and modification of existing codes for a specific application. Weller *et. al.* (1998) provided a discussion on the technical aspects of the codes and its implementation in FOAM. FOAM version 2.0 is used here and the reference manual is available from Nabla Ltd. [2001].

7.2 Application of FV method

The accessibility of high-speed computers in the present times has encouraged the use of computer-based simulation for solving engineering/physical problems. Various numerical schemes have been developed to solve problems involving solid body deformation, fluid flow and heat transfer. In solid mechanics problems, finite element (FE) procedures are preferred whilst finite volume (FV) methods have been used primarily for solving fluid flow and heat transfer problems. In recent times, the potential of FV method for solving solid mechanics problems was demonstrated by Demirdzic and Martinovic [1993] and Demirdzic and Muzaferija [1994]. The scheme was later expanded to include dynamic fracture problems (Ivankovic *et al.* [1994]). FV formulation has also been suggested for solving problems involving cohesive crack models. The appropriateness of such an approach has been highlighted by Ivankovic *et. al.* [2003] and demonstrated in the simulation of the slow crack growth in polyethylene using measured cohesive laws (Pandya *et. al.* [2000, 2001]). In another approach which has been adopted by Karac [2003], the cohesive zone was described by a Dugdale model to simulate the drop impact tests of plastic containers. Stylianou and Ivankovic [2002] addressed the implementation of the cohesive zone based procedures in FV formulation involving dynamic fracture problems. The FV method has proved to be simple, straightforward, conservative and efficient. For these reasons, the FV method is gradually gaining acceptance as an alternative to the widely used FE method for solving solid mechanics problems. Complete reference to the FV formulation used here is available in associated literature (Demirdzic and Ivankovic [1999] and Ivankovic [2000]).

7.3 CNT model

The elastic-plastic large strain structural analysis code including cohesive zone boundary condition was employed in the simulation of the CNT tests. A thorough review of the codes will not be given here as a detailed description of the particulars of the scheme can be found in Tropsa *et. al.* [2003]. Its main feature is that the updated Lagrangian large strain solution scheme (Maneeratana [2000]) was used while solving

incrementally the displacement field. The constitutive relation of the elastic-plastic behaviour was described by Hooke's law to account for the elastic stress increment combined with the Prandtl-Reuss elasto-plastic law to describe the plastic deformations. The definition of the stress was given by the second Piola-Kirchoff stress tensor whereas the deformation was defined by the Green strain tensor. The basic constitutive laws of the CNT model are defined by the stress-strain properties while the fracture is described by means of a measured cohesive law. To account for an arbitrary shaped stress-strain or cohesive curves the codes were modified to incorporate the solution algorithms proposed by Karac [2003], which will be discussed in §7.3.4.

7.3.1 Solution domains and boundary conditions

Figure 7.1 shows the solution domain and the prescribed boundary conditions of the CNT model. The solution domain represents an eighth of the whole specimen domain due to symmetry in three directions. The dimensions correspond to the CNT specimen based on a rectangular bar of dimensions 16 x 16 x 110 mm. The ligament radius is 2.8mm while the length of 30mm represents a half of the distance between the mechanical grips. The top surface (loading patch) and the cohesive zone (CZ) boundary (i.e. ligament area) were simulated using direction mixed boundary conditions (Figure 7.1(b)). The notch patch and the front surfaces were described as traction-free. Other boundaries were symmetry planes. A more orthogonal geometry (rectangular shaped as shown in Figure 7.1(b)) compared with the geometry domain in Figure 7.1 (a) was employed to reduce processing time. The effect on the results was found to be minimal.

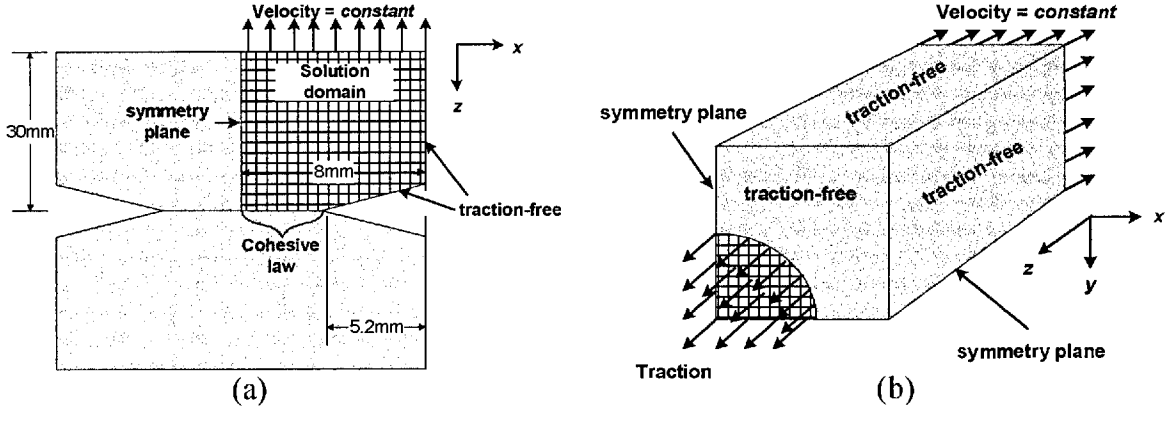

Figure 7.1 (a) Solution domain. (b) Prescribed boundary conditions.

7.3.2 Numerical Mesh

The solution domain was discretised into 24000 cells using a total of eight basic building blocks as shown in Figure 7.2. The mesh was sufficiently refined to insure mesh independent results without incurring high CPU time (Ting [2001]). On the loading patch, all blocks were treated as a single entity. On the other hand, at the cohesive and notch surfaces the blocks are defined as follows: Blocks 0 to 2 identified the CZ boundaries whereas the traction free surface (notch area) defined blocks 3 to 7. The mesh was graded towards the ligament centre by specifying a cell ratio of 1.5 between the largest and the smallest cell along x-direction of blocks 1 and 2. Additionally, a more gradual change of the cells shape from the CZ to traction free region was achieved by introducing additional arc-shaped blocks (blocks 3 and 4). There were 30 cells of equal size in the z-directions.

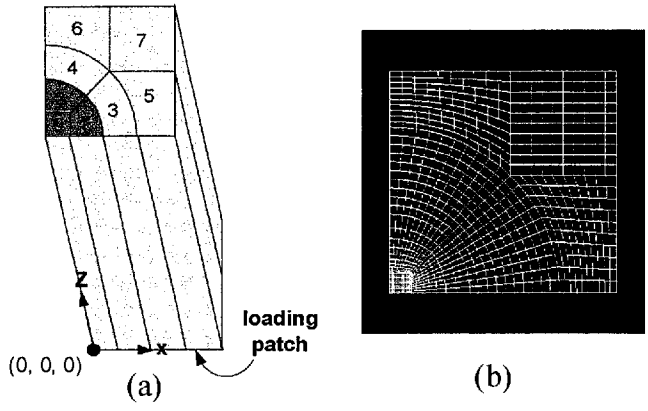

Figure 7.2 (a) Block structure. (b) Numerical mesh.

7.3.3 Material models

Since the true stress-strain curve was not available, an elastic-perfectly plastic model approximated from the nominal stress-strain curve is assumed as shown in Figure 7.3(a). The material parameters (yield stress, σ_y, yield strain, ε_y and modulus of elasticity, E) were obtained from the measured nominal stress-strain curves of chapter 4 except for the plastics modulus, E^p, which is set to 0 MPa. The cohesive law (i.e. the local fracture criterion) prescribed along the CZ boundary was based on the damage (decreasing) portion of the measured cohesive curves (red dashed line in Figure 7.3(b)) and the initial elasticity of the gauge portion of the specimen is ignored. In this

approach, the cohesive traction is set equal to the measured peak stress, σ_{max} which decreases to zero when the separation δ reaches a critical value δ_{COD}. The area under the curve (shaded area) defines the fracture energy. Such an approach is recently referred to as the extrinsic method which is numerically more stable than the intrinsic approach in which the elastic (rising) portion of traction-separation curve is included (Kubair and Geubelle [2003]). Values of the stress-strain and cohesive parameters being used in the simulation of CNT tests will be given in §7.5.

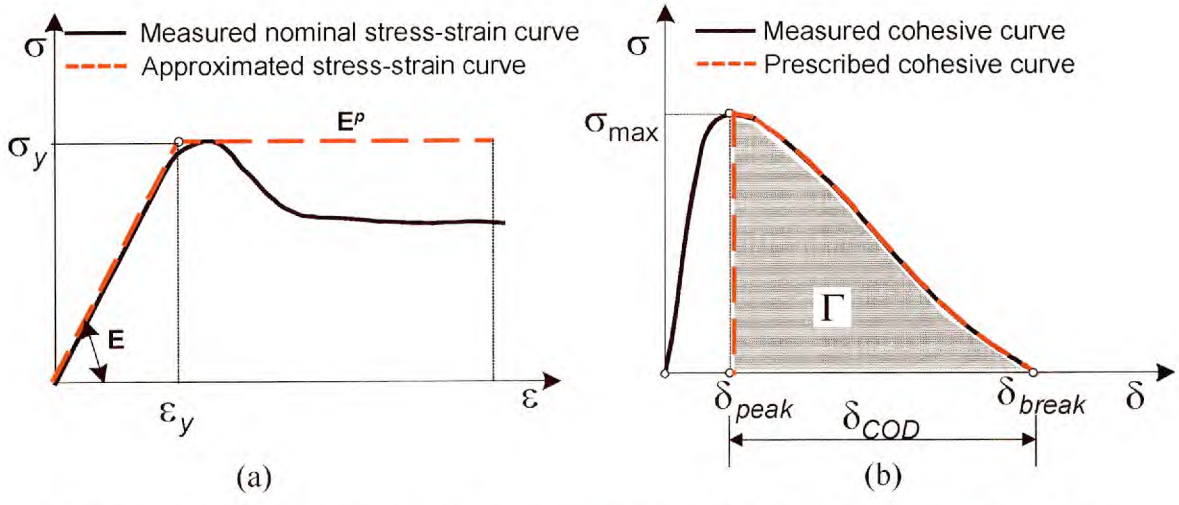

Figure 7.3 Material models. (a) Stress-strain curve. (b) Traction-separation curve.

7.3.4 Procedure to read in the basic constitutive laws

During the initialisation of the test case, the sub-routine (developed by Karac [2003]) reads in the properties of the stress-strain and the cohesive curves from the data files. The input curves are then stored in the computational node in the centre of the cells. Figure 7.4 illustrates the input points defined in the data files. Two procedures were introduced to the sub-routine of the input cohesive curves. First, a search procedure was developed for σ_{max} to replace the earlier version which assumed that σ_{max} is located in the first data point since this would be incorrect if the initial slope of the cohesive curve is considered. Second, the area under the curve was integrated after all data points were stored. Previously, the fracture energy was defined in a separate file which required updating for different prescribed curves.

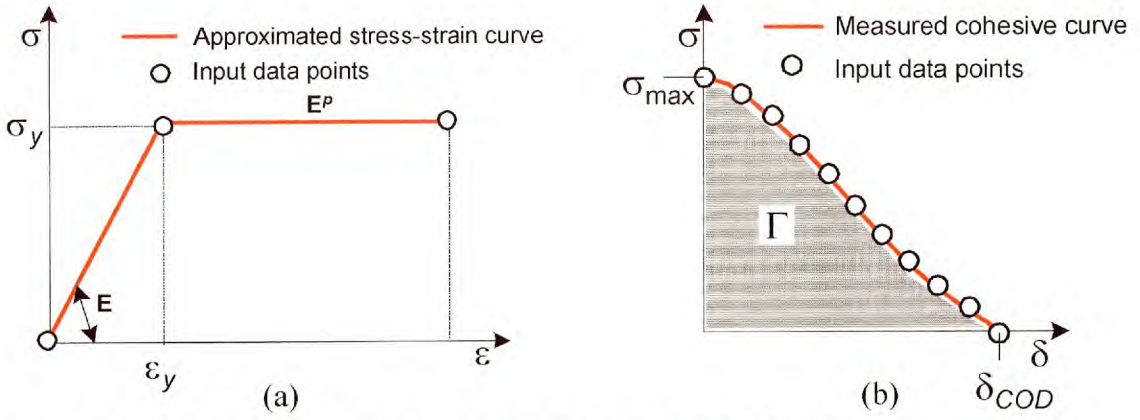

Figure 7.4 Input data points for (a) stress-strain curve and (b) traction-separation curve.

7.3.5 Algorithm for cohesive zone boundary condition

The FV setup for the CZ boundary condition is divided into three sets of conditions as illustrated schematically in Figure 7.5(a), and the solution algorithm is described below. Prior to the execution of the algorithm, another sub-routine is called to search for the softening stress σ_{soft}. The value of σ_{soft} was determined by linear interpolation between input data points. The calculated normal displacement δ_{normal} is used to locate σ_{soft} on the prescribed cohesive curve as illustrated in Figure 7.5(b). As the simulation is concerned mainly with the damage behaviour under increasing displacement (loading), the behaviour under unloading conditions is not critical to the numerical results.

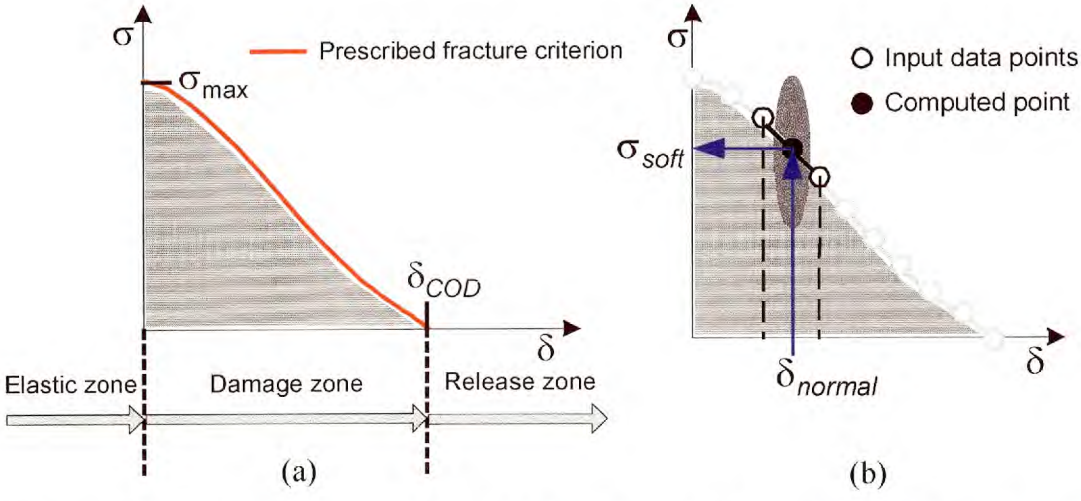

Figure 7.5 Schematic illustrations of (a) the FV setup on CZ boundary condition and (b) the search procedure for σ_{soft}. Dark shaded region denotes possible calculated traction values.

- Elastic zone - The cell will remain in the symmetry plane such that:

  $\delta_{normal} \leq \delta_{tolerance}$ and $\sigma_{normal} \leq \sigma_{max}$

  If true, $\delta_{normal} = 0$

  Otherwise, $\sigma_{normal} = \sigma_{max}$

  Where δ_{normal} is the normal displacement, $\delta_{tolerance}$ is a tolerance value, σ_{normal} is the normal stress component and σ_{max} is the peak stress of the prescribed cohesive curve. The $\delta_{tolerance}$ was specified to prevent floating exception errors with a value set equal to 0.1% of the δ_{COD} value, where δ_{COD} is the critical separation value of the prescribed cohesive curve.

- Damage zone - The cell switches to the full traction boundary condition when the following condition is satisfied:

  $\delta_{tolerance} < \delta_{normal} \leq \delta_{COD}$

  If true, $\sigma_{normal} = \sigma_{soft}$

- Release zone - The cell switches to traction-free when:

  $\delta_{normal} > \delta_{COD}$

  If true, $\sigma_{normal} = 0$

7.4 Validation of the CNT Model

The validation of the CNT model was performed by using a linear damage model since it resembled the decohesion behaviour of the materials studied. The cohesive parameters were given by σ_{max} = 29 MPa, δ_{COD} = 1.36 mm and Γ =19.8 kJ/m^2. The bulk material, on the other hand, was given the following values: σ_y = 12.5MPa, ε_y = 0.033, E =0.38Gpa and E^p =0MPa. The values were obtained from experiments on dumbbell and circumferentially notched tensile specimens tested at 0.1 mm/min. The simulation was performed at a fixed displacement rate of 0.1 mm/min.

Figure 7.6 shows the validation result of the CNT model. As can be seen in Figure 7.6(a), the calculated traction-separation (TS) curve fits the prescribed curve. However,

there is a slight deviation prior to reaching the peak stress. Examination of the TS curves of the notch tip cell and far cell in Figure 7.6(b) on the other hand, showed an exact fit on the prescribed damage model. The results thus indicate that the discrepancy is due to the averaging effects on the CZ boundary over the entire ligament.

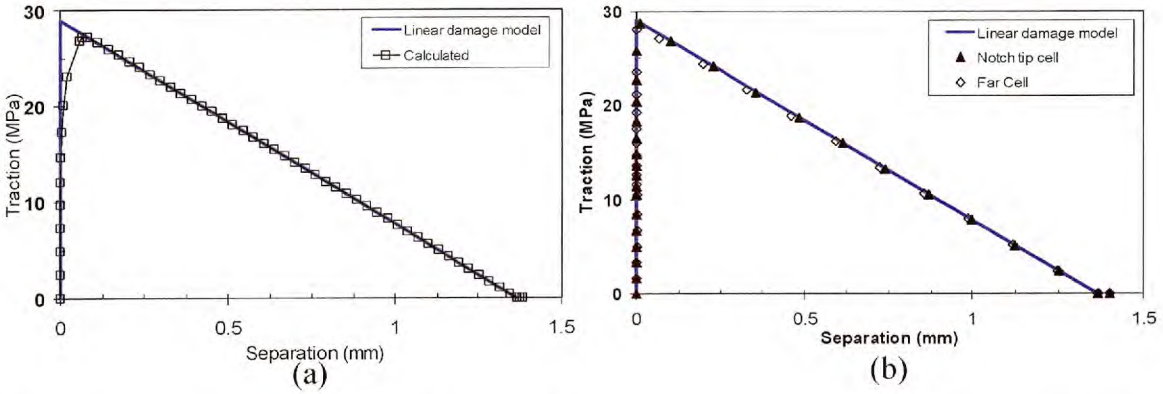

Figure 7.6 Validation of the CNT model. (a) Comparison between prescribed and calculated stress-displacement curve. (b) Stress-displacement curves of cell.

7.4.1 Energy components in the system

The energy conservation was checked by tracking the external, strain, kinetic and fracture energy of the system. Figure 7.7 shows the comparison of the variations of the energy components with time. Prior to the initialisation of the damage, most of the external work is converted into strain energy. This can be seen in Figure 7.7 in which the bulk of the total energy (which is a sum of the strain, fracture and kinetic work) stored in the specimen comes from an increase in the strain energy. Subsequently, the release of the strain energy causes a significant rise in the fracture energy. By comparison, the kinetic work contribution to the total energy curve is negligible throughout the simulation because of the slow test speeds. More importantly, the total energy curve is within the boundary of the external energy curve, suggesting that the solution is bounded and the discretisation is conservative. The difference in the external and total energy values of the system can be attributed to the numerical dissipation.

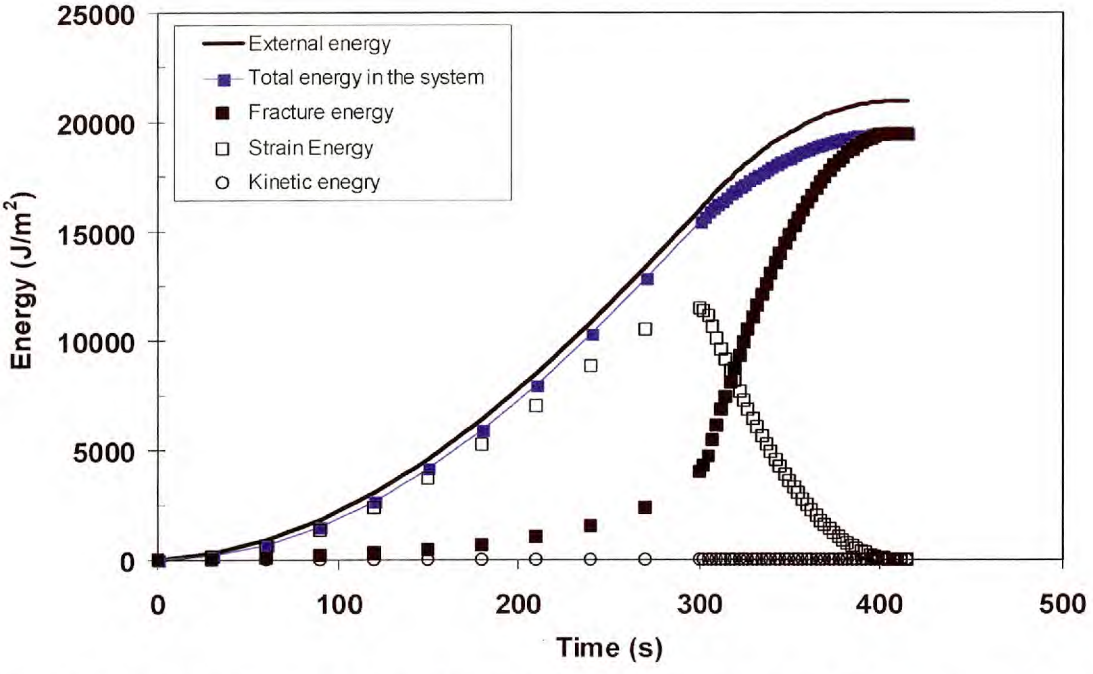

Figure 7.7 Comparison of the variations of the energy components in the system with time.

7.5 Simulation of CNT tests

The CNT simulations were performed on a limited range of the cohesive laws measured from the PE80 16mm thick specimens with a 10% LBA ratio. In each simulation at a particular velocity, the stress-strain and cohesive curves measured at the corresponding rate were applied. Test speed was constant and achieved by applying a fixed displacement increment in each time step. However, the CNT simulations considered here were based on slow test speed experiments, which can lead to long computation times. In order to save CPU time and hard disk space a variable time step strategy was adopted. In this approach, a large incremental time step is specified initially to speed up calculations. This is because a substantial amount of time (displacement) is required to initiate the damage. However, once the damage is initiated the fracture can occur in a relatively short period of time. Hence, the time step is reduced near the strain softening stage. The material properties and CZM parameters used in the simulations are summarised in Table 7.1 while the time steps are listed in Table 7.2.

Material properties				CZM parameters		
Density: 940 kg m^{-3}		Poisson ratio: 0.3				
Velocity (m/s)	σ_y (MPa)	ε_y	E (GPa)	σ_{max} (MPa)	Γ (kJ/m^2)	δ_{COD} (mm)
$8.3x10^{-4}$	20.6	0.032	0.64	35.6	25.2	1.27
$8.3x10^{-5}$	15.7	0.031	0.51	32.8	31.0	1.69
$8.3x10^{-6}$	13.2	0.030	0.44	30.0	27.6	1.64
$8.3x10^{-7}$	12.2	0.038	0.32	27.8	27.5	1.66

Table 7.1 Material properties used in the CNT simulations

	Time step 1			Time step 2	
Velocity (m/s)	Start time	Δt_1	End time	Δt_2	End time
$8.3x10^{-4}$	0	0.08	0.16	0.04	0.8
$8.3x10^{-5}$	0	0.5	3.5	0.25	10
$8.3x10^{-6}$	0	5	45	2.5	102.5
$8.3x10^{-7}$	0	20	940	5	1030

Table 7.2 Time step defined in the CNT simulation. Where Δt_1 is time step 1 and Δt_2 time step 2. All times are given in seconds.

7.5.1 Results and discussion

Figure 7.8 shows the comparison between the prescribed and average calculated TS curves at various loading speeds. The experimental curves represent the prescribed fracture criterion which denotes only the post-peak branch of the measured cohesive law as described in Figure 7.3(b). It can be seen that the calculated TS curves fit the prescribed curves of any arbitrary shape, regardless of test speeds. The deviation prior to the peak stress is due to the cell averaging effects as explained in Figure 7.6.

Figure 7.9 shows the TS curves obtained from the CNT simulations. The experimental curve denotes the measured cohesive curve while the 5mm GL (gauge length) curve represents the simulation where the strain is calculated over a gauge length of 5mm (after correcting for symmetry). The 5mm GL curve, therefore, represents the experimental set-up using a video extensometer with a gauge length of 5mm, whereas

the 60mm GL curves correspond to a 60mm gauge length (see Figure 3.12). According to Figure 7.9 the peak stress is unaffected by the choice of the gauge length. In contrast, the pre-peak extension increases with an increase in gauge length due to a significant amount of the displacement of the gauge length. Therefore, an accurate description of the traction-separation properties would require a small gauge length to be defined so that the bulk contribution is minimised. The results thus reinforced the experimental observation discussed in Figure 3.11.

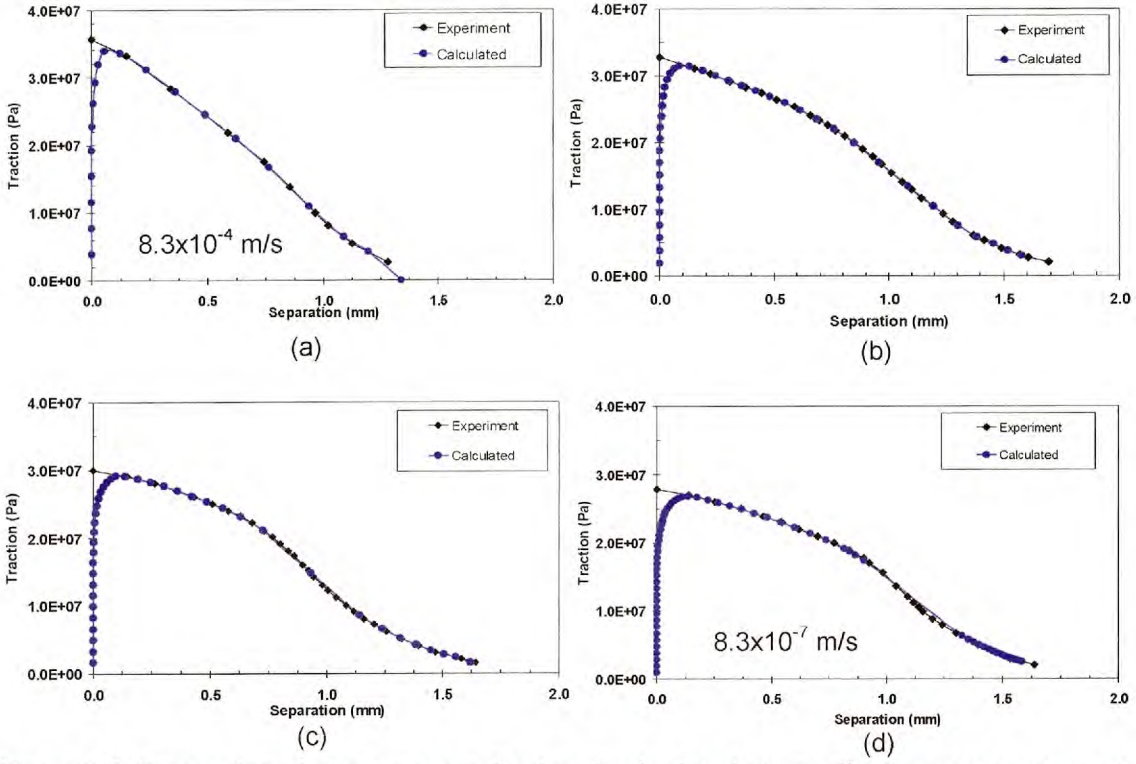

Figure 7.8 Comparison between prescribed and calculated stress-displacement curves at various loading speeds.

As can be seen from Figure 7.9, the model (5mm GL curve) is able to accurately simulate the initial part of the TS curve. Beyond the peak, the softening stage is overestimated while the total separation distance is underestimated. This limitation can be attributed to the prescription of the constitutive law using a perfectly elastic-plastic model which is stiffer than the actual material model (Figure 7.3(a)). Since a stiffer material is likely to have a higher resistance against the deformation. This would suggest that the CNT model depends also implicitly on the shape of the stress-strain curve, emphasising the importance of using true stress-strain properties. The averaging effects and non-uniformity of the damage evolution across the ligament may also

have influenced the simulation results. More importantly, the simulations highlight the significance of specifying a small gauge length so that an accurate assessment of the fracture behaviour can be obtained.

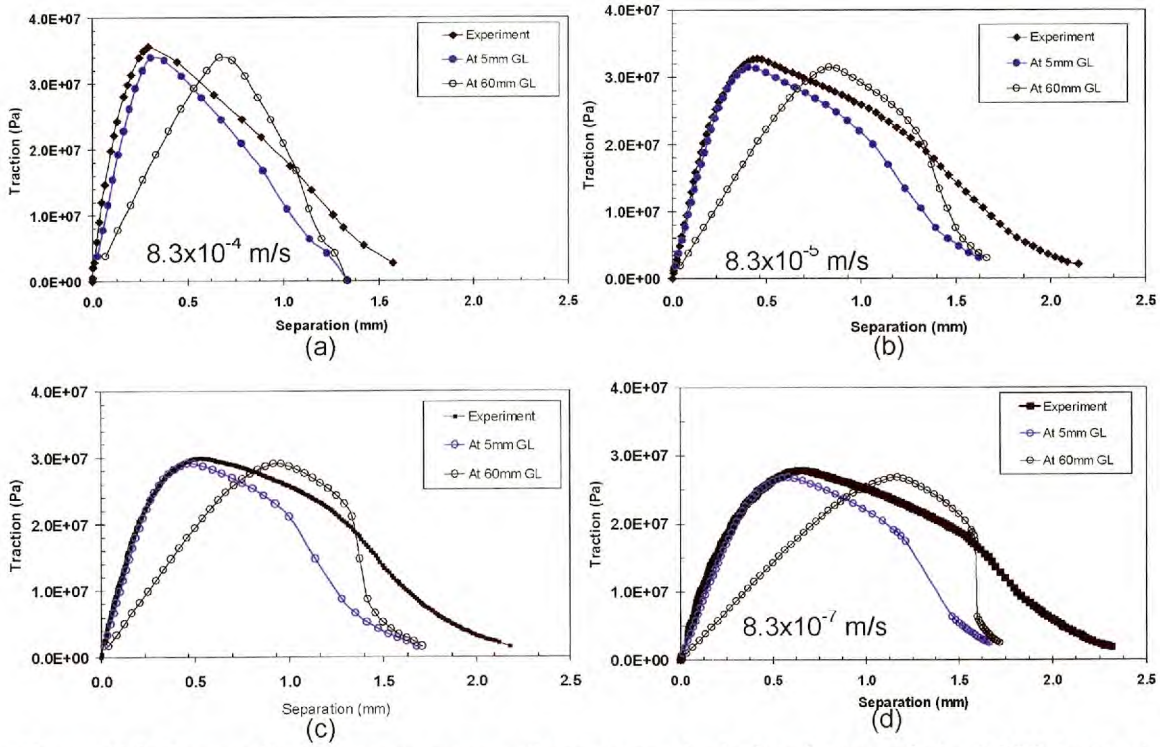

Figure 7.9 Stress-displacement curves from numerical simulation of the CNT tests at various loading speed.

7.6 Conclusions

Preliminary numerical simulations of the CNT tests were performed. The CNT model uses elastic-plastic constitutive law approximated from measured nominal stress-strain curves while experimental cohesive curves were incorporated as the local fracture criterion. The simulation showed a good agreement with the experimental curve up to the peak load but could not adequately describe the post-peak behaviour. This discrepancy can be attributed to the approximation of the strain hardening characteristics which emphasised the need for a more precise definition based on a true stress-strain measurement. Undoubtedly, further work on modelling the CNT tests is required, which was far beyond the scope of the present investigation. Some recommendations for future work will be given in chapter 8.

Chapter 8
Conclusions and recommendations

8.1 Introduction

This chapter summarises the main findings of the thesis and provides some proposals for future work. Within each section the conclusions and the recommendations pertaining to the topic will be outlined.

8.2 Stress-strain behaviour

Under uniaxial stretching, the stress-strain behaviour of polyethylene was found to be rate-dependent which in turn influenced the yield point and the necking behaviour. These findings are consistent with the results reported in the literature. An intricate relationship was showed to exist between the density (crystallinity) and the degree of molecular entanglement, which could explain the difference in the behaviour between the polyethylene grades.

The present investigation did not take into account the decrease in the neck cross section at yield and hence the characterisation beyond the necking point is ill-defined. However, the traction-separation behaviour of tough polyethylene grades examined at low constraint conditions would suggest the comparative importance of obtaining an accurate assessment of the strain hardening characteristics. One manifestation of this is the absence of the cold-drawing plateau in polyethylene in a true stress *vs* true strain measurement as reported by G'Sell *et. al.* [1992]. In fact, the true stress-strain curve did not exhibit any stress drop at yield or any discontinuity, in contrast the curve showed a continuous rise of the stress as the material strain hardened. As a result, the conventional stress-strain measurements were inadequate in providing a precise description of the microstructural transformations of the material under stress. The

numerical study furthermore emphasised the need for a more precise definition based on the effective stress and the effective strain in the simulation of CNT tests. For these reasons, future work on tough polyethylene grades should be concentrated on characterising true stress-strain properties.

8.3 Traction-separation behaviour

The overall objective of the thesis is to determine the effect of constraint, in addition to rate on the traction-separation behaviour of polyethylene. A detailed conclusion of the results has been provided in the respective sections of chapter 5 and only a brief summary will be given here. To this end the investigation has demonstrated conclusively that the depth of the notch affects the notch tip constraint much more than does the thickness. The deeper the notch, the greater is the notch tip constraint. Conversely, the constraint is reduced as the notch depth decreases. Also, the peak stress is reduced but the break separation increases significantly, especially at low rates of testing. The high notch tip constraint (deep notch) thus best reflects the material inherent resistance to SCG in the brittle fracture mode while the lower constraint level would represent the material performance under the ductile failure mode. The dependency on the notch tip constrain has led to contrasting damage-failure behaviour between different grades of polyethylene and hence the overall energy dissipation process. By taking into account the effect of constraint in addition to rate, the material fracture response is likely to correlate better with the performance of the pipe material under real service conditions where a wide range of arbitrary constraint condition could be found. Such an analysis should provide the crucial information about the material performance for the manufacturers in the development and the characterisation of new generation pipe materials.

The experience gained from the present investigations including data contributed from previous studies (Duan and Williams [1998] and Pandya and Williams[2000]) has led to the following proposed CNT test configurations listed in Table 8.1 for the characterisation of the materials performance in both the brittle and ductile modes of failure. The recommended test configurations should provide manufacturers a "quick

and cost-effective test" in the assessment of the material SCG performance by taking into account the influence of the constraint and rate effects, both of which have been proved to play a vital role in the damage-failure mechanisms.

Domain	LBA ratio	Specimen geometry	Test speed (mm/min)		
Brittle	10%	10 x 10 x 110 mm	0.005	0.5	50
Ductile	50%	10 x 10 x 110 mm	0.005	0.5	50

Table 8.1 Proposed CNT test configurations.

Furthermore, the study has identified the various conditions (constraint and rate) in which craze yielding prevailed. Therefore, in future work it would be desirable to obtain a stress criterion perhaps based on the constraint factor, M for craze yielding (initiation) analogous to that for shear yielding criterion (eg. Tresca yield criterion, von Mises criterion etc.).

8.4 Structure-property analysis

The stop-section technique proposed by Clutton [2002] has demonstrated to be effective in examining the damage evolution at different stages of loading. This is confirmed by the numerous micrographs of the cross-sectioned specimen produced in the present work. By linking the microscopy work to the macroscopically measured traction-separation properties, a unified approach was developed whereby a relationship was established between the mechanical properties and microstructural behaviour. It was found that the combination of a high M_w and the presence of SCB content improved the SCG resistance under conditions of high constraints and low test rates. In contrast, at low constraints and low test rates the short chain branches appear to be more effective than M_w for increasing resistance to SCG. On the other hand, the material response is thought to be thermally controlled at high rates, regardless of the constraint level.

The technique could be improved by eliminating the procedures associated with the preparation of the drilled holes to position the jig after the test is stopped (see Figure 3.13). A simple solution is to make the locating pins of the jig movable as illustrated in Figure 8.1. In this way, the holes can be pre-drilled since the jig can be adjusted to compensate for any changes in the distance between the drilled holes. The procedure could also be enhanced by "freezing" the stopped sample in a nitrogen environment prior to sectioning and SEM, thereby minimising any elastic effects during unloading.

A recent publication by Plummer *et. al.* [2001] produced very clear and detail images of the fibrils in a craze structure. The images were taken from sectioned thin film produced with a microtome, which was embedded in an epoxy resin to improve the contrast between specimen-epoxy interfaces as illustrated in Figure 8.2. The high resolution of these images was achieved without resorting to high beam voltage which is a common source of damage to the fine structure in the form of microcracks. Given that a vast amount of information on the structural characteristics can be extracted from a sectioned specimen, future microscopy work should be geared towards such thin-film type analysis where a more reliable description of the deformation mechanism can be obtained.

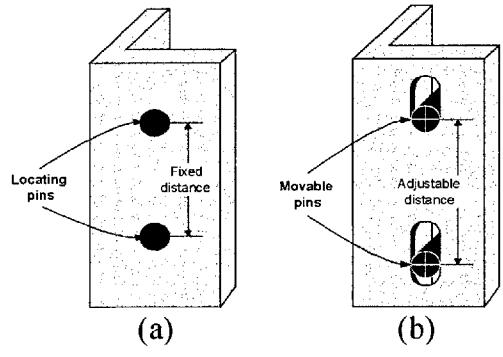

Figure 8.1 Jig design (a) Original and (b) Proposed.

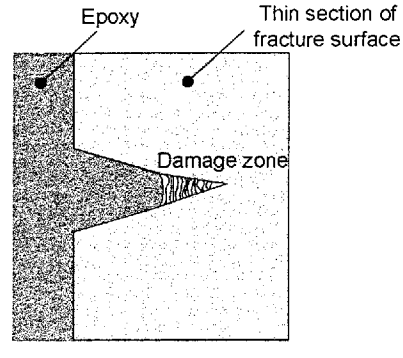

Figure 8.2 Proposed microscopy work using thin-sectioned specimen embedded in epoxy.

8.5 Numerical study

The numerical study presents a preliminary investigation into the simulation of CNT tests based on the finite volume approach. The CNT model was implemented using the

commercial finite volume library FOAM. As the true stress-strain curve was not available at this stage of the study, the material properties of the cells were specified by an elastic-perfectly plastic model approximated from a measured nominal stress-strain curve. On the other hand, fracture is described using the measured high constraint cohesive law. The simulations were performed at various speeds between $8.3x10^{-4}$ m/s (50 mm/min) and $8.3x10^{-7}$ m/s (0.05 mm/min). The CNT model was able to simulate accurately the initial part of the experimental curve but it overestimated the softening stage while the overall extension was underestimated. This discrepancy highlights the need of specifying the true stress-strain properties.

There are also several areas that require further modelling efforts. First, it concerns the simulation of CNT tests with low constraint traction-separation curves which has been neglected in the present study. This is because the current mesh cannot simulate large extensions and plastic deformation of a narrow region around the ligament, as observed in the experiments. One possible solution is to introduce the adaptive mesh refinement method as suggested by Karac [2003]. Furthermore, the simulation at a different rate or constraint condition would require a separate set of stress-strain and cohesive curves to be specified. Therefore, a long term approach is to have a procedure that reads in all available rate-constraint dependent cohesive curves, including the stress-strain curves for the numerical simulation. The codes should also be armed with a search procedure, perhaps based on the crack tip opening rate and constraint factor M, capable of seeking out from the family of curves the cohesive law pertinent to the current state of the test condition. If these problems (adaptive mesh refinement and search procedure) could be addressed within the CNT model then it should become easier to transfer these "codes" to other geometries such as the three-point bend specimen to predict the crack growth in tough polyethylene.

References

Amornsakchai T, Olley RH, Bassett DC, Al-Hussein MOM, Unwin AP and Ward IM, (2000). On the influence of initial morphology on the internal structure of highly drawn polyethylene. Polymer 41:8291-8298.

Argon AS and Salama MM, (1977). Growth of crazes in glassy polymers. Phil. Mag. 36:1217

Beech SH, Duncan JN and Millar JB, (2001a). Polyethylene pipeline systems – The big success story. In the conference proceedings of Plastics Pipes XI, Germany, 113-122.

Beech SH, Ferguson CR and Clutton EQ, (2001b). Mechanisms of slow crack growth in PE pipe grades. In the conference proceedings of Plastics Pipes XI, Germany, 401-410.

Bhattacharya SK and Brown N, (1985). The initiation of crack growth in linear polyethylene. J. Matl. Sci. 20:2767-2775.

Brooks N, Duckett RA and Ward IM, (1992). Investigation into double yield points in polyethylene. Polymer, 33 (9):1872-1880.

Brown N and Lu X, (1995). A fundamental theory for slow crack growth in polyethylene. Polymer 36 (3):543-548.

Brown N and Ward IM, (1983). The influence of morphology and molecular weight on ductile-brittle transitions in linear polyethylene. J. Matl. Sci. 18:1405-1420.

Boyce MC, Arruda EM and Jayachandran R, (1994).The large strain compression, tension, and simple shear of polycarbonate. Polym. Eng. Sci. 34(9):716-725.

Cawood MJ, Channell AD and Capaccio G, (1993). Crack initiation and fibre creep in polyethylene. Polymer, 34(2):423-425.

Chan MKV and Williams JG, (1983). Slow stable crack growth in high density polyethylene. Polymer 24:234-244.

Chan MKV and Williams JG, (1983). J-integral studies of crack initiation of a tough high density polyethylene. Intl. J. Fract. 23:145-159.

Channel AD and Clutton EQ, (1992). The effects of short chain branching and molecular weight on the impact fracture toughness of polyethylene. Polymer 33(19):4108-4112.

Choi S and Broutman LJ, (1985). A plane-strain tensile specimen to determine ductile-brittle transitions in polyethylene pipe grade resins. In proceedings of 9th Plastic Fuel Gas Pipe symposium, 141-159.

Clutton EQ, (2002). Private communication.

Demirdzic I and Ivankovic A, (1999). Finite volume stress analysis. Imperial College London Lecture notes, UK.

Demirdzic I and Martinovic D, (1993). Finite volume method for thermo-elasto-plastic stress analysis. Comput. Meth. Appl. Mech. Eng. 109:331-349.

Demirdzic I and Muzaferija S, (1994). Finite volume method for stress analysis in complex domains. Intl. J. Num. Meth. Eng. 37:3751-3766.

Donald AM, (1997). Crazing. In the Physics of Glassy Polymers- 2nd Edition (editors, Haward RN and Young RJ), Chapman & Hall, 295-341.

Duan DM, (1996). Fracture toughness and long term fracture behaviour of polyethylene. PhD Thesis, University of London, UK.

Duan DM and Williams JG, (1998). Craze testing for tough polyethylene. J. Matl. Sci. 33:625-638.

Dugdale DS, (1960). Yielding of steel sheets containing slits. J. Mech. Phys. Solids, 8:100-104.

Egan BJ and Delatycki O, (1995). The morphology, chain structure and fracture behaviour of high density polyethylene. J. Matl. Sci. 30 (13):3307-3318.

Elices M, Guinea GV Gómez J and Planas J, (2002). The cohesive zone model: advantages, limitations and challenges. Eng. Fract. Mech. 69:137-163

G'Sell C, Hiver JM and Dahoun A, (1992). Video-controlled tensile testing of polymers and metals beyond the necking point. J. Matl. Sci. 27:5031-5039.

G'Sell C, Hiver JM and Dahoun A., (2002) Experimental characterisation of deformation damage in solid polymers under tension, and its interaction with necking. Intl. J. Solids Struct. 39:3857-3872.

Gledhill RA and Kinloch AJ, (1979). Mechanics of crack growth in epoxide resins. Polym. Eng. Sci. 19(2):82-88.

Hamouda HBH, Simoes-betbeder M, Grillon F, Blouet P, Billon N and Piques R, (2001). Creep damage mechanisms in polyethylene gas pipes. Polymer 42:5425-5437.

Haward RN, (1994). The derivation of a strain hardening modulus from true stress-strain curves for thermoplastics. Polymer 35(18):3858-3862.

Hazra SK, (2000). Crazing and yielding of polyethylene under impact. PhD Thesis, University of London, UK.

Hong S and Kim KS, (2003). Extraction of cohesive zone laws from elastic far-fields of a cohesive crack tip: a field projection method. J Mech. Phys. Solids 51:1267-1286.

Hui CJ and Kramer EJ, (1995). Molecular weight dependence of the fracture toughness of glassy polymers arising from crack propagation through a craze. Polym. Eng. Sci. 35:419-425.

Ivankovic A, (2000). Computational continuum mechanics. Lecture notes, Imperial College London, UK.

Ivankovic A, Demirdzic I, Williams JG and Leevers PS, (1994). Application of the finite volume method to the analysis of dynamic fracture problems. Intl. J. Fract. 66:357-371.

Ivankovic A, Pandya KC and Williams JG, (2003) Crack growth predictions in polyethylene using measured traction-separation curves. Eng. Fract. Mech. in press.

Karac A (2003). Drop impact of fluid-filled polyethylene containers. PhD Thesis, University of London, UK.

Kinloch AJ and Williams JG, (1980). Crack blunting mechanism in polymers. J. Matl. Sci. 15:987-996.

Kinloch AJ and Young RJ, (1983). Fracture behaviour of polymers. Elsevier Science Publishers Ltd.

Kirk MT, Koppennoeter KC and Shih CF, (1993). Effect of constraint on specimen dimensions needed to obtain structurally relevant toughness measures. Constraint Effects in Fracture, edited by Hackett E.M. *et. al.*, ASTM, Philadelphia, 79-103.

Kramer JE and Berger LL, (1990). Fundamental processes of craze growth & fracture. Advances in Polymer Science, (edited by Kausch H.H.), Springer-Verlag, Berlin, 91/92: 1-68.

Kramer JE and Hart W, (1984). Theory of slow state crack growth in polymer glasses. Polymer 25:1667-1678.

Kubair DV and Geubelle PH, (2003). Comparative analysis of extrinsic and intrinsic cohesive models of dynamic fracture. Intl. J. Solids Struct. 40:3853-3868.

Lagaron JM, Capaccio G, Rose LJ and Kip BJ, (2000). Craze morphology and molecular orientation in the slow crack growth failure of polyethylene. J. Appl. Polymer Sci. 77:283-296.

Leevers PS, (1995). Impact and dynamic fracture of tough polymers by thermal decohesion in a Dugdale zone. Intl. J. Fract. 73:109-127.

Li W and Siegmund T, (2002). An analysis of crack growth in thin-sheet metal via a cohesive zone model. Eng. Fract. Mach. 69:2073-2093

Lin L and Argon AS, (1994). Review- structure and plastic deformation of polyethylene. J. Matl. Sci. 29:294-323.

Lu X and Brown N, (1997). Abnormal slow crack growth in polyethylene. Polymer 38:5749-5753.

Lu X and Brown N, (1992). A test for slow crack growth failure in polyethylene under a constant load. Polymer testing 11:309-319.

Lu X, Qian R and Brown N, (1991). Notchology – The effect of the notching method on the slow crack growth failure in tough polyethylene. J. Matl. Sci. 26:881-888.

Lu X, Wang X and Brown N, (1988). Slow fracture in a homopolymer and a copolymer of polyethylene. J. Matl. Sci., 23(2):643-648.

Lu X, Zhou Z and Brown N, (1997). A sensitive mechanical test for slow crack growth in polyethylene. Polym. Eng. Sci. 37(11):1896-1900.

Malvern LE, (1969). Introduction to the mechanics of a continuous medium. Prentice-Hall Inc..

Maneeratana K, (2000). Development of the finite volume method for non-linear structural Applications. PhD thesis, University of London.

McCrum NG, Buckley CP and Bucknall CB, (1996). Principles of polymer engineering. Oxford University Press.

Melick van HGH, Govaert LE and Meijer HEH (2003). On the origin of strain hardening in glassy polymers. Polymer 44:2493-2502

Nabla Ltd. (2001). FOAM version 2.0- demonstration and programmers guide. http://www.nabla.co.uk/

Narisawa I and Takemori MT, (1989). Fracture toughness of impact-modified polymers based on the J-integral. Polym. Eng. Sci. 29(10):671-678.

Nishio N, Iimura S, Yasuhara M and Nagatani F, (1985). Standard full notch creep test method and some test results on MDPE pipes. In proceedings of 9th Plastic Fuel Gas Pipe symposium, 29-39.

Nitta KH and Ishiburo T, (2002). Ultimate tensile behaviour of linear polyethylene solids. J. Polym. Sci. Part B: Polym. Phys. 40:2018-2026.

Nunes RW, Martin JR and Johnson JF, (1982). Influence of molecular weight and molecular weight distribution on mechanical properties of polymers. Polym. Eng. Sci. 22(4)205-228.

O'Connell PA, Bonner MJ, Duckett RA and Ward IM, (1995). The relationship between slow crack growth propagation and tensile creep behaviour in polyethylene. Polymer 36(12):2355-2362.

O'Connell PA, Bonner MJ, Duckett RA and Ward IM, (2003). Effect of molecular weight and branch content on the creep behaviour of oriented polytheylene. J. App. Polym. Sci. 89:1663-1670.

Pandya KC, (2000). The study of long term fracture properties in tough polyethylene. PhD Thesis, University of London, UK.

Pandya KC, Clutton EQ and Rose LJ, (2003a). A structure based assessment of ductile deformation mechanisms in polyethylene. In preparation.

Pandya KC, Clutton EQ and Rose LJ, (2003b). The Influence of molecular structure on impact and stress crack performance in polyethylene. In preparation.

Pandya KC, Ivankovic A and Williams JG, (2000). Cohesive zone modelling of crack growth in polymers. II: numerical simulation of crack growth. Plast. Rubber Compos. 29(9):447-452.

Pandya KC, Ivankovic A and Williams JG, (2001). Crack growth predictions in polyethylene using measured traction-separation curves. Advances in Fracture and Damaged Mechanics II edited by Guagliano M. and Aliabadi M.H., Hoggar, 1-6.

Pandya KC and Williams JG, (2000a). Measurement of cohesive zone parameters in tough polyethylene. Polym. Eng. Sci. 40(8):1765-1776.

Pandya KC and Williams JG, (2000b). Cohesive zone modelling of crack growth in polymers. I: experimental measurement of cohesive law. Plast. Rubber Compos. 29(9): 439-446.

Plummer CJG, Goldberg A and Ghanem A, (2001). Micromechanisms of Slow Crack Growth in Polyethylene under Constant Tensile Loading. Polymer 42:9551-9564.

Que NS and Tin-Loi F, (2002). Numerical evaluation of cohesive fracture parameters from a wedge splitting test. Eng. Fract. Mech. 69 :1269-1286.

Riemslag T, (1997). Crack growth in polyethylene. PhD thesis, Delft University of Technology, The Netherlands.

Siegmund T and Brocks W, (1999). Prediction of the work of separation and implications to modelling. Intl. J. Fract. 99:97-116.

Stylianou V and Ivankovic A, (2002). Finite volume analysis of dynamic fracture phenomena. II- A cohesive zone type methodology. Intl J. Fract. 113:125-151.

Tijssens MGA, Giessen van der and Sluys LJ, (2000). Modelling of crazing using a cohesive surface methodology. Mech. Matl. 32:19-35

Ting SKM, (2001). The study of crack growth in tough polyethylene by cohesive zone methodology. MPhil - PhD transfer report, Imperial College London, UK.

Ting SKM, Williams JG and Ivankovic A, (2003a). Slow crack growth behaviour of polyethylene under various constraint conditions. In the proceedings of the 12th International Conference on Deformation, Yield and Fracture of Polymers, UK, 17-20.

Ting SKM, Williams JG and Ivankovic A, (2003b). Effects of constraint on the traction-separation behaviour of polyethylene. Fract. Polym. Comp. Adh. II, Elsevier, in press.

Tränkner T, Hedenqvist M and Gedde UW, (1996). Structure and crack growth in gas pipes of medium density and high-density polyethylene. Polym. Eng. Sci. 36:2069-2076.

Tropsa V, Georgiou I, Ivankovic A and Kinloch AJ, (2003). Finite volume modelling of adhesive joints at slow and impact loading rates. In the proceedings of the 4th International Congress of Croatian Society of Mechanics, Bizovac, Croatia.

Tvergavrd V and Hutchinson JW, (1992). The relation between crack growth resistance and fracture process parameters in elastic-plastic solids. Mech. Phys. Solids 40:1377-1397

Unwin AP, Duckett RA, Ward IM, Collins TLD, Sweeney J and Coates PD, (2002). Suppression of necking in polyethylene. J. Appl. Polm. Sci. 86:3135-3147.

Vallés EM and Failla MD, (2003). Effect of temperature on the tensile mechanical behaviour of irradiated linear polytheylene. J. Polym. Sci. 88:1925-1935.

Ward IM, (1983). Mechanical properties of solid polymers- 2nd edition. John Wiley & Sons Ltd..

Ward IM and Hadley DW, (1993). An introduction to the mechanical properties of solid polymers. John Wiley & Sons Ltd. Chapter 11.

Weller HG, Tabor G, Jasak H and Fureby C, (1998). A tensorial approach to computaional continuum mechanics using object-oriented techniques. Computers in Physics 12(6):620-631.

Williams JG, (1984). Fracture mechanics of polymers. Ellis Horwood Limited.

William JG and Hadavinia H, (2002). Analytical solutions for cohesive models. J. Mech. Phys. Solids 50(4):809-825.

Xu CC, Siegmund T and Ramani K, (2003a). Rate-dependent crack growth in adhesives I. Modeling approach. Intl. J. Adhesion Adhesives 23:9-13.

Xu CC, Siegmund T and Ramani K, (2003b). Rate-dependent crack growth in adhesives II. Experiments and analysis. Intl. J. Adhesion Adhesives 23:15-22.

Yang QD and Thouless MD, (2001). Mixed-mode fracture analyses of plastically deforming adhesive joints. Intl. J. Fract. 110:175-187.

Errata

Errata

Errata